NUMERICAL SIMULATION FOR THE MANAGEMENT OF STEADY AND UNSTEADY FLOWS IN THE PRESENCE OF MIXING FOR BIOMEDICAL APPLICATIONS

A THESIS SUBMITTED TO THE FACULTY OF
UNIVERSITY OF MINNESOTA
BY

SRIKAR CHELIKANI

IN PARTIAL FULFILLMENT OF THE REQUIREMENTS
FOR THE DEGREE OF
DOCTOR OF PHILOSOPHY

ADVISER: Dr. EPHRAIM M SPARROW

JANUARY 2014

Acknowledgements

First and foremost, I would like to acknowledge the contribution of my adviser, Dr E.M. Sparrow for his immense motivation, support, advice, and guidance in pursuit of my PhD degree. He has been a great teacher, adviser, and role model. Without his support, this work would not have been possible. I would like to thank the staff and faculty of the University of Minnesota who have provided the technical knowledge and resources for me to undertake this effort. I express my gratitude towards my committee members: Dr. Arthur Erdman, Dr. Rusen Yang, and Dr. Shuzhong Zhang for their valuable time and feedback. I would also be indebted to my many lab mates and colleagues with whom I have enjoyed working with and learnt a great deal from. Of particular mention are my work and personal interactions with Prof. John Abraham, Ryan Lovik, Dan Bettenhaussen, and John Gorman.

I dedicate this thesis to my parents for their unflinching emotional and financial support in all my endeavors. I would like to specially thank my wife for her continuous belief and support through sometimes stressful times. Finally, I would like to thank all my friends, many of whom are like family members (especially Erie Street Rockers Group), for ensuring that my student life at the University of Minnesota was a fun and memorable experience.

Abstract

Numerical simulation models can be a highly effective starting point for the optimal design of biomedical devices. This concept forms the underpinnings of the research to be reported in this thesis. Three unique medical device applications are considered, and numerical modeling and simulation is performed to enable a near approach to an optimal design. Furthermore, numerical models can also provide valuable guidelines for experimentation and product development.

Each of the considered applications serves a therapeutic function. The common denominator to all of the applications is the major role played by fluid dynamics. For each of these applications, a model that conforms closely to the physical situation is formulated and subsequently implemented by numerical computation to yield outcomes of practical utility.

The first of the applications was motivated by the reality that certain patients require frequent access to the vascular system. For example, drug infusion during chemotherapy and dialysis treatment requires such access. To facilitate these intrusions, infusion ports are implanted at suitable sites. The design of such ports must enable convenience in injecting and extracting fluid media. Furthermore, if blood is one of the media, the geometry of the port must be tailored to avoid hemolysis.

Filtration is a major issue in the sanitary handling of biological fluids. The manufacture of such filtration media and other biomedical sterile fabrics makes use of very fine diameter fibers. The second major focus of this thesis is to provide a highly effective means for the production of the needed fibers. The manufacturing process which was majorly improved by the present innovations is the melt-blowing process.

There are many situations in which biomedical fluids must be extracted from the human body. For example, spent tracer fluids used in angiographies become a possible source of kidney damage unless they are extracted. The final focus of the thesis research was to develop a highly effective numerical model whose application guides the design of suction catheters suitable to the existing biological conditions.

Table of Contents

List of Tables

List of Figures

Chapter 1

INTRODUCTION

1.1 Introduction

The advent of high speed micro-processors along with the reduction in costs of computers and memory has led to an explosion in the use of Computational Fluid Dynamics (CFD) in a wide variety of industries. CFD is being extensively used in the design of automobiles, aircraft, HVAC systems, weather forecasting, and biomedical devices. But even today's most powerful super computers are not able to deal with the entire physical system of interest and solve it in its entirety in a reasonable timeframe. Hence, there continues to be a need to convert the physical system of interest into a computational model which can be solved to obtain the required information to guide design, development, and diagnostic efforts. The primary focus of this research is to identify, explore, and develop appropriate computational models of air flow and arterial blood flow for the design and development biomedical devices.

1) A computational model consists of the following components:
2) *A solution domain* which represents the space within which the fluid flow is to be investigated
3) *Boundary conditions* which define how the solution domain interacts with its environment

4) *Governing equations* which describe the physical phenomena occurring within the domain
5) *Material properties* of the flowing media

Once the foregoing ingredients have been assembled, the solution domain is discretized into nodes and elements. The nodes are the selected points at which the solution is be obtained. The governing partial differential equations are descretized and thereby metamorphize into a set of non-linear, highly coupled algebraic equations. The discretization may be performed utilizing either finite difference, finite volume, or finite element methodology [1-9]. A plethora of solution methods are available depending on the adopted software package.

The accuracy of the results of a numerical simulation is strongly dependant on the ability of the model to represent the actual physical system and the accuracy of the numerical algorithm. Faster computers and parallel processing methods have facilitated the use and development of more and more complex models to increase the fidelity of solutions. Complex models are generally more difficult to resolve due to inherent non-linearities and requirements of greater computational time and resources. Simplifications and assumptions can often be employed to get meaningful and useful results in a timely manner but can lead to inaccurate results and conclusions if they are not used appropriately. There exists a tradeoff between accuracy and computational time/resources.

A goal of this thesis is to build and validate numerical models which accurately represent physical situations encountered in the design and development of medical devices and to utilize the model results to enhance the efficacy of related therapies. Effort is also made to quantify the effects of different simplifying assumptions made in the models.

1.2 Challenges in modeling arterial blood flow

The underlying transport mechanism of blood in arteries is very similar to that of pressure- driven flow in a network of tubes. However, there are additional complexities which need to be accounted for while modeling arterial flows. The prominent factors which need to be considered for accurate modeling blood flow in arteries are:

- Blood vessel size and geometry
- Non-Newtonian rheology of blood
- Pulsatile nature of arterial blood flow
- Flow regime: laminar, turbulent or transitional
- Elastic response of the artery wall
- Mass transfer between blood and other media

1.2.1 Blood vessel size and geometry

It is not feasible to model the entire blood circulatory system, so it is common practice to model a section an artery of interest. The diameter and cross section of a blood vessel has a major influence on the characteristics of flow through it. The diameters vary widely

among individuals and also between different vessels of the same individual. A summary of the vessel sizes of the vascular system is shown in Table 1.1 [10].

Besides having different diameters, the vessels may also have a varying irregular cross-section and may contain branches. Most simulations treat the vessel walls to be of a constant circular cross-section. However, accurate vessel geometries may be obtained by combining a series of MRI, Ultrasound, or CT images of the desired section into a format which can be imported into standard CAD software for performing computational analysis. The advantages, limitations, and accuracy of various medical imaging techniques for constructing 3D geometries of blood vessels is analyzed and well-reviewed in the literature [11-13]. While a symmetric circular approximation of arteries often yields quick and useful insights into the flow patterns, it can lead to erroneous results when used in a region where bifurcations and rapidly changing cross sections are present.

Table 1.1 [10]: Diameters and wall thicknesses of various types of arteries

Vessel	Internal Diameter	Wall Thickness	Thickness/diameter ratio
Aorta	1-3 cm	2-3 mm	0.125
Main branches	0.5-2.25 cm	2 mm	0.182
Large arteries	4 -5 mm	1 mm	0.222
Medium arteries	2.5-4 mm	0.75 mm	0.231
Small arteries	1-2.5 mm	0.5 mm	0.286
Tributaries	0.5-1 mm	0.25 mm	0.333
Small rami	250-500 µm	125 µm	0.333
Terminal arteries	100-250 µm	60 µm	0.342
Arterioles	25-100 µm	20-30 µm	0.400
Metaarterioles	10-25 µm	5-15 µm	0.571

1.2.2 Non-Newtonian rheology of blood

Blood is a complex fluid which consists primarily of particulate cells suspended in continuous liquid called plasma. Plasma constitutes about 55% of the blood and mostly contains water (92% by volume) and a small amount of proteins (7%) and inorganic solutes (2%). Studies have shown that plasma can be treated as a Newtonian fluid whose viscosity has a moderate dependence on temperature [14,15]. The particulate phase of blood contains mainly erythrocytes (red blood corpuscles which constitute 99% of

cellular volume fraction), leukocytes (white blood corpuscles) and platelets. The RBC volume fraction in blood is called hematocrit and has a major effect on blood rheology because of their tendency to aggregate or deform. The actual viscosity of blood depends on variety of physiological parameters like hematocrit, rate of shear, plasma viscosity, temperature, gender, smoking habits, physical fitness index, etc. Numerous models have been developed for the viscosity of blood. Yilmaz and Gundogdu [16] have presented a detailed review of those models. The models can be broadly classified into the following categories:

- Newtonian models
- Non-Newtonian models
    - Time-independent Non-Newtonian models
    - Time-dependant Non-Newtonian models

Newtonian and time-independent non-Newtonian models are most commonly used in CFD simulations. Studies have shown that above a certain shear rate value, blood exhibits Newtonian behavior. The threshold shear rate value and Newtonian viscosity depend on various physiological parameters and a wide number of values are available for those factors [17-19]. At low stress levels, the aggregating nature of the erythrocytes causes the blood to behave like a shear-thinning fluid. A number of non-Newtonian models which account for the shear-thinning nature of blood have been formulated based on experimental data. Figure 1.1 displays some of the most-used models [20,21].

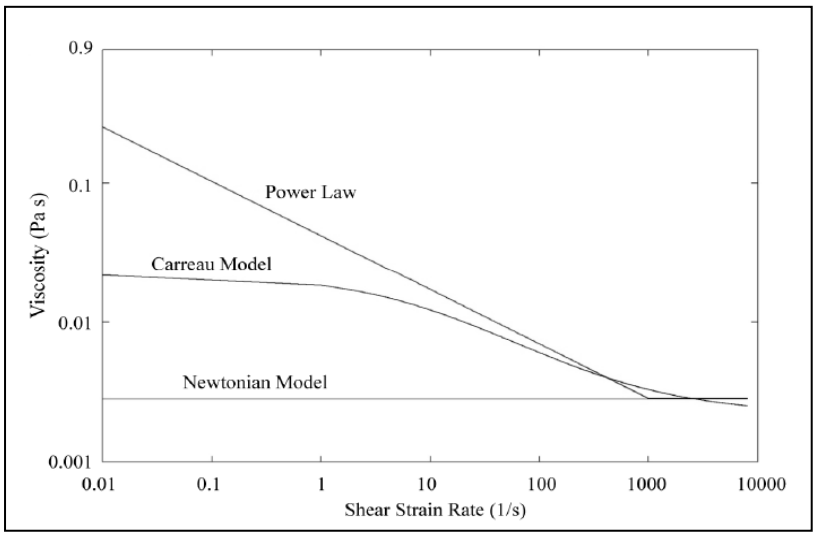

Fig. 1.1: Comparison of commonly used viscosity models for CFD analysis [20,21]

The figure shows the viscosity of blood given by a Newtonian model and two commonly used (power law [20] and Carreau-Yesuda [21]) time-independent non-Newtonian models on a log-log plot. At certain shear rates, blood has also been known to exhibit viscoelastic behavior. Many time-dependent viscosity models have been developed to predict the viscoeslatic or viscoplastic nature of blood [22-24]. Hence, it is very important to identify the maximum and minimum shear rates in the domain to pick a suitable blood viscosity model. The dimensionless parameters to be considered for characterizing blood rheology are the Deborah number (De) and Weissenberg number (We), which are defined as

$$De = \theta_r / T_c \tag{1.1}$$

$$We = \dot{\gamma}_c \theta_r \tag{1.2}$$

where θ_r is the relaxation time (typically 0.06 s for RBCs), T_c is a characteristic time (like time period of pulsation), and $\dot{\gamma}_c$is a characteristic shear rate.

If $De << 1$, the material can be considered viscous; if $De \sim 1$, the material is viscoelastic; and if $De >> 1$, the material is elastic [25]. The elastic properties of the material play an important role when We becomes greater than 1 [21].

It is imperative to identify an appropriate viscosity model for blood based on the encountered flow conditions and shear rates. It is also important to note that the viscosity models are developed from experiments performed in laboratory settings which may not mimic the exact physiology of the human body like the pulsatile nature of the blood flow. Hence, critical results obtained from simulations also need to be validated by experimental data.

1.2.3 Pulsatile nature of arterial blood flow

Many arterial flows are modeled as steady flows [19]. In reality, the blood flow at the inlet of the artery is pulsatile in nature based on the cardiac rhythm [26]. The pulsation has a significant effect on various hemodynamic quantities such as wall shear stress and pressure distribution in the artery. This effect diminishes at greater distances from the heart as the pulses become more damped. The time-dependant flowrates in various arterial segments can be obtained by various methods such as MRI imaging [26] and thermodilution [27]. Figure 1.2 [27] shows the flow rate in the coronary sinus during a cardiac cycle obtained from contrast enhanced MRI imaging. It can be clearly seen that the flow is reversed for a small portion of the cardiac cycle.

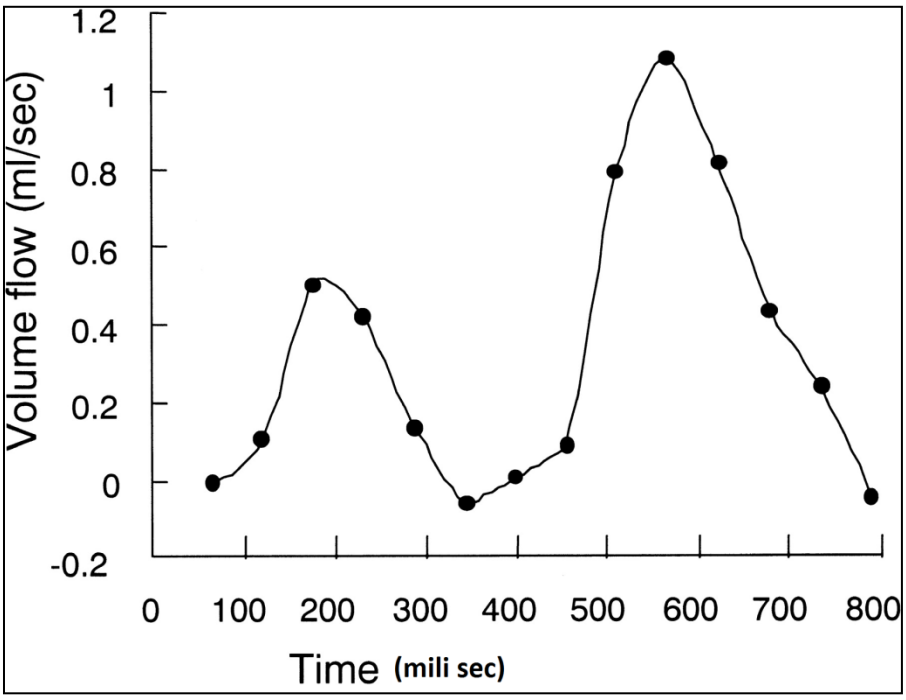

Fig. 1.2 [27]: Coronary sinus flow rate over the cardiac cycle

Though the results of flow measurements are fairly accurate, barely any data is available regarding the radial variation of the flow. This would require the inlet of the solution domain to be extended further upstream to allow the flow to develop. The current state of the art on pulsatile flow models is summarized by Gundogdu et al. [28,29]. Most of these models deal with pulsatile and oscillating flows without any flow reversal. The presence of the pulsation could cause a transition between the laminar and turbulent flow regimes, the modeling of which will be discussed in the next section. The development of computer-controlled pumps which mimic the pumping of the heart has contributed a great deal to the experimental investigation of pulsatile arterial flows and their modeling [30].

1.2.4 Flow regime: laminar, turbulent or transitional

The mean flow rates in most of the arteries would suggest that the blood flow would be laminar in nature. The physics of laminar flow is very well understood. The governing equations for laminar flow are the Navier-Stokes equations along with the continuity equation. The presence of pulsation and other physiological factors like artery shape and plaque formation may lead to the breakdown of laminar flow giving rise to either transitional or turbulent flow.

The most accurate method of resolving such flows are through Direct Numerical Simulation [31] (DNS) which involves a direct solution of the Navier-Stokes and continuity equations with simplifying modeling. The DNS approach requires the whole range (largest to smallest) of spatial and temporal scales of turbulence to be resolved. The smallest dissipative scale associated with most of the kinetic energy dissipation is the Kolmogorov scale, η, given by:

$$\eta = (\nu^3/\varepsilon)^{1/4} \tag{1.3}$$

where ν is the kinematic viscosity, and ε is the rate of kinetic energy dissipation. The simulation is inherently transient and the total time is proportional to the turbulent time scale τ, given by:

$$\tau = L/u' \tag{1.4}$$

where L is the integral spatial scale, and u' is the root mean square of the turbulent velocity component. To obtain a stable solution, the Courant number (C) must be less than unity.

$$C = (u'\Delta t/h) < 1 \quad (1.5)$$

where Δt and h are the time step and mesh size, respectively. The satisfaction of the above conditions requires that the number of nodes and time steps to increase as a power of the turbulent Reynolds number. Thus, this method becomes extremely computational intensive and is not yet suitable for industrial applications due to limitations of memory and time.

Since the use of DNS is impractical for most applications, it has been modified to include a filter which separates the fluid solution domain into a resolved field and modeled field. Such a method is known as Large Eddy Simulation (LES). Usually, the grid is used as the filter where the flow field is resolved ("large eddies") by DNS, and the effect of smaller scales on the resolved velocity field is added by suitable sub-grid scale (SGS) modeling methods. Some results for modeling pulsatile flow related to arterial blood flow have been obtained by LES [32-34] which show the breakdown of laminar flow. Even though this method needs a much smaller grid than DNS, it is still too computationally intensive for widespread use.

The most commonly used methods for turbulence modeling are based on the Reynolds-Averaged Navier-Stokes (RANS) equations. These equations are the time-averaged equations of the flow field which are obtained by applying the Reynolds decomposition of splitting the flow variable into an average and fluctuating components and introducing

this decomposition into the Navier-Stokes and continuity equations. The RANS equation for incompressible flow and Newtonian viscosity in the X-direction is:

$$\rho\left[\frac{\partial u}{\partial x}+\frac{\partial}{\partial x}(\bar{u}^2)+\frac{\partial}{\partial y}(\bar{u}\bar{v})+\frac{\partial}{\partial z}(\bar{u}\bar{w})\right]=-\frac{\partial p}{\partial x}+\mu\left[\frac{\partial^2\bar{u}}{\partial x^2}+\frac{\partial^2\bar{u}}{\partial y^2}+\frac{\partial^2\bar{u}}{\partial z^2}\right]-\left[\frac{\partial}{\partial x}\left(\rho\overline{u'^2}\right)+\frac{\partial}{\partial y}\left(\rho\overline{u'v'}\right)+\frac{\partial}{\partial z}\left(\rho\overline{u'w'}\right)\right] \quad (1.6)$$

The last three terms of the foregoing equation represent the turbulence inertia. They are designated as “Reynolds stresses”. Turbulence models provide closure by introducing additional equations to solve for these “stresses”. Generally, turbulent models are developed for Newtonian cases, and the effects of non-Newtonian nature on turbulence are documented in literature [35-37]. The most widely used models can be classified into:

Two-Equation Models

Reynolds Stress Models

The two-equation models introduce two additional equations to solve for the turbulence kinetic energy and its dissipation [38]. The simplest such model is the k-Epsilon Model which works very well for the free-shear regions. The k-Omega Model is very accurate for flow near the walls. The Shear Stress Transport (SST) model combines the best features of the k-Epsilon and k-Omega models. It assumes the characteristics of the K-Epsilon in the far-from-wall region and behaves like k-Omega near the walls. All these models are based on assuming an isotropic nature of turbulence.

The Reynolds Stress Models (RSM) [38] directly computes the individual Reynolds stresses and takes into account their directional effects. This model introduces additional equations (up to seven) to solve for the Reynolds stresses, and hence is much more computationally intensive and less robust than the others. In principle, the RSM method should be the most accurate RANS-based model but, different turbulence models work better for specific flow types. Hence, these models must be validated for the specific flow conditions before being applied. There are numerous books [39-41] available on turbulence modeling for CFD.

A major drawback of the traditional RANS-based models is their inability to account for transitional flows (between laminar to turbulent and vice versa). Menter et al. [42-44] have modified the SST model to account for transition in external flows. Abraham et al. [45] have tuned the constants of the SST model for simulating transition in internal flows. These authors [46,47] have used the model to predict "laminarization" and "turbulentization" of pulsatile flow. The pulses used, however, were sinusoidal in nature and did not contain a reversed flow component. It is extremely important to identify and validate an appropriate turbulence model for simulating the arterial blood flow.

1.2.5 Elastic response of arterial walls

The fluid flow through the artery has a major impact on the shape of the artery wall and vice- versa. Hence, it is essential to account for the deformation of the artery walls in order to accurately solve for the fluid flow. This involves a coupling between the fluid-

mechanical and structural-mechanical problems. The fluid exerts a load (pressure and wall shear) on the wall causing it to deform which, in turn, leads to a variation in the fluid flow, hence changing the load. Such a class of problems is generally known as two-way, fluid-structure interaction (FSI). The steps involved in solving a FSI problem are illustrated in Figure 1.3.

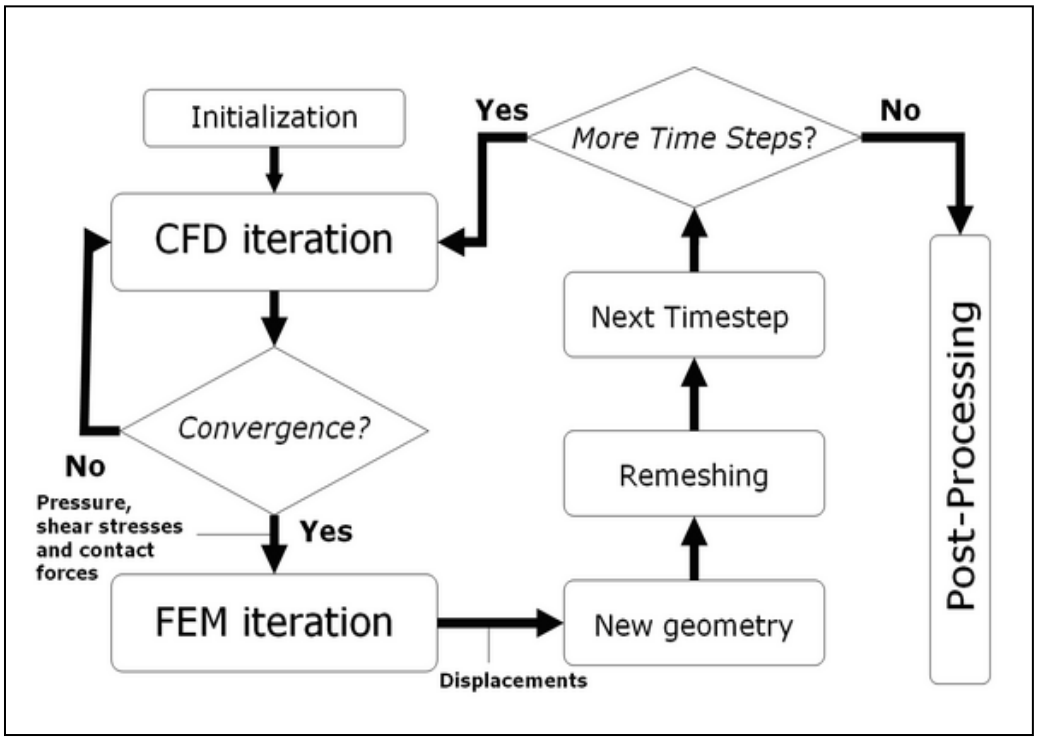

Fig. 1.3: Steps in solving a FSI problem [48]

The fluid flow problem is solved first using CFD. The governing equations for the fluid flow are the Navier-Stokes (RANS) and continuity equations. The wall is held fixed for the initial fluid flow iteration. After the flow is solved, the results such as wall shear and pressure are extracted and exported as loads to the FEM (finite-element method) solver to

determine the displacement. The governing equation for the structural problem is the conservation of linear momentum for a solid body given by:

$$\rho_w \frac{\partial^2 d_i}{\partial t^2} = \frac{\partial \sigma_{ij}}{\partial x_j} + F_i\,, \quad i = 1,2,3 \tag{1.7}$$

where $\rho_w$is the wall density, d_i and $\sigma_{ij}$are displacement and stress component respectively, and F_i is the force component on the body. In addition to the foregoing equation, a relationship between the stress and strain for the material is also required. For a linear material, that relationship is given by:

$$\vec{\sigma} = D\vec{\varepsilon} \tag{1.8}$$

in which $D$is the matrix of elastic constants (Youngs Modulus and Poissons ratio). Sigma and epsilon are the stress and strain tensors respectively. The deformation results are then exported to create a new geometry/mesh for the next iteration of the fluid flow solution. An Arbitrary Lagrangean Eulerian(ALE) based method is used to obtain convergence between the two solutions [48].

Key inputs for solving the FSI problem are the artery wall thickness and material properties. The general range of arterial wall thicknesses was shown in Table 1.1. Numerous models are available in the literature for modeling the elastic behavior of the artery walls. Kalita et al. [49] present a detailed review of such models. In general, the artery wall can be considered to be made of three layers or *tunicae* which are shown in Figure 1.4.

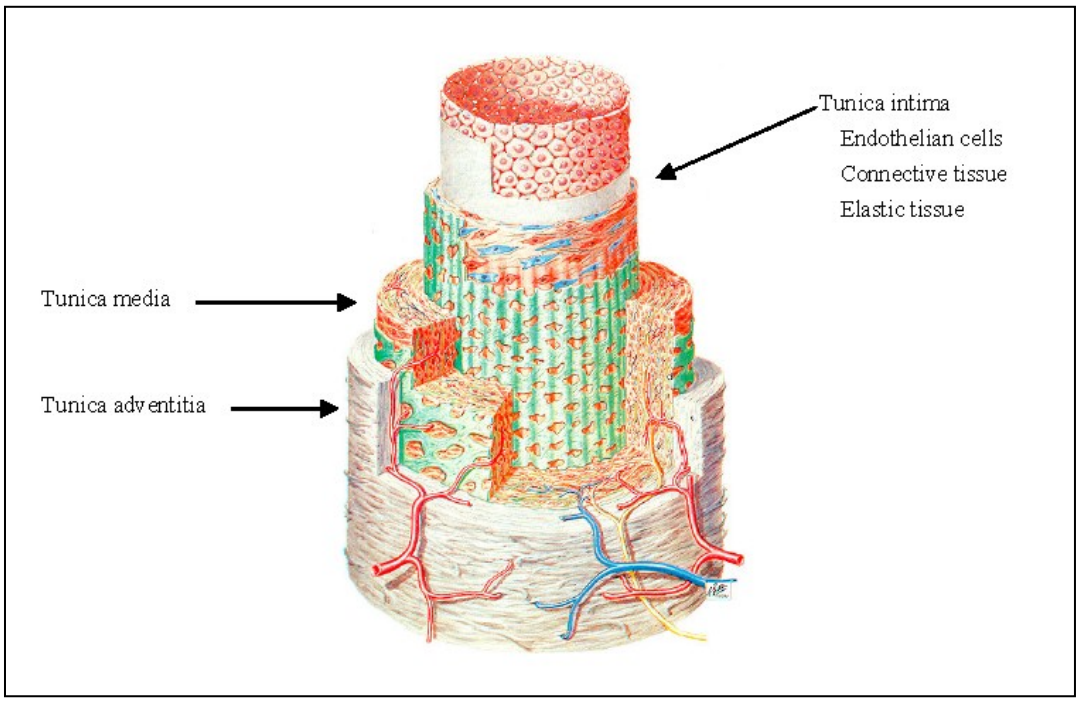

Fig. 1.4: The three layers of the artery wall

The innermost layer, called the *tunica intima,* consists of a monolayer of endothelial cells resting on a thin membrane and has a negligible effect on the mechanical properties of the artery wall [50]. The middle layer called *media* is the thickest layer and makes the largest contribution to the elastic nature of the arteries [51,52]. The outermost layer called *adventitia* consists mainly of loose collagen fibers embedded in a ground substance to protect the artery from its surroundings. The elastic modulus of this layer is shown to be at least an order of magnitude lower than the media [51].

Numerous models exist for predicting the elastic properties of the artery walls. Some of these models even take into account the presence of multiple layers and the physiological composition of the artery tissue. There are also studies which obtain these properties by

direct experimentation on tissue and by indirect methods using computer-imaging technologies [52-54]. The elastic properties of the wall are generally anisotropic and could also be non-linear.

Since the primary focus of the proposed simulation is the fluid-flow pattern, mass transfer, and wall shear stress, and not the variation of the stresses in the wall itself, the artery wall can be modeled as a single layer with linear material properties. The only required result from the structural analysis is the deformation, and this quantity can be validated by obtaining the shape of the artery as a function of time over the cardiac cycle using imaging techniques. Alternatively, the need for structural simulation can be eliminated by using the data from these images to create the required mesh motion. There are also polymer materials available which mimic the behavior of human arteries [55]. If necessary, the simulation can be expanded at the expense of computational time, stability, and resources to account for the presence of multiple layers and non-linear properties of the artery walls.

There are a number of papers in literature on FSI for modeling arterial blood flow [56-59]. These models are of varying complexities and some of them even model the transition to turbulent flow. However, none of these models investigate or model the possible re-laminariztion of the flow.

1.3 Development and application of computational models

While it is possible to build and validate an all-encompassing model which accounts for all the aforementioned complexities, it would not be practically viable to use such a model every time computational results are desired. Depending on the application and outputs of interest, further simplifications can be made and validated using known results or experimentation. A simple validated model can be an extremely efficient and powerful tool which can be used to substitute or supplement experimental work. It can lead to expedited and enhanced design of devices and processes while reducing costs of benchtop, animal-model, and in-vivo/in-vitro testing.

Attention is focused, in the subsequent chapters, to the development of such models for the following applications:

- Flow analysis of implantable infusion ports
- Investigation of the Coanda effect to optimize the production of bio-medical filtration materials
- Analysis of suction catheters for applications such as the extraction of spent contrast media

1.3.1 Flow Analysis of implantable infusion ports

An implantable infusion port is a medical device which is placed subcutaneously to grant easy and permanent access to a patient's vascular system. Such ports are used to

withdraw and/or deliver blood from patients who require frequent hemodialysis. Besides hemodialysis, infusion ports are also commonly used to deliver parenteral nutrition, fluorescent contrast media for angiography, chemotherapy drugs for cancer patients, analgesics and antibiotics to the blood stream, and to withdraw blood samples. The use of an infusion port reduces the trauma faced by patients who might otherwise require multiple needle pokes to grant intravenous access and also significantly lowers the risk of leakage of potent chemotherapy drugs into surrounding tissues. A typical infusion port is depicted in Figure 1.5.

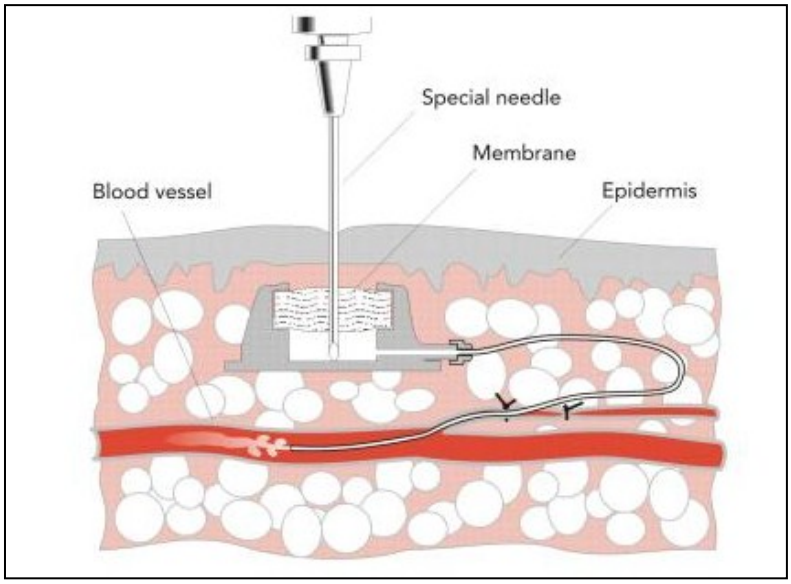

Fig. 1.5: Implantable infusion port

An infusion port consists of a fluid reservoir which is covered on top with a membrane. The membrane is typically made of silicone which can be pierced by a special needle to grant access to the reservoir. The needle can be connected to a manual or power syringe

to deliver or withdraw blood or other fluids to/from the reservoir. The outlet of the reservoir is connected to a catheter which is grafted into an artery/vein of interest. Besides the stated benefits of infusion ports, there are also some risks factors like hemolysis and thrombosis associated with their use. Thrombosis is the formation of blood clots and can lead to the port becoming inoperable. Hemolysis is the damage caused to blood cells due to excessive shear stress. The goal of Chapter 2 is to develop appropriate models to simulate the fluid flow in infusion ports and to extract flow metrics which can be used to evaluate and optimize the design and operation of these ports.

Reservoir geometry and fluid flow rates are the main parameters which determine the flow patterns and shear stress levels in the port. Reducing the shear stress levels experienced by blood passing through the port would lead to lowering the risk of hemolysis. Although lower shear stress levels reduce the risk of hemolysis, regions of extremely low shear stress could lead to stagnation zones which increase the propensity of forming blood clots which causes thrombosis. Reducing or eliminating the number of stagnation zones would significantly lower the risk of thrombosis. There is also need for the reservoir to serve as an efficient mixing chamber when the port is being flushed with saline to remove a stagnant pool of blood which may otherwise lead to infections or clotting. Good mixing is also desired when contrast media, medication, or nutrition is being delivered into the port. The port must also be capable of operating in the reverse-flow mode when blood needs to be withdrawn from the port. Numerical analysis can serve as a very powerful tool in optimizing and analyzing the design of infusion ports.

Chapter 2 is dedicated to the analysis of fluid flow and mass transfer processes occurring in such ports.

1.3.2 Investigation of Coanda-effect to optimize production of biomedical filtration materials

While Chapter 2 deals with the analysis of liquid (primarily blood) flow, the focus of Chapter 3 is the simulation of air flow to optimize the melt-blowing process for the manufacture of fine fibers used in biomedical filtration materials. For patients undergoing dialysis, a pump along with a catheter and infusion port is used to remove impure blood from the body. The impure blood is filtered outside the body and pumped back into the patient. The filtration medium consists of polymeric materials which are made of very thin nano-fibers. Such fine-fibers are typically made using the melt-blowing process. Figure 1.6 shows a schematic representation of the melt-blowing process.

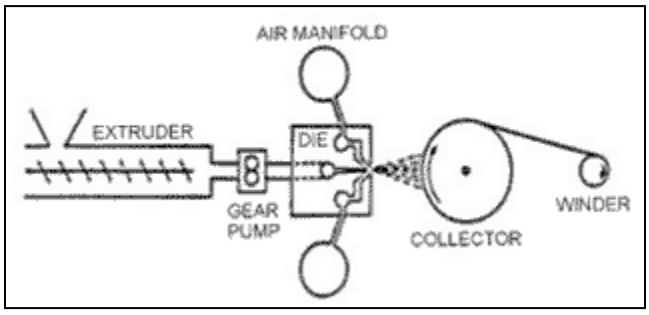

Fig. 1.6: Schematic diagram of the melt-blowing process

In the melt blowing process, hot molten polymer is pumped into an extrusion die where it is stretched by friction caused by high-velocity, hot air jets. The air jets elongate the

molten polymer along the flow direction, and the polymer melt solidifies into fine fiber strands as it cools in the downstream direction. These fiber strands are collected onto a spinning web. This method is one of the most common ways of producing non-woven fabrics and is widely studied in the literature [60-64]. Fabrics made by this process have a wide range of applications, some of which are listed below:

- Manufacture of filters for blood, air, water, gasoline, oil, tea, etc.
- Biomedical fabrics like face masks, gowns, and other sterile equipment
- Thermal insulation materials
- Membranes for pharmaceutical processing, allergens, drainage systems, etc.

Different applications require fibers of different diameters. The melt-blown process can produce fibers with diameters as large as 15 microns and as small as 0.1um. The physical attributes of the fabrics such as fiber diameter and uniformity are strongly influenced by the air flow characteristics, collector speed, and spacing between the die and collector. The goal of Chapter 3 is to investigate a novel approach of invoking the Coanda effect to control the trajectory of flowing air to obtain a uniform thickness of fibers on the collector. *The Coanda effect is the tendency of a fluid jet to be attracted to a nearby surface*. The Coanda effect has a wide range of applications, the most common of which is to generate lift for aircraft. It is generally associated with curved surfaces, and the literature is quite sparse on the use of plane-wall Coanda effects. Chapter 3 investigates the use of both curved and plane walls for invoking the Coanda effect to control the trajectory of air jets used in the melt-blowing process. It also explores the use of other

features of the Coanda-producing wall such as the lateral distance of the wall from the fluid jet, downstream length of the wall, and curvature of the wall to control the trajectory of the fluid jet.

The methodology used in Chapter 3 can also be applied to study other biomedical and physiological phenomena where the Coanda effect is present such as in fluidic ventilators, air distribution in lungs, fetal blood circulation, and human phonation [65-67].

1.3.3 Analysis of flows in suction catheters for extracting spent contrast media to prevent contrast-medium-induced nephropathy (CIN):

Chapter 1 dealt with the analysis of blood flow in an implantable infusion port which is connected to a catheter which can be used to deliver or remove fluids to/from the body. The aim of Chapter 4 is to study the flow characteristics of a suction catheter which is used to remove blood from the body. The intended application of the catheter is to prevent contrast–medium induced nehproapthy (CIN) which is the damage caused to kidneys when they encounter iodine-based-contrast media used during arteriographies.

1.3.3a Introduction to Contrast-Induced Nephropathy (CIN)

Iodine-based-contrast agents are used for a number of X-ray based medical imaging techniques such as angiography (arterial investigations) and venography (venal investigations). Some of the major applications of such methods are:

- Detecting the presence or absence of atherosclerosis
- Visualizing the arterial and venal blood flow to various organs
- Identify vessel narrowing
- Aiding physicians in performing interventional work such as stenting or treating aneurisms.

Angiography involves injecting a radio-opaque contrast media into the blood vessels and imaging using X-ray-based methods such as fluoroscopy. Access to the blood vessels is gained either through the femoral artery for imaging arterial system and the left side of the heart, or the femoral vein for visualizing the venous system and the right side of the heart. Catheters steered by guide wires are used to inject an iodine-compound-based contrast media into the blood stream at the area of interest. The contrast agent absorbs X-rays making it visible on X-ray images. These images can either be still or motion images. The images are then processed and modified into a suitable form by a computer. Figure 1.7 illustrates a typical angiography procedure.

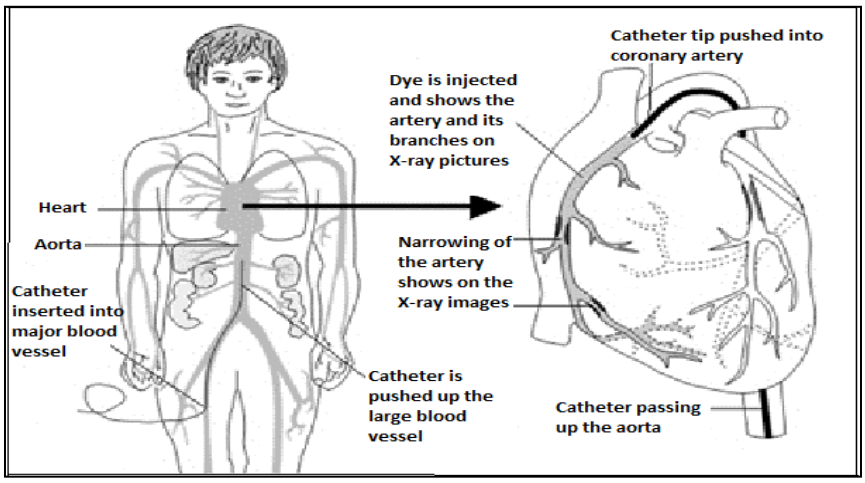

Fig. 1.7: Schematic diagram of coronary angiography

Iodine-based-contrast agents are chosen because of their water solubility and relatively harmless interaction with the human body for normal healthy individuals. These agents are available as clear solutions and can be used without any significant side effects almost anywhere in the body. However, the interaction of contrast media with the kidneys can lead to serious kidney damage and cause acute renal failure for patients suffering from certain pre-existing conditions [68-72]. Damage caused to kidneys by the iodinated-contrast agent is known as contrast-induced nephropathy (CIN) and is defined as a greater than 25% increase in serum creatinine or an absolute increase of 0.5 mg/dL in serum creatinine within 48 hours of using a contrast agent [73]. An increase in blood creatinine level indicates a significant damage to nephrons. Contrast-agent damage is the third most common cause of hospital acquired renal deficiency. Studies have shown that the mortality rate amongst those who developed CIN is much higher than those who did not develop CIN upon administering contrast agent (almost five fold increase in mortality rate) [74,75]. CIN was also shown to be an independent predictor of mortality for patients

undergoing percutaneous coronary intervention (PCI) [76]. Harjai et al. [77] developed a new tripartite classification of CIN for patients undergoing PCI. The probability of developing CIN sharply increases for patients with the following risk factors:

(i) Chronic kidney disease (most important factor)

(ii) Pre-existing renal dysfunction

(iii) Congestive heart failure

(iv) Diabetes

(v) Older age

The use of iodinated-contrast-based angiography is often unavoidable in certain cases despite its inherent risk of causing CIN. There is also no proven efficacious pharmacological or mechanical treatment for eliminating CIN. Dialysis and hemofiltration have also not proven to be viable strategies for treating CIN. Hence, there is a strong need for a device which either eliminates the occurrence or significantly reduces the risk of CIN. The goal of chapter 4 is to create a suitable numerical model for simulating the operation of such a device. The model would provide insights into the effects of operating parameters (such as pressure and time) on the performance of the device and aid in developing a catheter which would minimize any harmful effects on the human body.

1.3.3b Proposed device to eliminate CIN

Although the underlying mechanism of contrast-induced nephropathy is not fully understood, its occurrence can be eliminated by preventing the contrast media from entering the kidneys. The severity of CIN can be reduced by decreasing the amount of contrast media which enters the kidneys.

This can be achieved by draining out the contrast fluid from a location downstream of the angiography region and upstream of the kidneys. A significant share of angiographies involve coronary angiographies for assisting in angioplasty which may require administering contrast agent multiple times. A schematic diagram for a proposed device to remove contrast agent during coronary angiography [78,79] is shown in Figure 1.8.

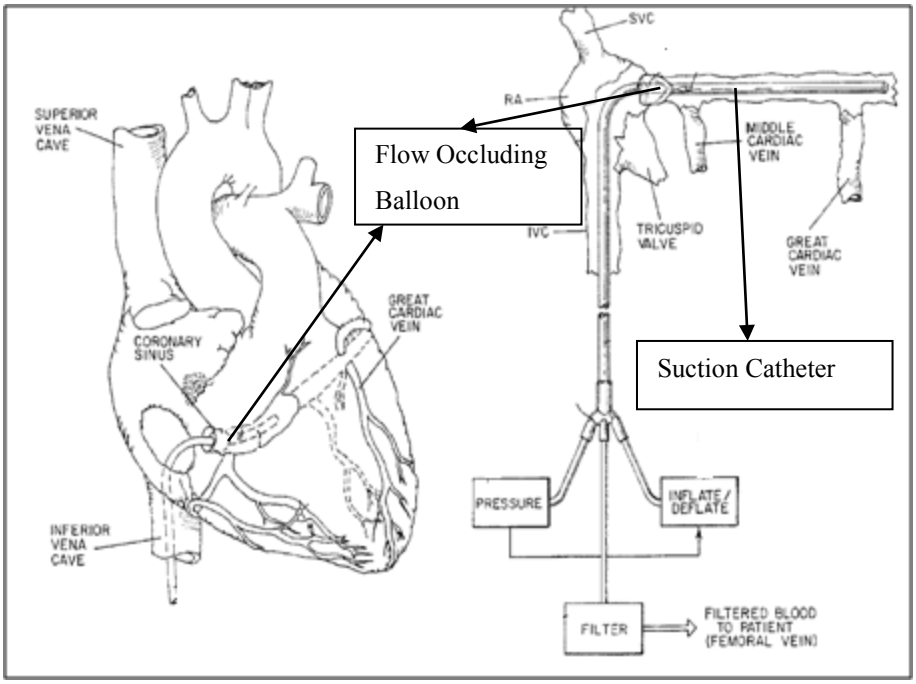

Fig. 1.8 [78]: Schematic diagram of a device to eliminate CIN

The device consists of a catheter placed in the coronary sinus and connected to a suction pump. When contrast is introduced into the blood in the coronary arteries, it is prevented from entering the right atrium of the heart by drawing the contrast laden blood through the suction catheter placed in the coronary sinus. Depending on the volume being withdrawn, the contrast-laden blood can either be discarded or filtered outside the body and returned through the femoral vein. The catheter may also be attached to a low pressure balloon to temporarily occlude the coronary sinus in order to prevent contrast from escaping into the right atrium.

Though the above method is for coronary arteriographies, it can also be applied to other regions of the body. The location of the suction catheter would depend on the zone being analyzed using contrast media. The tip would ideally lie in a large vessel, between the zone being analyzed and the kidneys, which carries the bulk of the contrast flow.

1.3.3c Suction catheter model

The purpose of chapter 4 is to create a suitable numerical model to guide the design of the catheter component of the proposed device in the preceding section. The primary challenge in building such a model would be to account for the effects of various physiological factors of the surrounding artery in which the catheter is placed like the pulsatile nature of blood flow, non-Newtonian rheology of blood, complex arterial size and shape, and elastic behavior of the artery walls. Accurate modeling of the fluid dynamics of the system is necessary to study the influence of the device characteristics

and operating parameters such as geometry, suction pressure and time on the efficacy of the method and also for eliminating potential harmful physiological conditions such as hemolysis [80,81] and artery wall damage [82,83] which are closely related to the fluid flow.

Though aimed at developing a suction catheter to remove contrast media, the concepts developed in chapter 4 can also be applied to other suction catheter applications involving the removal of blood such as hemodialysis, hemofiltration, and removal of blood clots [84,85].

Chapter 2

FLUID FLOW AND MASS TRANSFER ANALYSIS IN VASCULAR ACCESS PORTS

2.1 Introduction

The focus of this chapter is the fluid mechanics and mass transfer of fluids that are passing through a permanent implantable infusion port in the human body. The operation and applications of such ports have been outlined in Chapter 1. The goal of this chapter is to develop a suitable computational model which would be capable of evaluating different port designs and providing guidance for optimizing the port geometry and operating parameters for lowering the risk of harmful physiological effects. The work will be subdivided into three parts. In the first part, the flow of a homogenous fluid through several infusion port geometries will be analyzed. The second part will consider fluid flow and mass transfer, the latter due to the presence of a second miscible species like saline. The third part would be similar to the first part, but include flow at a higher flow rates and also in the reverse direction which is likely to be encountered in dialysis applications.

The numerical simulations will be performed by means of ANSYS – CFX software. This is a commercial code based on a finite-volume discretization of the Navier-Stokes

equations, the conservation of mass equation and, when appropriate, a species conservation equation. The solutions encompass unsteady three-dimensional flows.

2.2 Physical situations

As discussed in the foregoing, three physical situations are to be considered. The first of these is a homogenous flow without mass transfer, the second is an inhomogeneous flow with mass transfer, and the third is a homogenous flow at higher flow rates and flow-direction reversal for dialysis applications.

2.2.1 Unsteady three-dimensional flow of a homogeneous fluid

2.2.1a Port geometry description

Overall views of the three geometries to be considered are conveyed in Figures 2.1, 2.2, and 2.3. These three configurations, respectively designated as A, B and C, correspond to different candidate ports. The first two of these are already used in practice, while the third is a new design whose evaluation is an important goal of this investigation. A common feature of all three configurations is an inlet aperture through which a fluid is introduced into a relatively large reservoir. The inflowing fluid serves to displace fluid that is already in the reservoir, the result of the displacement being an outflow into a catheter which delivers fluid to the blood stream.

Geometrical differences among the three ports are related to the shape and size of the reservoir as well as the location of the reservoir exit. As will be demonstrated when the results are presented, these differences give rise to potential hemolysis-creating flow patterns. Three-dimensional isometric views of the three investigated ports are displayed in Figs. 2.1, 2.2, and 2.3.

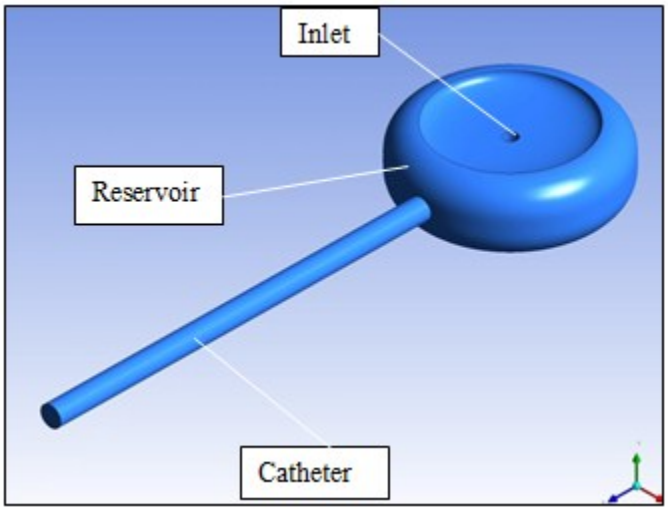

Fig. 2.1: Three-dimensional isometric view of Port A

Figure 2.1 shows Port A. In essence, it is a flat disc with a cylindrical depression in its upper surface. The disc is hollow and serves the purpose of a reservoir. The aperture shown in the figure and labeled inlet is created by the user when inserting the needle of a syringe. The catheter is attached to the reservoir along a radial line extending outward from its periphery.

The second of the currently available ports, to be designated as Port B, is exhibited in Fig. 2.2. Once again, the reservoir is a hollow disc-shaped body. The catheter is joined to the reservoir as a tangent to its outer rim. The last of the ports, shown below, is to be designated as Port C. It differs from Port B in that the attachment of the catheter to the reservoir is accomplished by means of a gently converging transition section.

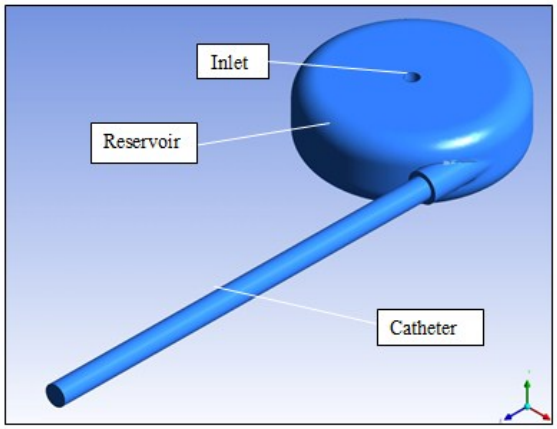

Fig. 2.2: Three-dimensional isometric view of Port B

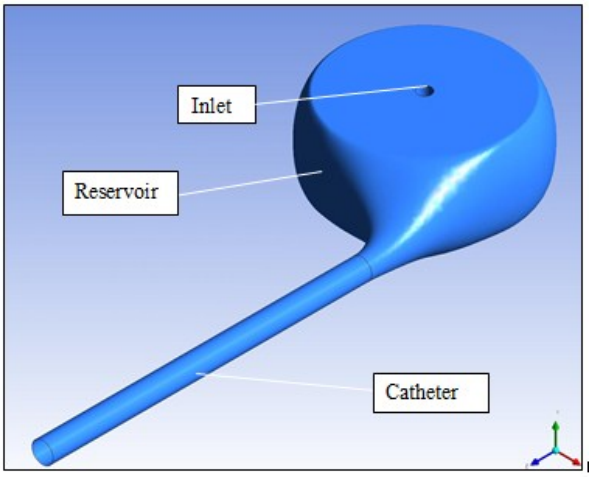

Fig. 2.3: Three-dimensional isometric view of Port C

In Port C, the capability to build a gentle convergence into the catheter is enabled by the height of the reservoir being considerably larger than the diameter of the catheter. It can be expected that the gradual contraction would give rise to a much smoother inflow than would occur for Ports A and B which do not have this feature.

To reinforce the foregoing discussion, Figs. 2.4, 2.5, and 2.6 have been prepared. These figures are planar cuts which show the geometry of the transitions from the reservoir to the catheter. Figure 2.4, which corresponds to Port A, has a transition which includes a sharp-edged inlet. It is well known that sharp-edged inlets give rise to flow separation because fluids are unable to turn sharp corners. The inlet shape shown in Fig. 2.5 (Port B) includes a turn that is greater than 90 degrees. Such a turn is even more difficult for a fluid to negotiate than would be a 90-degree turn. Again, flow separation is to be expected. Another feature of the geometry of the transition section of Port B is the abrupt change of cross section that can be seen at the top of the diagram (Fig. 2.5). Such an abrupt change is difficult for the fluid to cope with, and separation is likely.

The just-identified two geometric errors in the design of Port B have been corrected in Port C as can be seen from Fig. 2.6. Not only has the more than 90-degree turn been eliminated, but also a rounding of the transition geometry has been introduced. Furthermore, the abrupt change of cross section noted at the end of the last paragraph no longer exists in Port C.

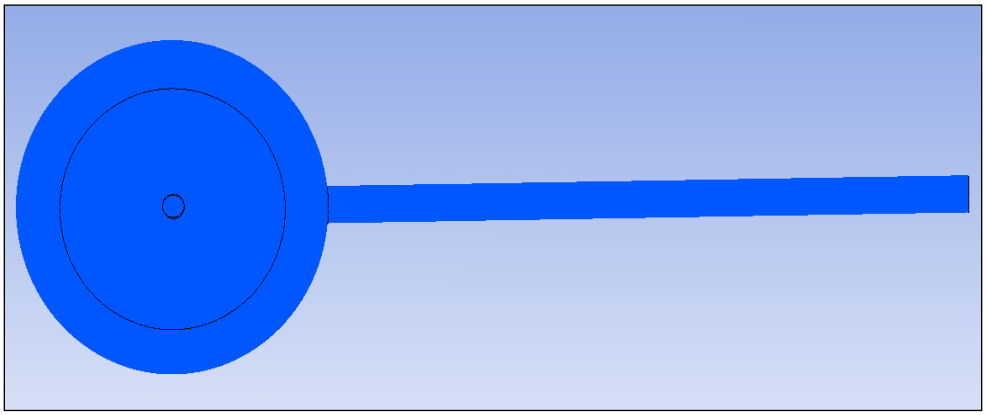

Fig. 2.4: Planar view of Port A

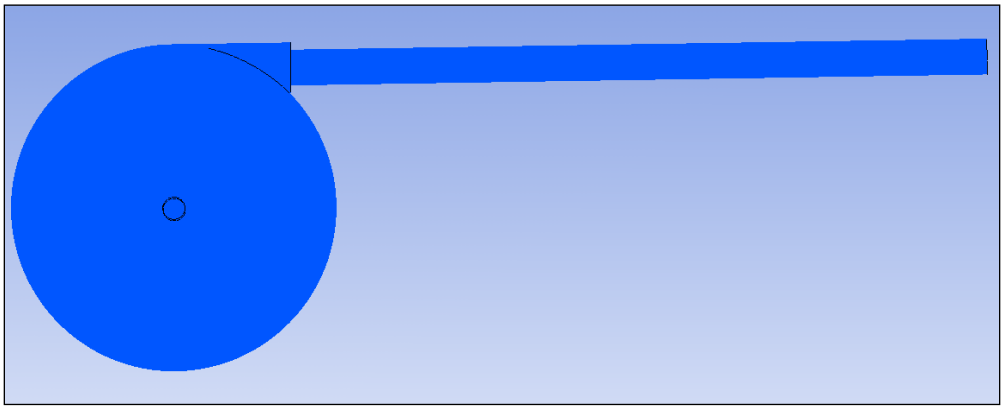

Fig. 2.5: Planar view of Port B

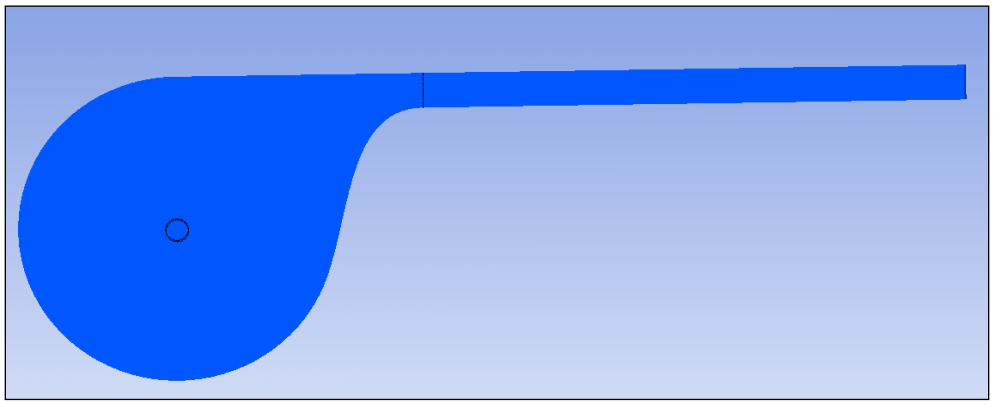

Fig. 2.6: Planar view of Port C

2.2.1b Governing equations for fluid flow

The equations which will be solved for the fluid-flow problem are the three-dimensional, unsteady, incompressible form of the Navier-Stokes equations and the equation of continuity. In these equations, two constitutive equations were employed. The first is the Newtonian model which makes use of a constant value of the viscosity. The other is a non-Newtonian model, two candidate forms of which were used.

Navier-Stokes Equations:

$$\rho\left[\frac{\partial u}{\partial t}+\frac{\partial u^2}{\partial x^2}+\frac{\partial(uv)}{\partial y^2}+\frac{\partial(uw)}{\partial z^2}\right]=-\frac{\partial p}{\partial x}+\frac{\partial}{\partial x}\left(\mu\frac{\partial u}{\partial x}\right)+\frac{\partial}{\partial y}\left(\mu\frac{\partial u}{\partial y}\right)+\frac{\partial}{\partial z}\left(\mu\frac{\partial u}{\partial z}\right) \tag{2.1}$$

This equation applies for the x-coordinate direction. The quantities *u, v,* and *w* are the velocity components in the *x, y,* and *z* directions; ρ is the density, *p* is the pressure, and μ is the viscosity. The symbol *t* represents time. The other two components are obtained by cycling *u, v,* and *w* and *x, y,* and *z*. Note that the viscosity is contained within the differentiation operators to accommodate the spatial variations of the non-Newtonian model. For the Newtonian model, the viscosity passes through these operators.

Continuity Equation:

$$\frac{\partial u}{\partial x}+\frac{\partial v}{\partial y}+\frac{\partial w}{\partial z}=0 \tag{2.2}$$

The boundary conditions for the velocity problem are: (a) all velocities are zero on all solid surfaces, (b) the fluid entering the solution domain is assigned a steady velocity that is uniformly distributed across the inlet section, and (c) standard weak boundary

conditions are imposed at the exit of the catheter, and a pressure is prescribed there. Since the problem is unsteady, an initial condition is also needed. The condition of zero velocity and uniform pressure throughout the solution domain was imposed as the initial condition.

2.2.1c Numerical simulations

For each of the port configurations, the numerical simulation mimicked an experiment which was initiated with both the reservoir and the catheter filled with blood. The activation of the fluid motion was accomplished by the steady injection of a second fluid (sometimes the same as the fluid already in the system and sometimes a different fluid). The operating conditions for the executed numerical simulations are listed in Table 2.1. It can be seen from the table, nine of the investigated cases were characterized by the same injected volumetric flow, 10 ml/min. To implement a sensitivity study, the other three cases were accorded injected flow rates that were four times higher. The period of injection was the same for all cases. The injected fluids were either blood or saline.

Table 2.1: Detailed information for the numerical simulation parameters

Run No.	**Port Type**	**Injected Fluid**	**Rate of Injected Volume (ml/min)**	**Injection Time (s)**	**Total Domain Volume (m^3)**	**Constitutive Law**
1	A	Blood	10	2	7.51e-7	Newtonian
2	B	Blood	10	2	8.85e-7	Newtonian
3	C	Blood	10	2	9.96e-7	Newtonian
4	A	Blood	40	2	7.51e-7	Newtonian
5	B	Blood	40	2	8.85e-7	Newtonian
6	C	Blood	40	2	9.96e-7	Newtonian
7	B	Blood	10	2	8.85e-7	Non–Newtonian 1
8	C	Blood	10	2	9.96e-7	Non–Newtonian 1
9	C	Blood	10	2	9.96e-7	Non–Newtonian 2
10	A	Saline	10	2	7.51e-7	Newtonian
11	B	Saline	10	2	8.85e-7	Newtonian
12	C	Saline	10	2	9.96e-7	Newtonian

The numerical solutions made use of two constitutive models for blood, either Newtonian or non-Newtonian. For the latter, two different algebraic models were employed. These equations are:

Carreau Equation [86] (Non-Newtonian 1):

$$\mu = \mu_{\infty} + \left[(\mu_0 - \mu_{\infty})(1 + (\gamma\lambda)^q)^{\left(\frac{m-1}{q}\right)}\right] \quad (2.3)$$

Power Law (Non-Newtonian 2):

$$\mu = k\gamma^{\frac{n-1}{10}} \text{ for } 0.001 \leq \gamma \leq 1000 \quad (2.4)$$

$\mu = k*1000^{(n-1)/10}$ for $\gamma \geq 1000$

$\mu = k*0.001^{(n-1)/10}$ for $\gamma \leq 0.001$

where μ is the viscosity (kg/m-s), and γ is the shear rate (1/s). The quantities *m, q, λ, n,* μ_{∞}, and μ_0 are constants. Values of the Carreau constants were: λ = 0.11, m = 0.392, μ_0 = 0.022

kg/m s, μ_{∞} = 0.0022 kg/m s, and q = 0.644 [87]. For the power-law model, k = 0.42 and n = 0.61.

A graph of these equations is displayed in Fig. 2.7. In that figure, the viscosity is plotted as function of the strain rate. Also appearing in the figure is a horizontal line that represents a Newtonian model for blood. It can be seen from Fig. 2.7 that at higher shear rates, both the above models become very close to the Newtonian model.

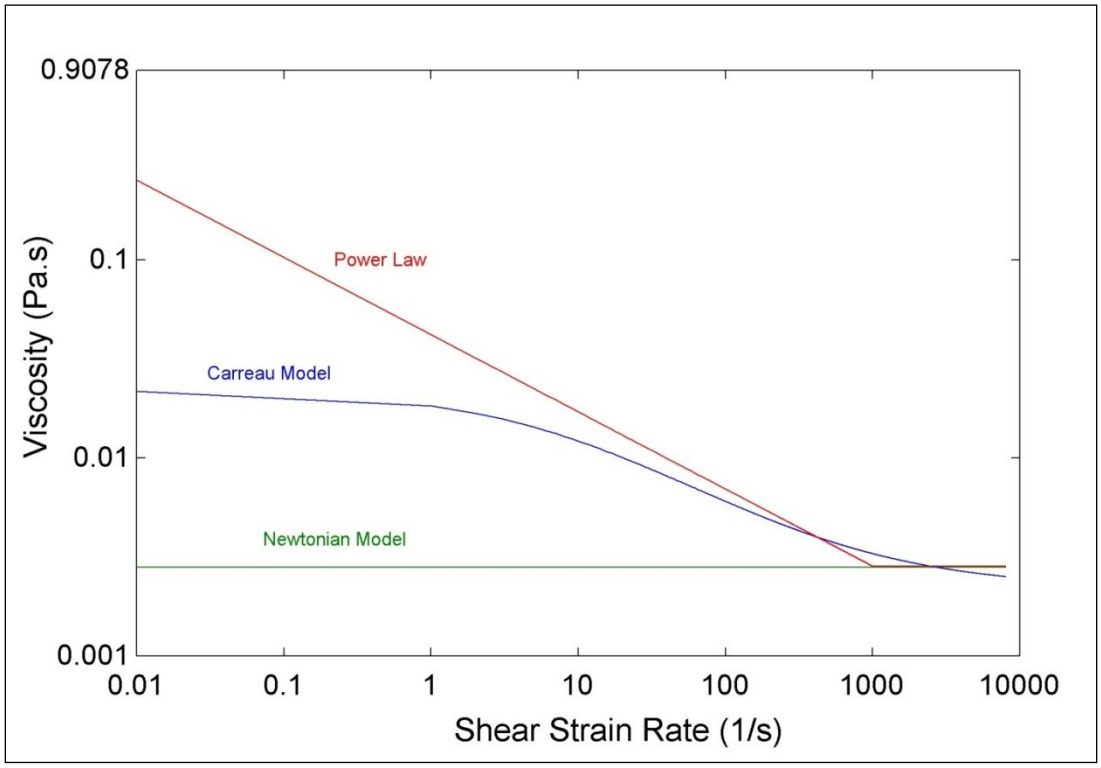

Fig. 2.7: Viscosity of blood according to the Carreau model, the power-law model, and the Newtonian model.

2.2.1d Diagnostic display of fluid flow results

Figures 2.8 and 2.9 respectively show the variation of the shear strain rate and pressure gradient along the center line of the catheter extending from the center of the reservoir to the downstream end of the catheter. The center line of the catheter lies along the z coordinate. The length from $z = 0$ to $z = 0.011$ (m) extends from the center of the reservoir to the outlet of the reservoir which is also the inlet of the catheter.

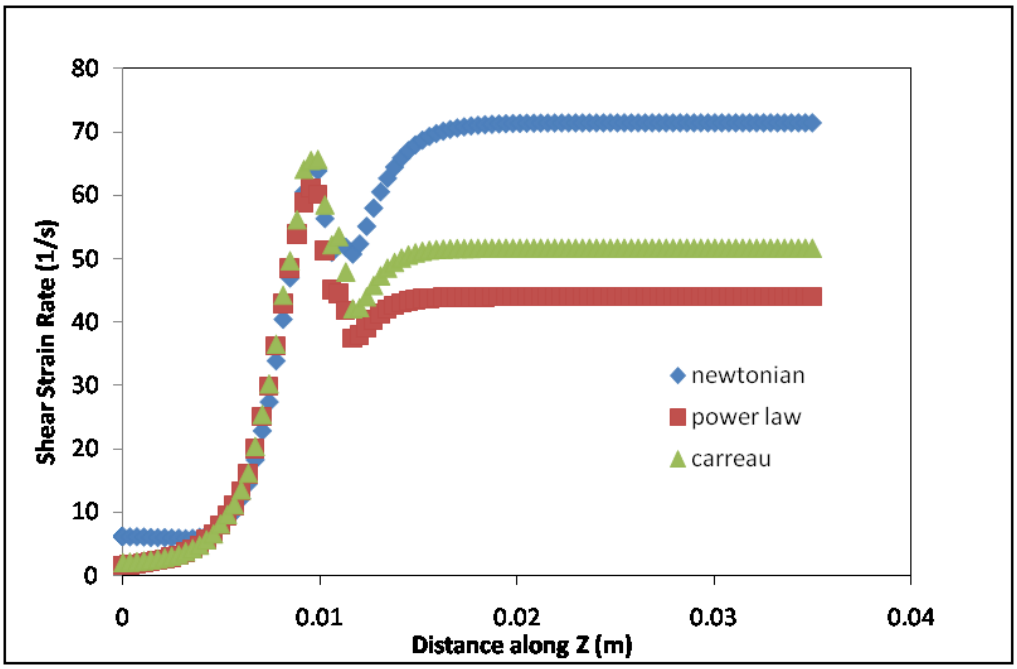

Fig. 2.8: Shear strain rate along the centerline of the catheter

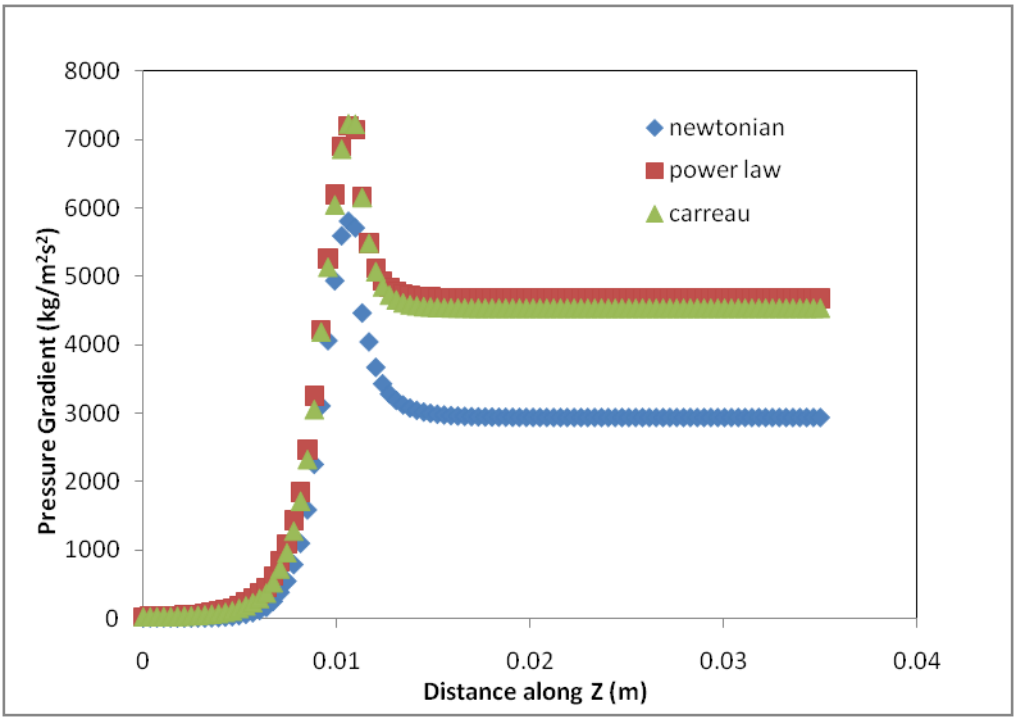

Fig. 2.9: Pressure gradient along the centerline of the catheter

It can be seen that both Newtonian and non-Newtonian flows give similar profile shapes for the pressure gradient and for the strain rate. The Newtonian model gives an upper bound for the strain rate. It is well established that higher strain rates give rise to higher rates of hemolysis. So, for the given conditions, a Newtonian model gives a conservative representation of the flow field with respect to hemolysis and has been chosen for further simulations because of its simplicity. This finding also suggests that when saline injection is to be simulated, it would be sufficient to use a Newtonian viscosity model in conjunction with a mixing rule to determine the viscosity of saline-blood mixtures. For simplicity, an empirical formula which is commonly used to determine the viscosity of fluid blends was applied to determine the viscosity of the saline-blood mixture.

The equation is [88]:

$$\upsilon = \exp^{e^{(Vblend-10.975)/14.524}} - 0.8 \quad (2.5)$$

where:

$$Vblend = [x_a VBN_a] + [x_b VBN_b] \quad (2.5a)$$

$$VBN = 14.534 \ln[\ln(\upsilon + 0.8)] + 10.975 \quad (2.5b)$$

Where υ is the kinematic viscosity (centistokes), and x is the mass fraction.

The duration of each simulation run was equal to the duration of injection period. In all cases, the flow was regarded as laminar with calculated Reynolds numbers of 47 and 188 when a Newtonian viscosity was used with the given flow rates of 10 ml/min and 40 ml/min respectively.

As a check on the accuracy of the numerical simulations, it may first be observed that for fully developed laminar flow of a Newtonian fluid, the friction factor is $f = 64/Re$. To compare this friction factor with that from the simulations, the definition of the friction factor was evaluated by using information extracted from the numerical solutions. The friction factor is defined as

$$f = -\left(\frac{\partial p}{\partial x}\right) d/\left(\frac{1}{2}\rho U^2\right) \qquad (2.6)$$

where $\frac{\partial p}{\partial x}$ is the pressure gradient at the downstream end of the catheter, d is the catheter diameter, ρ is the fluid density, and U is the mean fluid velocity.

By use of the results from the numerical solutions, it is found that $f = 1.37$ for a flow rate of 10ml/min. From the theoretical solution, $f = 64/Re = 1.36$. The agreement between these two values is within 0.74 %.

2.2.1e Further results for Newtonian flow

Pressure drop and shear stress

The effects of flow rate and port geometry on the pressure drop and maximum shear stress are summarized in Table 2.2. The listed results correspond to the steady state that was achieved prior to the termination of the two-second run period.

An inspection of the pressure drop results listed in Table 2.2 shows a remarkable similarity between those for Ports A and B. On the other hand, the pressure drops for Port

C are approximately 80% of those for the other ports. This reduction in pressure drop can be attributed to a better geometric design for Port C. In truth, however, this small reduction in pressure does not provide any practical advantage.

Table 2.2: Pressure drop and maximum shear stress in the fluid domain at different flow rates

No.	**Port**	**Flow rate**	**Maximum shear stress**	**Pressure drop**
1	A	10	3.9	113
2	A	40	24	586
3	B	10	4.5	113
4	B	40	25	588
5	C	10	7.2	89
6	C	40	30	490

Further insights into the mechanisms that contribute to the pressure drop results can be obtained by noting that an increase in flow rate by a factor of four gives rise to a pressure drop increase that is larger than a factor of four. The flow in the catheter is more or less fully developed throughout (horizontal lines in Fig. 2.9) and fully developed pressure drops do scale linearly with the flow rate for laminar flow. On the other hand, the inertial-based pressure losses in the reservoir are non-linear and give rise to a larger-than-linear pressure loss.

Next, attention may be turned to the maximum shear stress results of Table 2.2. The maximum shear stress in the fluid domain is found to occur within the reservoir near the fluid injection port. When considering these results, it is important to recognize that they are local. Therefore, they are subject to the local nature of the mesh. As a consequence, they should not be regarded as having the same level of fidelity as would characterize overall results such as the end-to-end pressure drops that are also listed in Table 2.2. However, the issue of the accuracy level is moot when looked at with respect to the context of hemolysis. It can be demonstrated that the shear stress values listed in the table are far below the threshold at which hemolysis occurs. This demonstration will be implemented with the aid of Fig. 2.10 [80,81, 89-99].

Figure 2.10 shows a summary of results available in the literature which gives the relationship between shear stress level and hemolysis. It shows the time required to induce hemolysis at different magnitudes of shear stress. The figure indicates that hemolysis is unlikely to occur at shear stresses below 100 Pa. Since the values of shear listed in Table 2.2 are considerably lower than 100 Pa, it may be concluded that none of the ports investigated gives rise to a high-enough shear stress to cause hemolysis at the given flow rates.

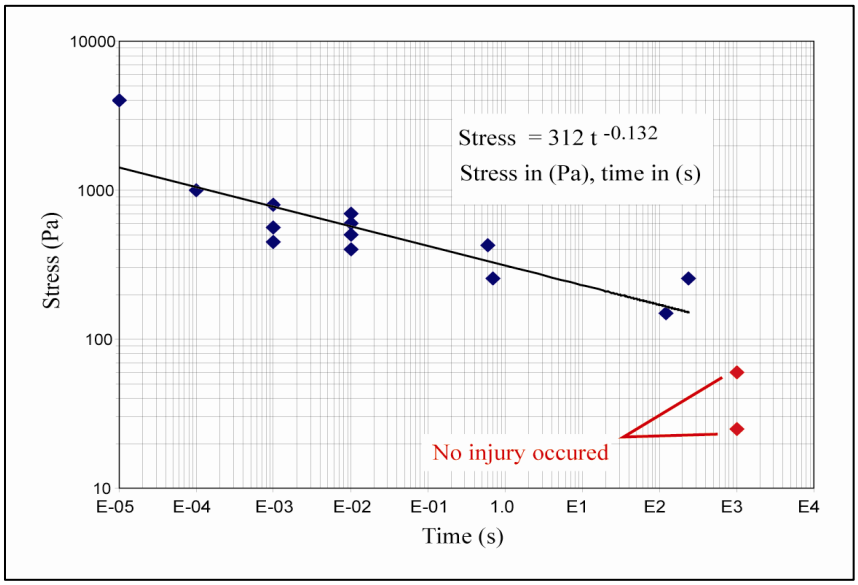

Fig.2.10[80,81, 89-99]: Relationship between shear stress level and hemolysis

Streamlines and Vector Diagrams

Streamlines and vector diagrams provide a means for visualizing the flow pattern in the reservoirs. Figures 2.11(a), 2.11(b) and 2.11(c) show the three-dimensional streamlines originating from the inlet in ports A, B and C configurations, respectively. Since the flow becomes steady, these lines also represent the pathlines. It can be seen from these figures that the streamlines are twisted near the inlet of the catheter for Ports A and B due the sudden change of cross section. On the other hand, the twist is much less pronounced for Port C. Another feature that distinguishes Port C from the others is that its coiled flow pattern in the reservoir is not as tightly knotted as the rest.

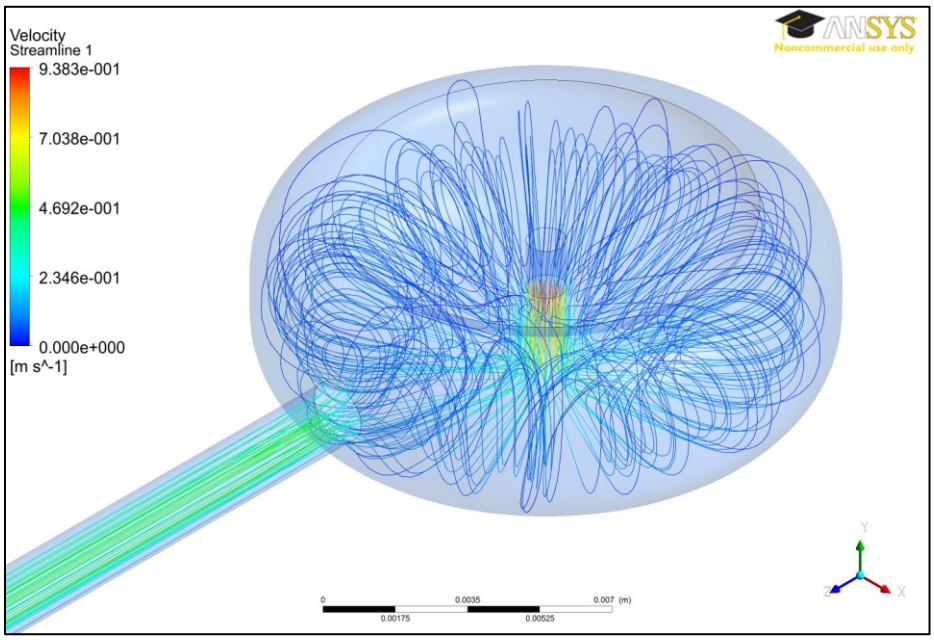

Fig. 2.11(a): Three-dimensional streamlines originating from inlet of Port A

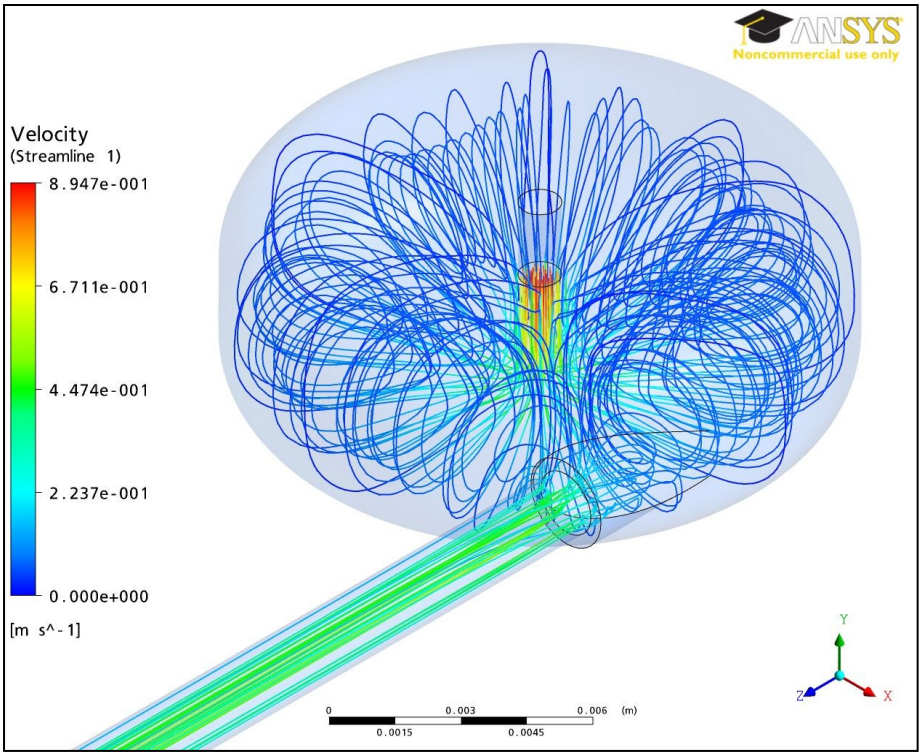

Fig. 2.11(b): Three-dimensional streamlines originating from inlet of Port B

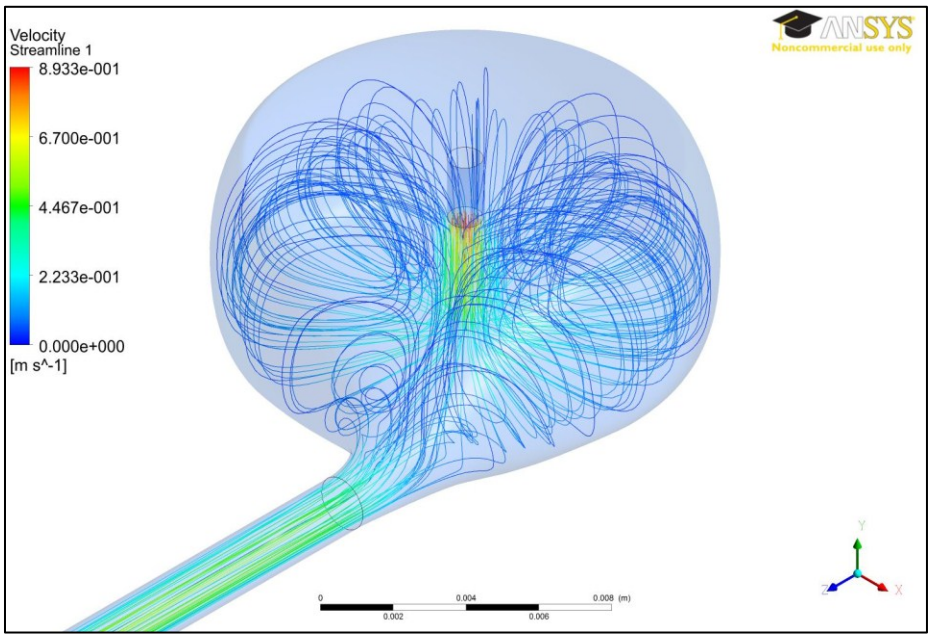

Fig. 2.11(c): Three-dimensional streamlines originating from inlet of Port C

The degree of smoothness experienced by the flow passing from the reservoir into the catheter is clearly displayed by the vector diagrams shown in Figs. 2.12(a), 2.12(b) and 2.12(c). Examination of Fig. 2.12(a), Port A, shows the streamlines bending sharply as they negotiate what is nearly a 90-degree change of direction. Since the Reynolds number of the flow is very low, such a sharp change is able to occur without flow separation. Figure 2.12(b) indicates the presence of a recirculation zone for Port B. In general, recirculation zones may bring on hemolysis. However, in the present situation, the flow velocities are so low that hemolysis does not occur. In addition, a recirculation zone is filled with a captive fluid which does not exit the catheter. It may be speculated that particulates could congregate in the captive fluid and cause agglomeration. Figure 2.12(c)

corresponds to Port C. The passage of the flow from the reservoir into the catheter follows smoothly converging streamlines and may be regarded as ideal.

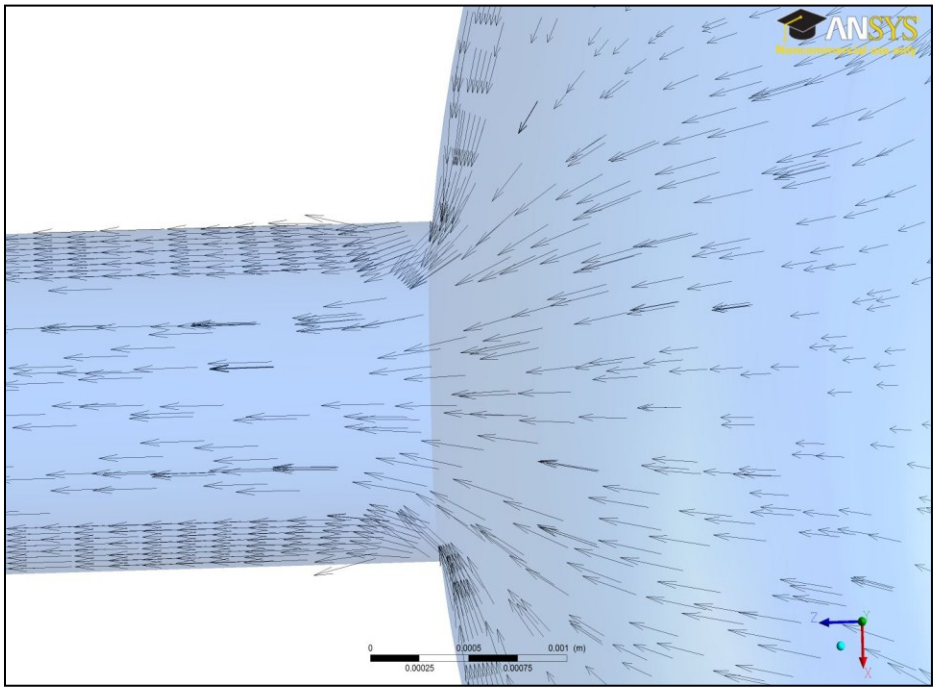

Fig. 2.12(a): Velocity vectors at the entrance of the catheter for Port A

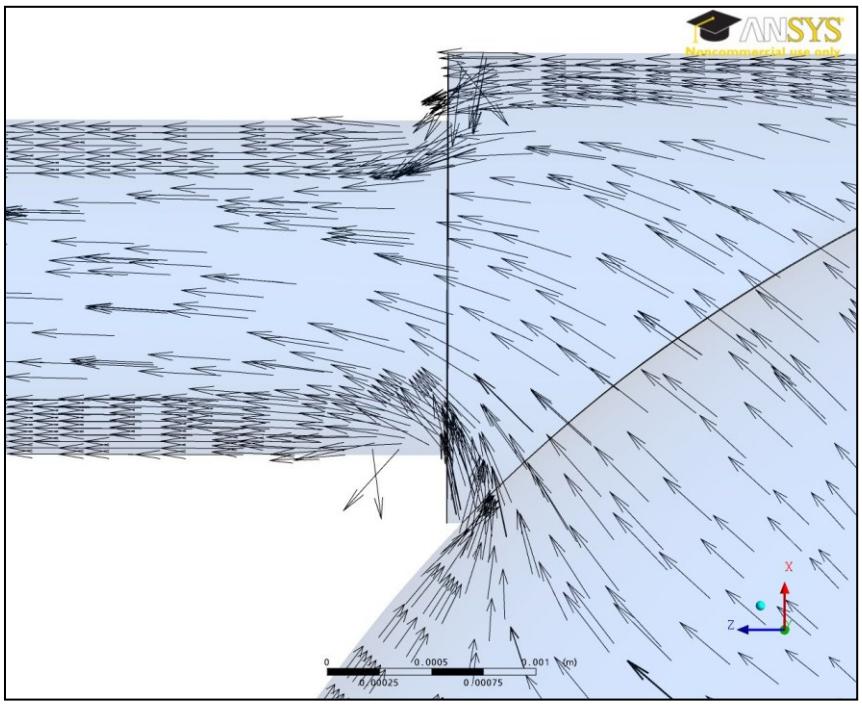

Fig. 2.12(b): Velocity vectors at the entrance of the catheter for Port B

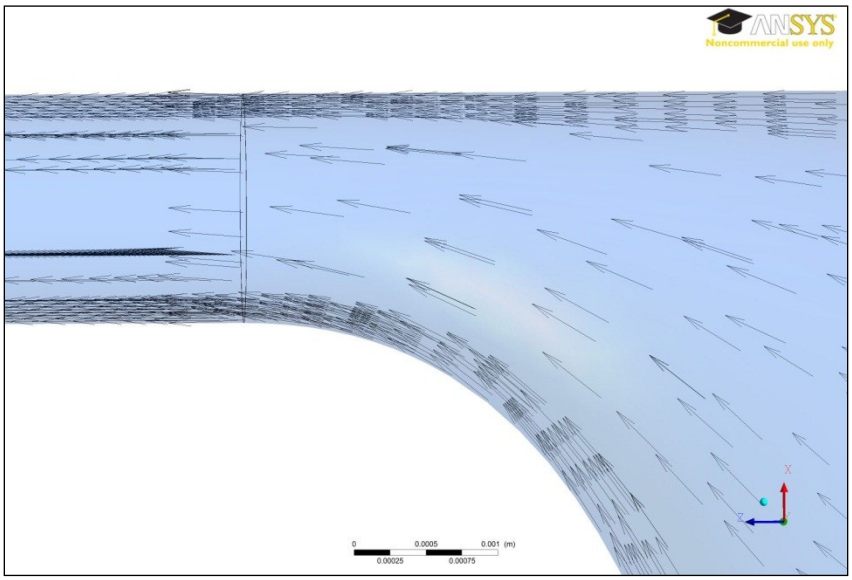

Fig. 2.12(c): Velocity vectors at the entrance of the catheter for Port C

2.2.2 Mass transfer between blood and saline

2.2.2a Governing equations

If the quantity C represents the concentration of a diffusing species in another medium, the species conservation equation is

$$u\frac{\partial C}{\partial x} + v\frac{\partial C}{\partial y} + w\frac{\partial C}{\partial z} = D\left[\frac{\partial^2 C}{\partial x^2} + \frac{\partial^2 C}{\partial y^2} + \frac{\partial^2 C}{\partial z^2}\right] \tag{2.7}$$

where D is the binary diffusion coefficient. The mass transfer is solved by utilizing the heat-mass transfer analogy. The governing equation for convective heat transfer has the form:

$$\rho c_p\left[\frac{\partial T}{\partial t} + u\frac{\partial T}{\partial x} + v\frac{\partial T}{\partial y} + w\frac{\partial T}{\partial z}\right] = k\left[\frac{\partial^2 T}{\partial x^2} + \frac{\partial^2 T}{\partial y^2} + \frac{\partial^2 T}{\partial z^2}\right] \tag{2.8}$$

In this equation, T is the temperature, k is the thermal conductivity, and c_p is the specific heat at constant pressure. The two foregoing equations can be brought into congruence by a simple transformation:

$$T \rightarrow C,\ c_p = 1/\rho,\ and\ k = D \tag{2.9}$$

By this transformation, the species conservation equation can be solved by CFX as if it were a heat convection equation. A value of 1.5e-9 m^2/s was used as the binary diffusion co-efficient. This value is consistent with the measured values for saline in biological tissues [100]. Since typically used saline solutions have a salt mass fraction of 0.9%, properties of pure water was used to represent the saline

The boundary conditions for the mass transfer problem are: (a) no mass transfer at any solid surface, (b) given value of C at the inlet of the solution domain, and (c) standard weak boundary conditions at the exit of the catheter. Initially, C = 0 throughout the solution domain.

2.2.2b Mass transfer results

The results of the mass transfer simulations will be conveyed by means of concentration contour diagrams. The displayed concentration is that of the injected fluid. A concentration C = 1 at a point means that the fluid at that point is totally injected fluid. On the other hand, C = 0 signifies the total absence of the injected fluid. In that case, the fluid is that which originally occupied the reservoir and the catheter, hereafter referred to as the incumbent fluid. The presented concentration information is for the steady state. The color strip at the left of each contour diagram provides the relationship between the colors and the magnitudes of C.

The in-reservoir results for each of the ports are presented in a pair of figures, respectively Figs. 2.13(a) and (b) for Port A, Figs. 2.14(a) and (b) for Port B, and Figs. 2.15(a) and (b) for Port C. Both the (a) and (b) parts of each figure are focused on the reservoir, but display different views. The (a) parts show the concentration contours in a plane that is perpendicular to the top and bottom surfaces of the reservoir and includes the geometric axis of the catheter. The (b) part of each figure displays contours in a plane

that is perpendicular to that used to define the (a)-part results. The part-(b) plane lies at the half-height of the reservoir.

Inspection and comparison of the three (a)-part figures show the degree of coherence of the injected fluid as it mixes with the incumbent fluid. For Port B, the injected fluid experiences little mixing as it moves downward along the centerline of the reservoir. For Port A, there is slightly more mixing along this path. In contrast, for Port C, there is considerably more mixing between the injected and incumbent fluids as the former makes its way downward along the centerline of the reservoir.

The injected fluid dead-ends against the bottom of the reservoir and then fans outward along the bottom surface. The flaring is quite symmetric for Port A, but less so for Ports B and C.

The main observation from the part-(a) figures is the degree of mixing of the injected and incumbent fluids. In this regard, it is abundantly clear that the geometry of Port C gives rise to the best mixing.

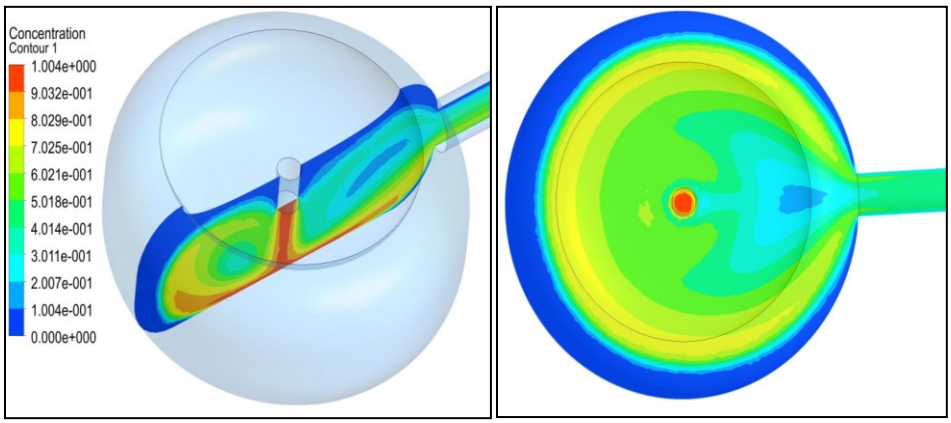

(a) *(b)*

Fig. 2.13(a): Concentration contour along a plane perpendicular to the reservoir top and bottom surfaces for Port A, (b) Concentration contour along a plane perpendicular to the fluid injection and located at reservoir half-height for Port A

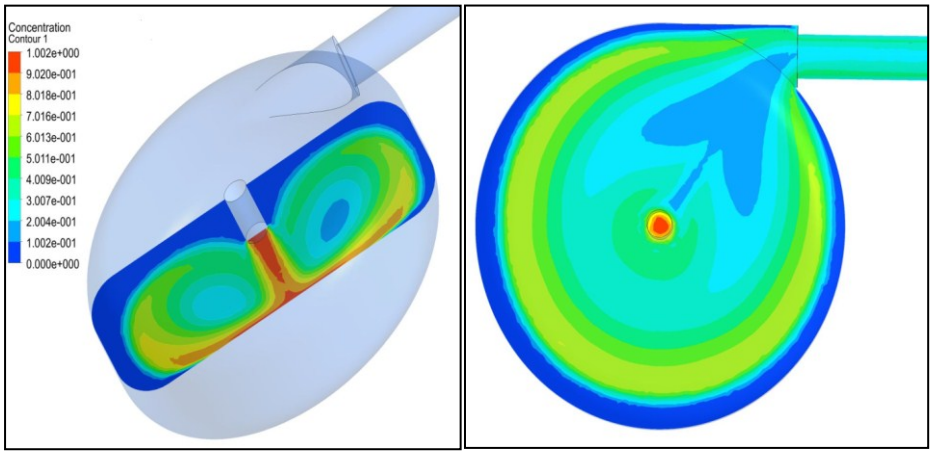

(a) *(b)*

Fig. 2.14(a): Concentration contour along a plane perpendicular to the reservoir top and bottom surfaces for Port B, (b) Concentration contour along a plane perpendicular to the fluid injection and located at reservoir half-height for Port B

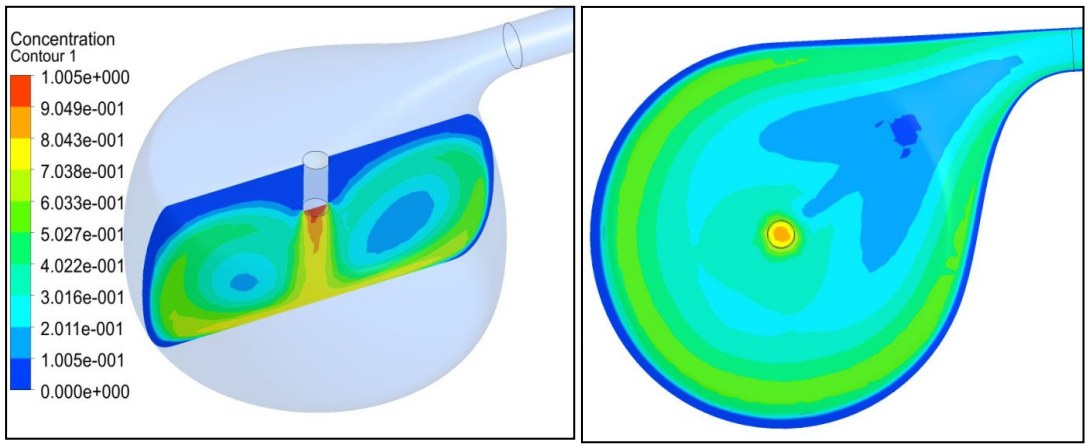

(a) *(b)*

Fig. 2.15(a): Concentration contour along a plane perpendicular to the reservoir top and bottom surfaces for Port C, (b) Concentration contour along a plane perpendicular to the fluid injection and located at reservoir half-height for Port C

The part-(b) figures confirm the hierarchy of mixing for the various ports. From most mixing to least mixing, the ports are ordered as C, A and B. Further observation of the part-(b) figures reveals an arrow-shaped blue-colored formation, with the arrow pointing from the center of the reservoir toward the exit. This formation is clearly in evidence for Ports A and C and to lesser extent for Port B. The contour strip identifies these zones as containing primarily incumbent fluid.

Three additional figures, 2.16, 2.17, and 2.18, will now be presented to convey mass concentration information for the catheter. Each of these figures is made up of three circles, each of which represents a cross section of the catheter. From left to right, the

respective circles correspond to the catheter inlet, the catheter half length, and the catheter exit.

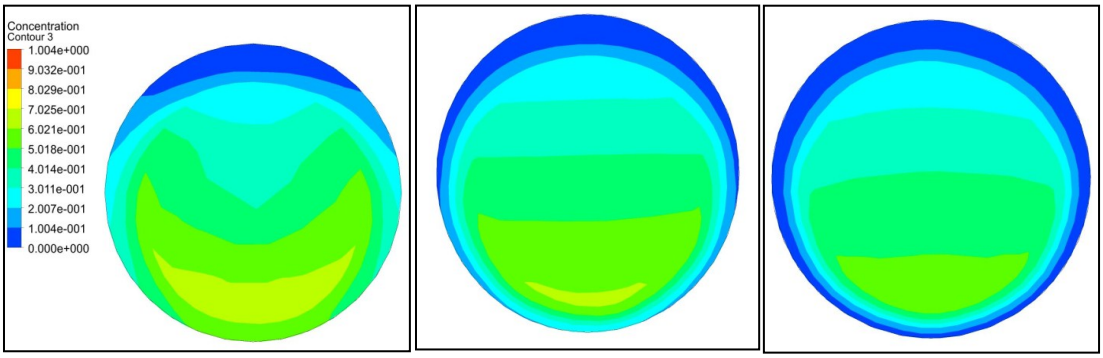

(a) *(b)* *(c)*

Fig. 2.16: Concentration contours in cross-sectional planes near the inlet (a), half-length (b) and outlet (c) of the catheter for Port A

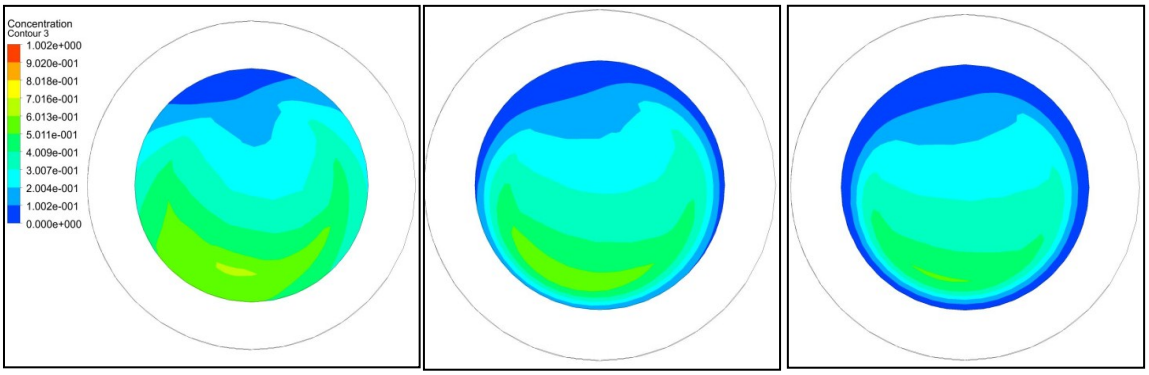

(a) *(b)* *(c)*

Fig. 2.17: Concentration contours in cross-sectional planes near the inlet (a), half-length (b) and outlet (c) of the catheter for Port B

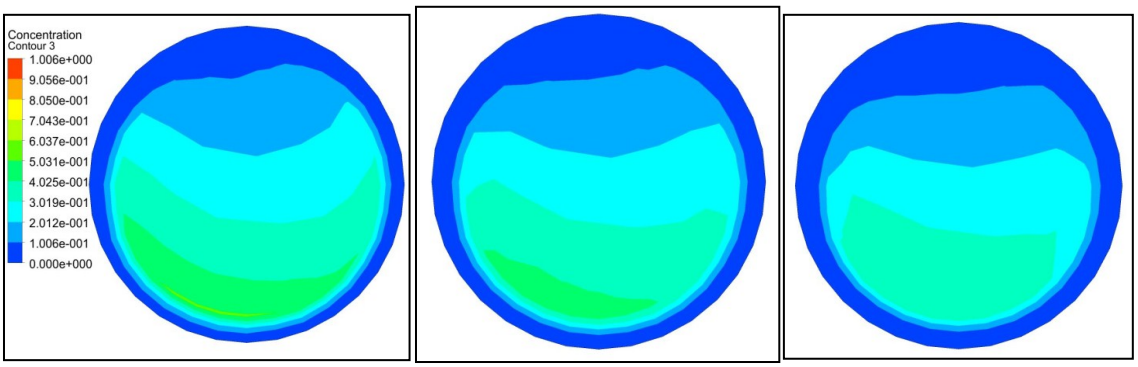

(a) *(b)* *(c)*

Fig. 2.18: Concentration contours in cross-sectional planes near the inlet (a), half-length (b) and outlet (c) of the catheter for Port C

For Port B, Fig. 2.17, there is clear evidence that mixing occurs along the length of the catheter. At the exit cross section, the concentration is generally homogeneous, but the incumbent fluid still dominates adjacent to the wall. Progressive mixing is also in evidence for Port A (Fig. 2.16), but the concentration is less uniform at the exit cross section than that observed for Port B. The results for Port C, Fig. 2.18, display little lengthwise evolution. The concentration at the exit cross closely resembles that for Port B.

2.2.3 Flow of a homgenous fluid for dialysis applications

The flow rates listed in Table 2.1 would be representative of flow rates which are likely to be encountered when fluid is injected into the reservoir using a syringe. For dialysis applications, both the inlet and outlet of the reservoir would be connected to catheters which, in turn, would be connected to a pump to deliver/remove blood to/from the

reservoir. Typical flow rates used in dialysis range between 150 ml/min and 450 ml/min. With some modifications, the methodology used in Section 2.2.1 can be applied to simulate flows at these rates. The Navier Stokes equations discussed in Section 2.2.1B need to be modified to account for turbulence which may arise at higher flow rates. Since dialysis involves both delivery and removal of blood, it is also important to evaluate the port in reverse flow direction.

2.2.3a Governing equations for flow of a homgenous fluid at higher flow rates

To account for turbulence, the Reynolds-Averaged Navier Stokes (RANS) equations need to be solved. These equations are:

x-momentum:

$$\rho\left(\frac{\partial u}{\partial t}+\frac{\partial u^2}{\partial x}+\frac{\partial uv}{\partial y}+\frac{\partial uw}{\partial z}\right)=-\frac{\partial p}{\partial x}+\frac{\partial}{\partial x}\left[(\mu+\mu_t)\frac{\partial u}{\partial x}\right]+\frac{\partial}{\partial y}\left[(\mu+\mu_t)\frac{\partial u}{\partial y}\right]+\frac{\partial}{\partial z}\left[(\mu+\mu_t)\frac{\partial u}{\partial z}\right] \tag{2.7}$$

y-momentum:

$$\rho\left(\frac{\partial v}{\partial t}+\frac{\partial v^2}{\partial y}+\frac{\partial vw}{\partial z}+\frac{\partial vu}{\partial x}\right)=-\frac{\partial p}{\partial y}+\frac{\partial}{\partial y}\left[(\mu+\mu_t)\frac{\partial v}{\partial y}\right]+\frac{\partial}{\partial z}\left[(\mu+\mu_t)\frac{\partial v}{\partial z}\right]+\frac{\partial}{\partial x}\left[(\mu+\mu_t)\frac{\partial v}{\partial x}\right] \tag{2.8}$$

z-momemtum:

$$\rho\left(\frac{\partial w}{\partial t}+\frac{\partial w^2}{\partial z}+\frac{\partial wu}{\partial x}+\frac{\partial wv}{\partial y}\right)=-\frac{\partial p}{\partial z}+\frac{\partial}{\partial z}\left[(\mu+\mu_t)\frac{\partial w}{\partial z}\right]+\frac{\partial}{\partial x}\left[(\mu+\mu_t)\frac{\partial w}{\partial x}\right]+\frac{\partial}{\partial y}\left[(\mu+\mu_t)\frac{\partial w}{\partial y}\right] \tag{2.9}$$

In addition to conservation of momentum, mass conservation has to be satisfied by solving the incompressible continuity equation given by:

$$\frac{\partial u}{\partial x} + \frac{\partial v}{\partial y} + \frac{\partial w}{\partial z} = 0 \quad (2.10)$$

The quantity μ_t appearing in the RANS equations is called the *turbulent viscosity.* It is assumed to be isotropic, but depends on the coordinates *x, y*, and *z*. The values of μ_t are obtained from turbulence models.

A wide array of literature on turbulent flow modeling has demonstrated that RANS-based turbulence models are appropriate for the determination of μ_t values that lead to accurate solutions [101-103] for pipe flows. Numerous models which solve for the turbulent viscosity have been developed and reviewed in literature [38]. Here, the Shear Stress Transport (SST) model used in conjunction with the RANS equations was chosen because it incorporates the near-wall competence of the k-ω model and the far-from-wall competence of the k-ε model [42-44]. At low Reynolds numbers, the results obtained from the SST turbulence model resemble those of that obtained from laminar flow models.

2.2.3c Flow results in forward direction

Pressure Drop

Higher pressure drops indicate greater resistance to the fluid flow and hence require more pump work**.** A plot of flow rate versus pressure drop between the inlet of the reservoir and the catheter exit for Ports A-C is shown in Figure 2.19. Port C exhibited a lower

pressure drop than either of Ports A or B, indicating a lowered resistance to fluid flow and diminished pumping power. While assessing these results, it is important to remember (from Table 2.1) that the volumes of all the ports were not the same. However, the lower pressure drop for Port C can be attributed to better design and not higher volume. If diminished pressure were due to volume size alone, the difference in pressure drop would be evident at all flow rates.

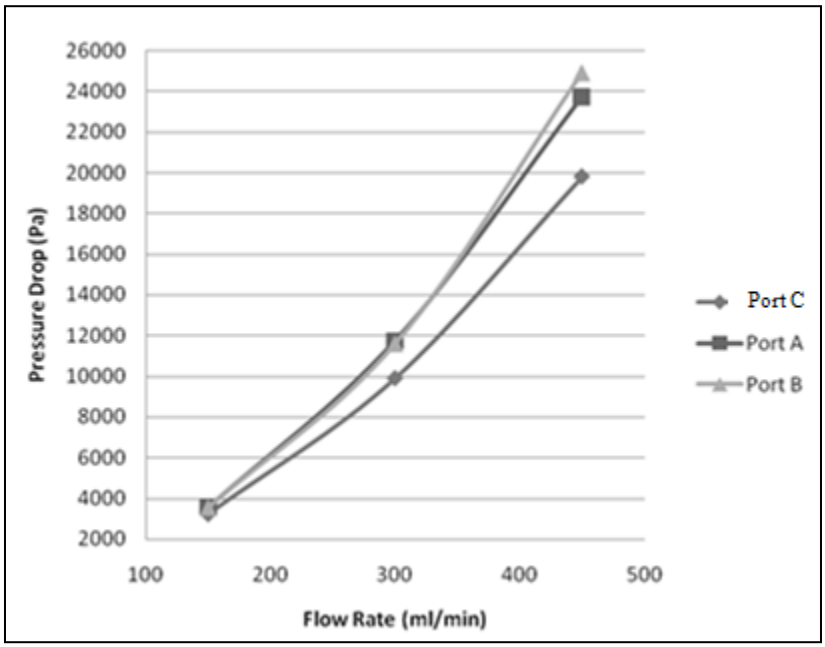

Fig. 2.19: Pressure drop v/s flow rate in forward flow direction

Streamlines and Vector Diagrams:

The streamlines and vector diagrams for the three ports at higher flow rates are very similar to those obtained at lower flow rates already conveyed in Figures 2.11(a) – 2.11(c) and Figures 2.12 (a) – 2.12 (c). The conclusion drawn from the flow patterns at

lower flow rates which indicate more ideal flow characteristics for Port C are also applicable here at higher flow rates. To avoid repetition, streamlines and vector diagrams for the three ports in forward direction at a higher flow rate (450 ml/min) are depicted in Appendix A.

2.2.3d Flow results in reverse direction

To simulate the removal of blood from the port, the inlet of the reservoir (depicted earlier in Figure 2.1) has been extended outwards to represent a section of a catheter which would be used to remove blood from the port. The diameter of the catheter was taken to be 1 mm and 7 mm length of the catheter was included in the solution domain. An outlet boundary condition with a fixed mass flow rate is applied at the tip of the extended section of the solution domain. The modified solution domain for reverse flow conditions along with the three-dimensional streamlines at a flow rate of 150 ml/min for various ports are presented in Figures 2.20(a) to 2.20(c).

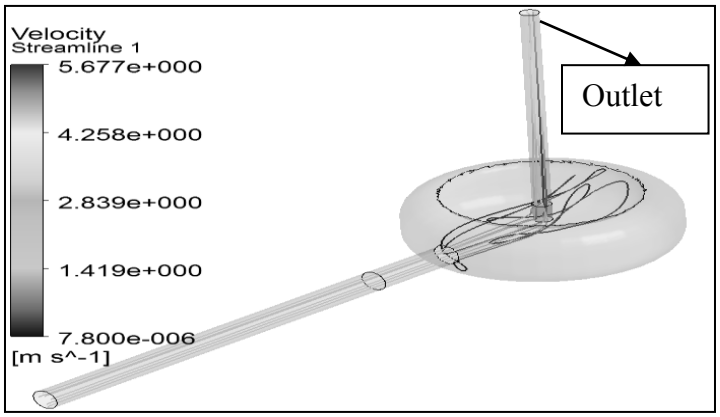

Fig. 2.20(a): Three-dimensional streamlines for the Port A with reverse flow of 150ml/min

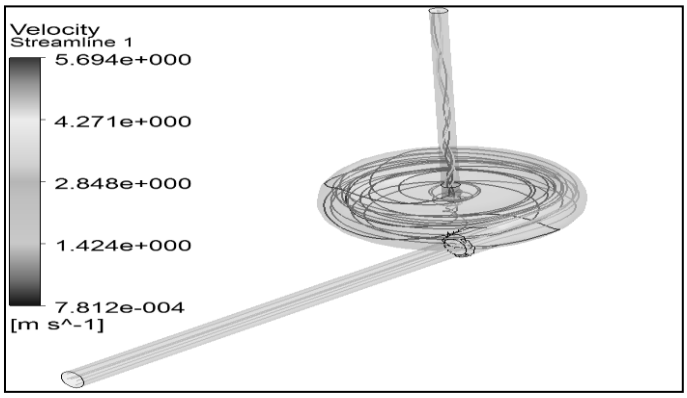

Fig. 2.20(b): Three-dimensional streamlines for the Port B with reverse flow of 150ml/min

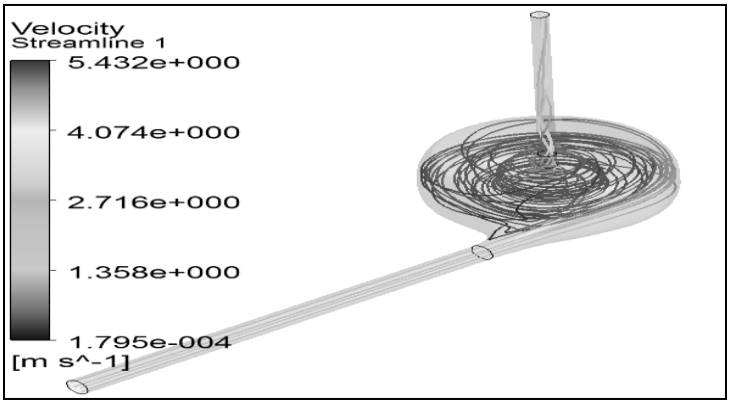

Fig. 2.20(c): Three-dimensional streamlines for the Port C with reverse flow of 150ml/min

It is evident from the streamlines in Figures 2.20(a) – 2.20(c) that a tangential entrance of fluid into the reservoir as exhibited by Ports B and C is much more desirable if the entering fluid is to traverse the entire reservoir volume before exiting through the other

catheter. Such a design would lead to much better flushing of the reservoir while minimizing stagnation zones.

Figure 2.21 shows the pressure drop between the inlet and outlet of the reservoir in the reverse flow mode. It can be seen from the figure that the tapered tangential entrance of Port C leads to a much lower resistance to flow than does Port B. Port A also exhibits a lower pressure drop similar to that of Port C. This outcome is mainly due to the fact that the fluid entering the reservoir in the case of Port A does not traverse the entire volume of the port, a situation which is more likely to lead to stagnation zones which increase the likelihood of thrombosis.

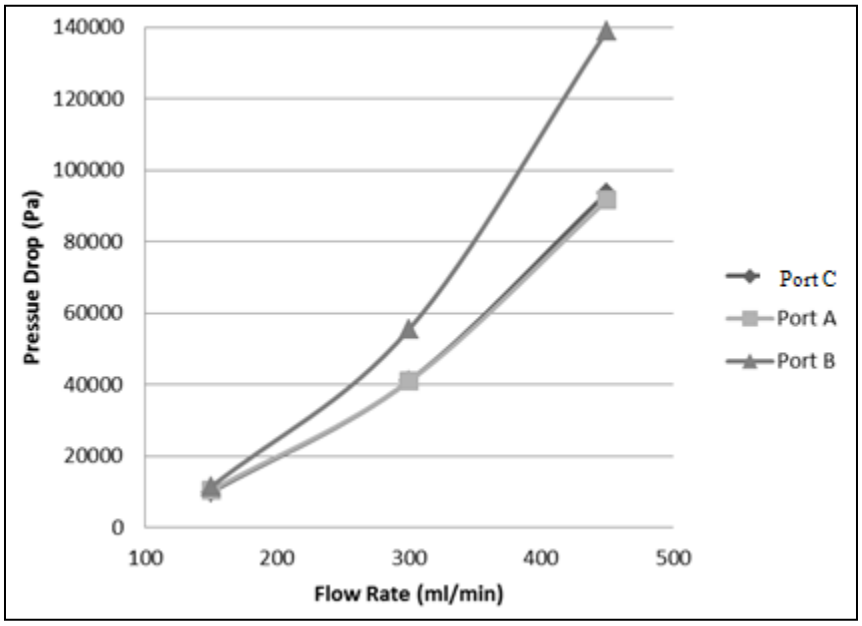

Fig. 2.21: Pressure drop in the reservoir plotted against flow rate for the three access ports operating in the reverse direction

2.2.3e Effect of volume-reducing-members on the flow characteristics of infusion ports

There are filed patents [104] which claim the use of volume-reducing-members as an effective means of lowering pressure drop in implantable infusion ports. The purpose of this section is to explore the efficacy of incorporating such features into the design of the proposed Port C. Figure 2.22 shows the modified geometry of Port C with volume-reducing-members on the left and the unmodified geometry on the right, along with their corresponding streamlines in the forward direction. The internal volume of the reservoir could be minimized by placing inert beads in the reservoir, or by manufacturing the reservoir with internal protrusions. Figure 2.23 is similar to Figure 2.22 but the streamlines are for the reverse flow direction.

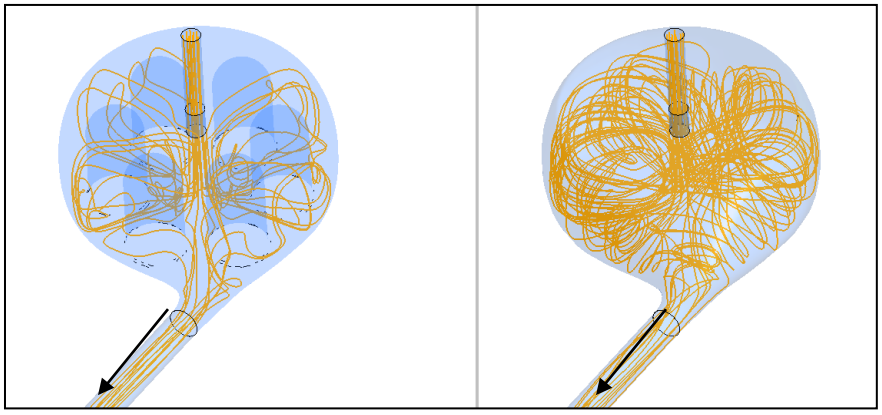

(a) *(b)*

Fig. 2.22: Three-dimensional streamlines for Port C in forward flow with (a) and without (b) volume-reducing-members

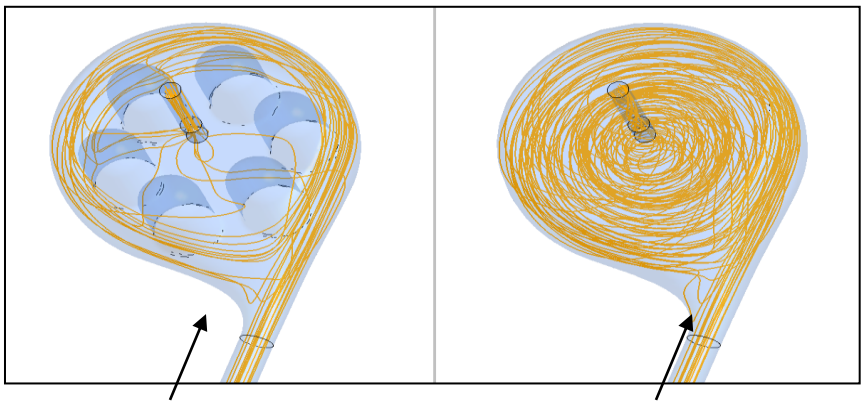

(a) (b)

Fig. 2.23: Three-dimensional streamlines for Port C in reverse flow with (a) and without (b) volume-reducing-members

It can be surmised from figures 2.22 and 2.23 that the presence of volume-reducing-members leads to more undesirable flow patterns with increased likelihood of stagnation zones behind these members. Table 2.3 summarizes the effect of the volume-reducing-members on the pressure drop inside the reservoir.

Table 2.3: Pressure drop in Port A and Port C with and without volume-reducing-members in both forward and reverse directions at a flow rate of 150 ml/min

Port	Flow Direction	Volume-reducing Members	Pressure Drop (Pa)
Port C	Forward	Present	1425
Port A	Forward	Absent	1510
Port C	Reverse	Present	8817
Port A	Reverse	Absent	9838

It can be seen that there is a small benefit in terms of lower pressure drop with the presence of volume-reducing-members. However, this reduction in pressure drop would be negligible relative to the overall pressure drop across the entire dialysis system. The potential risks associated with the undesirable flow patterns in the presence of volume-reducing-members would far outweigh the small pressure drop benefit that comes with the volume-reducing features. Two-dimensional streamlines, velocity contour plots, and vector diagrams for different cross sections of the port can be used to provide further insight into undesirable flow patterns caused by volume-reducing members. These visual aids would essentially convey the same information as that of the three-dimensional streamlines in Figures 2.22 and 2.23 and have been confined to Appendix B for the sake of brevity. A similar analysis of the effect of volume-reducing members on the performance of Port A also yielded the same conclusions and those results are also included in Appendix B.

Chapter 3

USE OF THE COANDA EFFECT TO OPTIMIZE THE PRODUCTION OF BIO-MEDICAL FILTRATION MEDIA

3.1 Introduction

As stated in Chapter 1, the goal of this chapter is to investigate the use of the Coanda Effect to optimize the melt-blowing process which is used to produce nanofibers for making biomedical filtration media. The melt-blowing process is the most common process used for producing non-woven fibers and its operating principle and applications have been briefly discussed in Chapter 1. This chapter is devoted to invoking the Coanda Effect to modify the air flow patterns occurring in the melt-blowing process to alter the properties of media produced by the process.

The Coanda Effect is a result of entrainment of ambient fluid by a jet. A surface that is brought in close proximity to the jet restricts the entrainment of fluid in that region. As the flow accelerates to try to balance the momentum transfer, a pressure difference across the jet results, and the jet is deflected closer to the surface, eventually attaching to it. The impact of the Coanda Effect is widespread both in technological and natural phenomena. It has important applications in high-lift devices on aircraft, where air moving over the wing can be "bent down" towards the ground using flaps. The Coanda-affected flow from a wing-mounted jet engine produces enhanced lift by dramatically

increasing the velocity gradient in the shear flow in the boundary layer. In this velocity gradient, fluid particles are blown away from the surface, thus lowering the pressure there. In air conditioning, the Coanda principle is exploited to increase the throw of a ceiling-mounted diffuser. Because the Coanda Effect causes air discharged from the diffuser to adhere to the ceiling, it travels farther before dropping. In cardiovascular medicine, the Coanda effect accounts for the separate streams of blood in the fetal right atrium. It also explains why eccentric mitral regurgitation jets are attracted and dispersed along adjacent left atrial wall surfaces. In meteorology, the Coanda theory has also been used to explain air streams that flow out of mountain ranges.

In most physical situations in which the Coanda Effect is encountered, the neighboring surface is convex. In a very limited category of applications, the effect is observed in the presence of flat surfaces. In one such application, Miozzi et al. [105] have experimentally investigated the use of a flat lateral wall to control the direction of water flowing from a river into the sea. To better understand and illustrate the physics of the Coanda Effect, a simple preliminary numerical model of a situation similar to the one explored by Miozzi et al. has been developed and shown in Figure 3.1. The figure shows streamlines emerging from a narrow channel delivering a fluid to a wide open chamber. The diagram on the left (Figure 3.1(a)) shows a case where both the sides and downstream end of the chamber are left open while, the right-hand diagram shows a case in which a lateral wall is placed on one of the sides to alter the direction of the fluid flow. In the absence of a lateral wall, it would be expected that the fluid flow would be symmetric as shown in

Figure 3.1(a). When a lateral wall is present, uninformed intuition would lead to the expectation that fluid would take the path of least resistance and flow towards the open end to avoid the additional resistance caused by the wall. However, due to the presence of the Coanda Effect, the emerging fluid jet is deflected towards the direction of the lateral wall as seen by the streamlines in Figure 3.1(b).

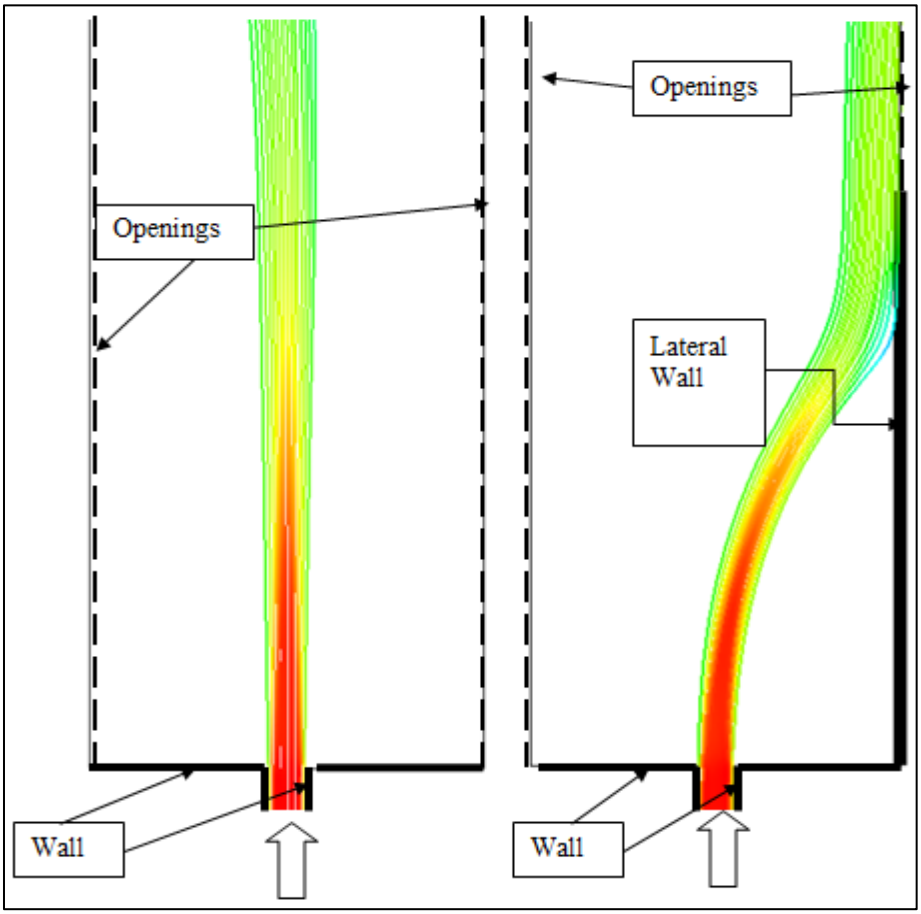

(a) *(b)*

Fig. 3.1: Solution domain and streamlines to show the presence of the Coanda-effect (a) Case with open sides (no Coanda Effect) (b) Case with lateral wall to induce Coanda Effect

To explain the deflection of the streamlines towards the lateral wall in Figure 3.1(b), Figure 3.2 has been prepared. Figure 3.2 displays velocity vectors corresponding to the situations depicted in Figure 3.1. It can be seen from Figure 3.2(a) that for the case where no lateral wall is present, the emerging jet entrains fluid from both the open sides resulting in symmetric flow about the center of the channel. In Figure 3.2(b), the presence of the lateral wall restricts the entrainment of the surrounding fluid as it adheres to the wall due to the no-slip condition, resulting in the creation of a recirculation zone which directs the jet towards the wall.

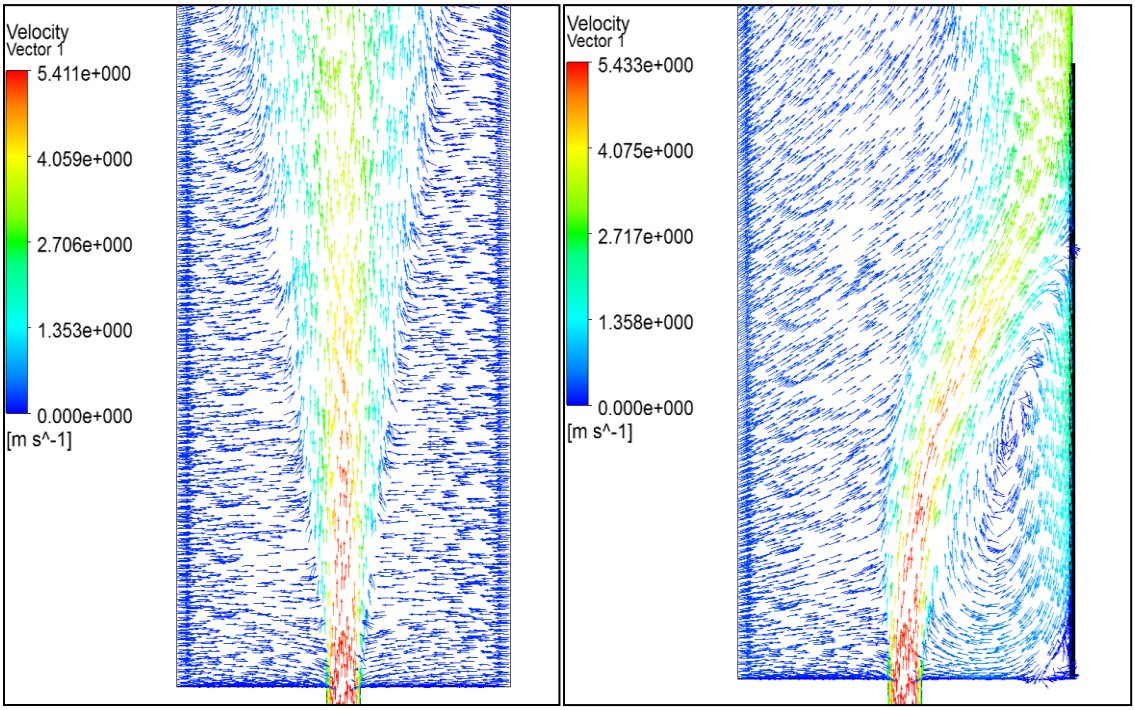

(a) *(b)*

Fig. 3.2: Velocity vectors corresponding to Figure 3.1

Now that the Coanda Effect in presence of a plane lateral wall has been demonstrated by a numerical model, the remainder of the chapter is focused on invoking the Coanda Effect by utilizing lateral walls to alter the trajectories of nanofibers during the meltblowing process. A later section of the chapter is devoted to comparing the effectiveness of plane walls to that of curved walls in invoking the Coanda Effect.

3.2 Problem definition

In this section, a novel and heretofore unrecognized use of the Coanda Effect will be quantitatively explored. It is proposed to use the Coanda Effect to enhance the production of fine fibers by the melt-blown method [106-110]. According to that method, a still-molten polymer is forced through each of an extensive linearly-deployed array of fine-diameter apertures. The thus-created fiber strands emerge from the die into an environment where high-speed, parallel-flowing air jets exert friction forces that stretch the fiber. The thus-produced fibers are collected at a target surface situated parallel to the plane to the fiber-producing apertures. A schematic side view of the just described melt-blown-process setup is presented in Figure 3.3.

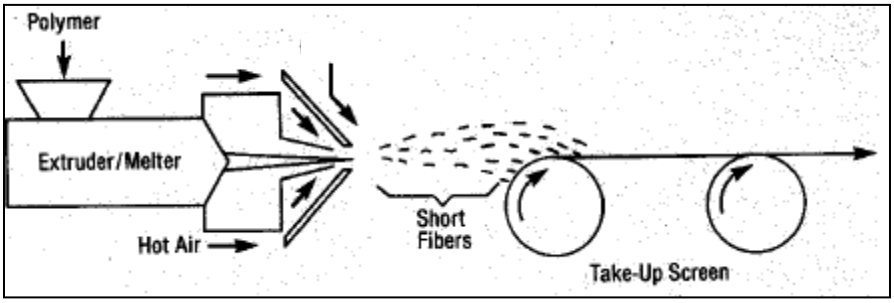

Fig. 3.3: Schematic side view of a melt-blown fiber production setup

As can be seen in the figure, polymer grains are introduced into a melter/extruder whereafter the melted polymer is delivered to a die. The die is extensive in the direction perpendicular to the plane of the figure. The figure displays a typical cross section of the die. Seen there is a single converging flow passage through which the molten polymer is forced and from which it emerges as a still-molten fiber. Also shown in the figure are compartments which serve as plenum chambers whose narrow exits create slot jets of hot, high-velocity air. The friction drag created by the interaction of the air jets with the emerged fiber serves to stretch it longitudinally and reduce its diameter [111]. The air jets entrain cooler, quiescent air from the surroundings, with the result that the jets broaden and decelerate. The processes of jet cooling and deceleration occur simultaneously with the hardening of the fiber. The solidified polymer strands are shown traversing the space between the fiber-producing equipment and the collection apparatus (a rotating take-up screen). Momentum possessed by the fibers is sufficient to carry them to the rotating take-up roll.

In general, the produced fibers impinge uniformly on the take-up roll. However, the trajectories of the fibers emerging from the outboard ends of the fiber-producing equipment carries them inboard of the ends of the take-up rolls, thereby producing a thicker mat with deleterious properties. It is proposed here to use the Coanda Effect to alleviate the aforementioned localized over-thickening of the mat of captured fibers.To investigate the use of the Coanda Effect as a means of modifying the trajectories of the fibers produced at the ends of the equipment, numerical simulation will be used to guide

the positioning of surfaces to be used to create the Coanda Effect. Furthermore, since planar surfaces are the simplest ones to implement in practical equipment, the action of such surfaces will be evaluated here. As noted in the foregoing, a review of the relevant literature has found only very sparse use of planar surfaces to create the Coanda Effect [105, 112-114]. Therefore, this investigation has the dual goals of quantitatively demonstrating that the Coanda Effect can be produced by means of plane surfaces and, once demonstrated, the surfaces can be tailored to provide trajectories suitable for the uniform collection of melt-blown fibers.

The model selected for investigation is shown in schematic view in Figure 3.4. This figure is a three-dimensional rendering of the cartoon that was pictured in Figure 3.3. In the rendering, only those features that are relevant to the simulation model are retained. As can be seen in Figure 3.4, the fiber filaments emerge from small circular apertures in the front face of the die. In reality, there are hundreds of such apertures. Only a small number is pictured in the figure because for the others that are situated to the left of those that are shown, symmetry prevails between each successive pairs of apertures. To the right of the displayed apertures, the die face continues as a flat smooth surface. Further inspection of Figure 3.4 shows that the apertures are situated in a slot. This slot is the exit of the channels through which the aforementioned high-velocity air jets emerge from the die face.

The filaments proper are of such small diameter that they have been neglected because the length scale of the Coanda Effect is much greater than the fiber diameter. Consequently, the fiber trajectories will follow the streamlines of the flowing air. This model is used widely and successfully in the simulation of very small particles transported by a carrier gas. The adoption of this model has shifted the focus of the investigation from the fibers per se to the air flow patterns.

The three-dimensional space in which the air flow will be investigated is depicted in Figure 3.4 as jutting forward of the die face. That space will be termed the solution domain. The faces of the solution domain are surfaces on which boundary conditions must be specified. The plane upper boundary of the domain is a surface of geometrical symmetry. That specification eliminates the need to consider an upward reflection of the solution domain. By the same token, the leftmost face of the domain is also a symmetry surface. The rear surface of the domain coincides with the die face and hence is a wall. The other three rectangular faces are open to airflow. In addition to the six rectangular faces, the solution domain includes the parallel-walled channel through which air is delivered.

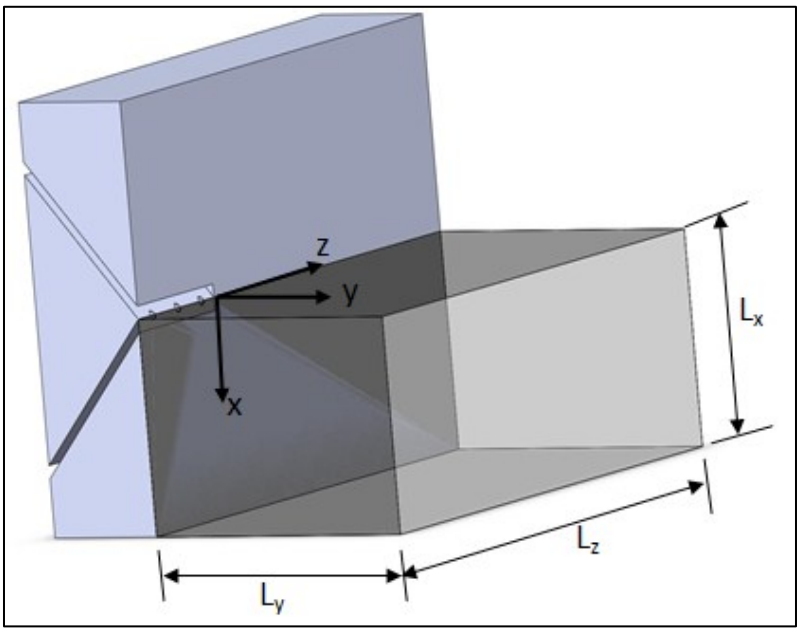

Fig. 3.4: Schematic diagram of the solution domain and the adjacent die face

The strategy for activating the Coanda Effect will now be set forth. A plane wall will be envisioned to be put in place at the right-hand end face of the solution domain, which heretofore had been considered to be open to airflow. The *z*-coordinate defining the distance of the Coanda wall from the location of the emerging air jet (hereafter called the standoff distance) will be varied parametrically as part of the investigation. A second geometrical parameter will be the *y*-direction length of the Coanda-activating surface.

The parameterization will be accomplished in dimensionless terms. The coordinates *x*, *y*, and *z* are made dimensionless according to the following definitions

$$x = \frac{x'}{L_x}, \;\; y = \frac{y'}{L_y}, \;\; z = \frac{z'}{L_z} \tag{3.1}$$

where L_x, L_y, and L_z are shown in Figure 2. This trio of L values will be regarded as constants for all the considered cases. The velocities u, v, and w are also made dimensionless, but with respect to a single reference velocity W_{ref} = 1 ft/s = 0.305 m/s. The numerical simulations were performed for a constant temperature and correspondingly constant values of the density and viscosity of the air flow. These properties were taken at one atmosphere and 25 °C.

To provide definitive information about the parametric variations for which solutions were obtained, it is convenient to define the distance between the origin of coordinates and the z-position of the Coanda wall as C_z'. The investigated values of $C_z = C_z'/L_z$ are 0.25, 0.50, and 1.0. The second geometric parameter that was varied is the y-direction length of the Coanda wall C_y' expressed as $C_y = C_y'/L_y$ = 0.429 and 1.0. Fixed geometrical quantities for the solutions include: (a) width of the air delivery channel = $0.0346L_x$, (b) length of the air delivery channel = $3L_x$, (c) z-direction length of the air slot = $0.15L_x$, and (d) height of the air slot = $0.04L_x$. The choice of these dimensions was guided by those of actual melt-blown-fiber production equipment.

3.3 Governing equations and numerical simulation

The problem under investigation is three-dimensional, and the flow is turbulent. The Reynolds-Averaged Navier- Stokes (RANS) equations that form the basis of the solutions performed here are presented in dimensional terms for ease of recognition.

x-momentum:

$$\rho\left(\frac{\partial u^2}{\partial x}+\frac{\partial uv}{\partial y}+\frac{\partial uw}{\partial z}\right)=-\frac{\partial p}{\partial x}+\frac{\partial}{\partial x}\left[(\mu+\mu_t)\frac{\partial u}{\partial x}\right]+\frac{\partial}{\partial y}\left[(\mu+\mu_t)\frac{\partial u}{\partial y}\right]+\frac{\partial}{\partial z}\left[(\mu+\mu_t)\frac{\partial u}{\partial z}\right] \quad (3.2)$$

y-momentum:

$$\rho\left(\frac{\partial v^2}{\partial y}+\frac{\partial vw}{\partial z}+\frac{\partial vu}{\partial x}\right)=-\frac{\partial p}{\partial y}+\frac{\partial}{\partial y}\left[(\mu+\mu_t)\frac{\partial v}{\partial y}\right]+\frac{\partial}{\partial z}\left[(\mu+\mu_t)\frac{\partial v}{\partial z}\right]+\frac{\partial}{\partial x}\left[(\mu+\mu_t)\frac{\partial v}{\partial x}\right] \quad (3.3)$$

z-momemtum:

$$\rho\left(\frac{\partial w^2}{\partial z}+\frac{\partial wu}{\partial x}+\frac{\partial wv}{\partial y}\right)=-\frac{\partial p}{\partial z}+\frac{\partial}{\partial z}\left[(\mu+\mu_t)\frac{\partial w}{\partial z}\right]+\frac{\partial}{\partial x}\left[(\mu+\mu_t)\frac{\partial w}{\partial x}\right]+\frac{\partial}{\partial y}\left[(\mu+\mu_t)\frac{\partial w}{\partial y}\right] \quad (3.4)$$

In addition, mass conservation has to be satisfied by solving the steady-state and incompressible continuity equation given by

$$\frac{\partial u}{\partial x}+\frac{\partial v}{\partial y}+\frac{\partial w}{\partial z}=0 \quad (3.5)$$

The foregoing equations are in dimensional form, but they were made dimensionless prior to their numerical solution. The quantity μ_t appearing in the RANS equations is called the *turbulent viscosity.* It is assumed to be isotropic, but depends on the coordinates *x, y*, and *z*. The values of μ_t are obtained from turbulence models.

Previous work [115] on a related problem has demonstrated that RANS-based turbulence models are appropriate for the determination of μ_t values that lead to accurate solutions. Here, the Shear Stress Transport model used in conjunction with the RANS equations was chosen because it incorporates the near-wall competence of the k-ω model and the far from wall competence of the k-ε model[101, 116, and117].

Discretization was performed carefully to ensure a mesh of high resolution with nodes concentrated in regions of high gradients. After the execution of a mesh independence study, the final computer runs were performed with a mesh containing about 500,000 nodes. The implementation of the numerical simulations was performed by means of ANSYS-CFX software which is based on finite-volume discretization.

To complete the specification of the problem, boundary conditions are necessary. The boundary condition information is facilitated by reference to Figure 3.4. At the inlet of the air delivery channel, the velocity was specified as $400W_{ref}$. In the paragraph immediately above Figure 3.4, a preliminary discussion of the boundary conditions was set forth. To recapitulate, the upper and leftmost faces that bound the solution domain are symmetry surfaces, while the rear face is a wall. Prior to the placement of the Coanda wall, the other three faces of the solution domain were open to air flow. However, in view of the complexity of the flow, there is no certainty that air crossing these faces is necessarily an outflow. Therefore, to provide total flexibility for the air to find its own directions, these faces are specified as *openings*.

The foregoing situation, absent the Coanda wall, will be termed the *baseline case*. Another noteworthy feature of the baseline case is the selected height of the solution domain. In particular, the lower face of the domain was chosen so that its distance from the upper face (a symmetry plane) did not impose any constraint on the flow field.

The investigation of the Coanda Effect was implemented by the placement of a solid wall as the right-hand face of the solution domain. Two such walls were considered. One of these spanned the entire right-hand face, while the other covered only the inner portion of the right-hand face. For the latter case, the uncovered portion of the right-hand face was specified as an opening. This strategy was motivated in order to assess the impact of the size of the Coanda wall on the flow field.

3.4 Results and discussion for a flat Coanda wall

3.4.1 Coanda effect as witnessed by the transverse velocity

It is proposed that the magnitude of the dimensionless transverse velocity w can serve as a means of identifying the presence of the Coanda Effect. This strategy is based on the notion that the Coanda Effect draws fluid toward the wall whose presence is responsible for the effect.

The approach to the presentation of the *w* results is to select a dimensionless downstream distance *y* (see Figure 3.4) from the jet exit and to display transverse distributions of that velocity on the symmetry plane $x = 0$. This information is presented for parametric values of the dimensionless *standoff distance* of the Coanda wall. The selected dimensionless downstream distances are $y = 0.5$, 1.0, and 1.5, which correspond respectively to Figures 3.5, 3.6, and 3.7.

Each figure contains seven curves. One of these curves is designated as the *baseline* case. It corresponds to a situation where there is no Coanda-inducing wall and for which the solution domain extends laterally (leftward) to a distance of one unit from the air jet exit. This baseline case will be used as a standard against which the magnitudes of the *w*-velocities corresponding to the presence of the Coanda-wall are compared. That wall is parametrically positioned at standoff distances $C_z = 0.25$, 0.5, and 1.0. For each of these Coanda-wall standoffs, the dimensionless downstream lengths of the wall are selected to be 2.0 units (partial length wall) and 3.5 units (full length wall).

Attention will first be focused on Figure 3.5, which corresponds to the downstream distance $y = 0.5$. The horizontal axis shows the dimensionless *z* distance of the Coanda wall from the jet exit. The vertical axis is the dimensionless transverse velocity *w*, positive values of which correspond to flow toward the Coanda wall.

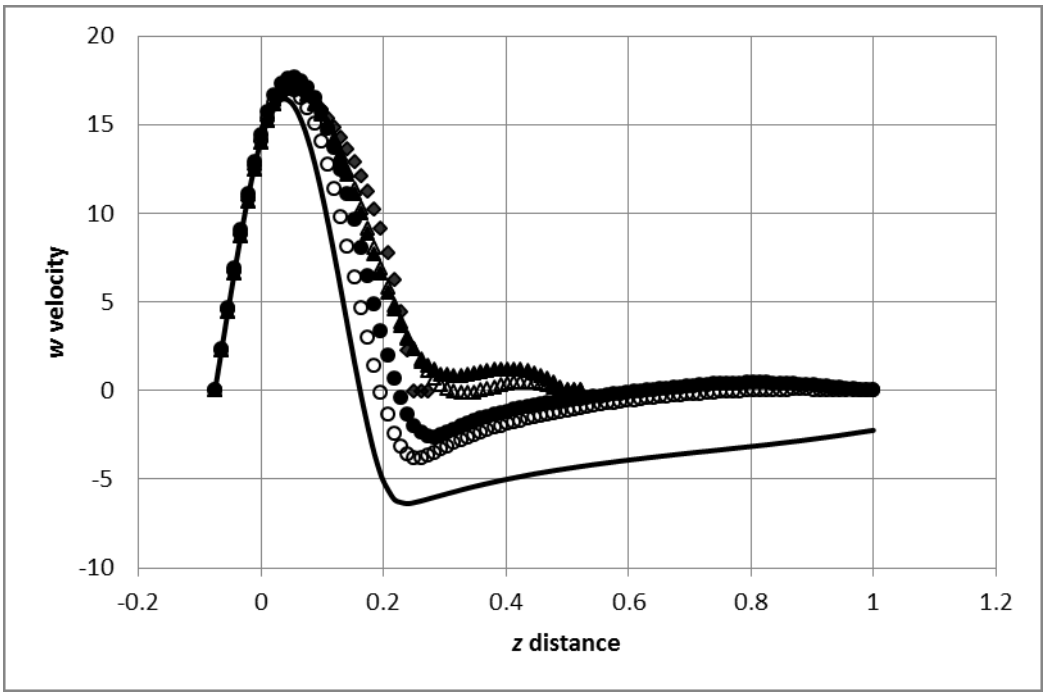

Fig. 3.5: Dimensionless transverse velocity w, in the presence and absence of a Coanda-inducing wall at a dimensionless downstream distance y = 0.5 units. Symbols: — Baseline; ◆◇ 0.25 standoff; ▲△ 0.5 standoff; ● ○ 1.0 standoff. Filled symbols are for the full-length Coanda wall and open symbols are for the partial-length wall.

The interpretation of these results starts with the baseline case and subsequently compares the results for the Coanda walls with it. If the Coanda wall cases show higher magnitudes of the *w*-velocity than those for the baseline case, it can be surmised that the Coanda Effect is operative. Special focus will be directed to the zone of *z* values where the largest *w* velocities occur. That zone can be seen in Fig. 3.5 to be in the neighborhood of $z = 0.05$. This, in itself, is an important finding because it is close to where a fiber would emerge from the die.

Careful inspection of the figure indicates that for this y-distance downstream of the jet exit, none of the investigated standoff distances gives rise to a significant Coanda Effect when viewed with respect to the baseline case. It may be conjectured that this insensitivity is due to the presence of a recirculation zone situated just downstream of the jet exit which shields the small-z neighborhood from the presence of the Coanda wall.

The next figure, Figure 3.6, displays results for a dimensionless downstream distance y = 1.0. Note that only z values up to 0.25 are displayed in the figure. This focus on small z values is motivated by the fact that the air velocity primarily interacts with the fiber in a narrow range of small z. The figure shows a substantial Coanda effect, with the greatest increase of the maximum w velocity being about 38% compared to the baseline case at z of 0.1. This enhancement occurs due to the presence of a Coanda-wall whose standoff distance is 0.25, for both the full- and partial-length walls. It is also seen from Figure 3.6 that the location of the peak w velocity is shifted toward the Coanda wall. This shift appears to be correlated with the magnitude of the velocity maximum: *the greater the magnitude, the greater the shift.* For the case of the highest velocity magnitude, the location of the maximum occurs at z = 0.1.

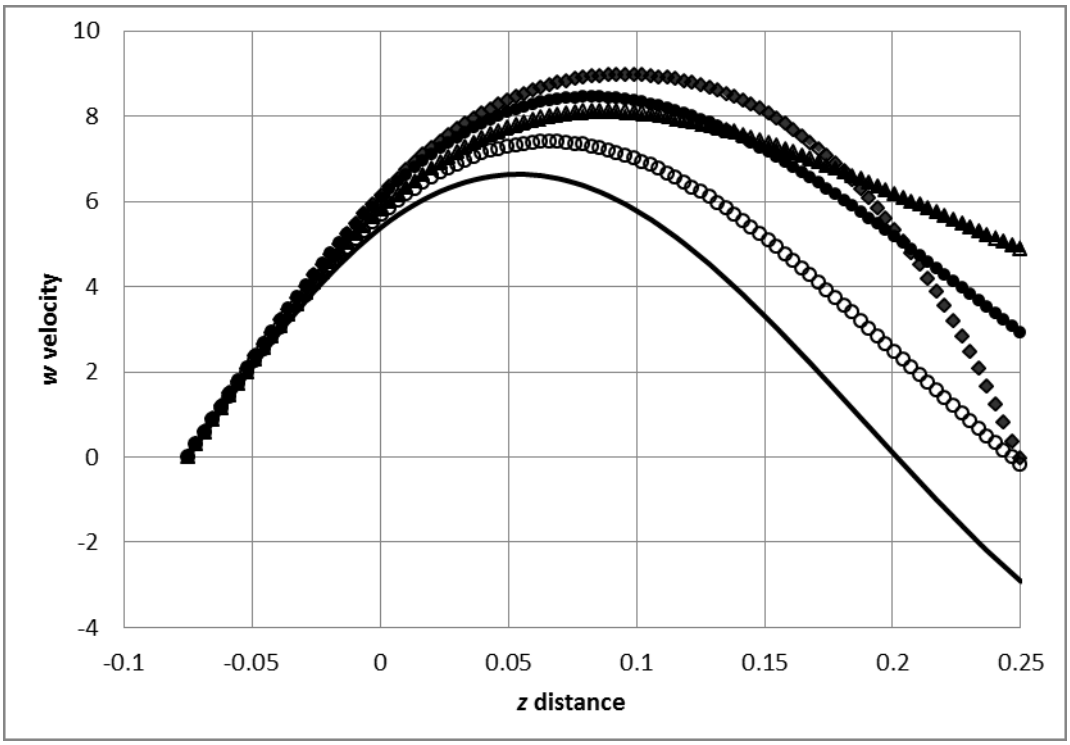

Fig. 3.6: Dimensionless transverse velocity w, in the presence and absence of a Coanda-inducing wall at a dimensionless downstream distance y = 1.0 units. Symbols: — baseline; ◆◇ 0.25 standoff; ▲△ 0.5 standoff; ● ○ 1.0 standoff. Filled symbols are for the full-length Coanda wall and open symbols are for the partial-length wall.

.

The results for the dimensionless downstream distance $y = 1.5$ are presented in Figure 3.7. At this downstream location, the enhancement of the maximum velocity due to the Coanda effect is about 57%. This augmentation occurs for all of the investigated cases except for the partial-length wall at a standoff distance of one. Furthermore, it may be noted that the neighborhood of the greatest enhancement has shifted to z values between 0.1 and 0.15.

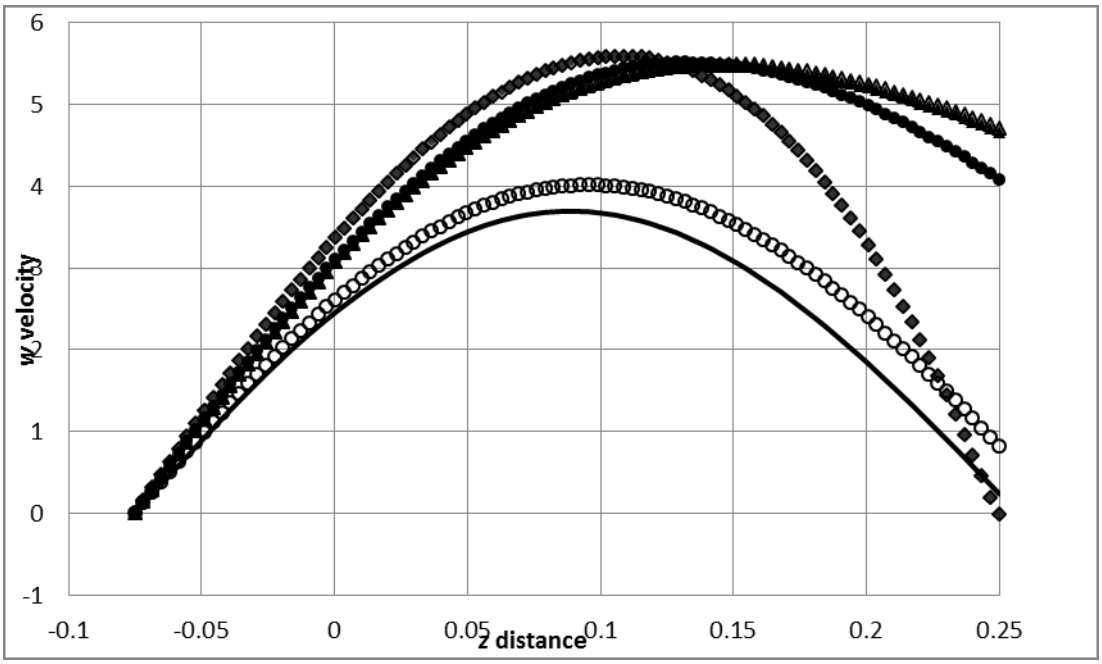

Fig. 3.7: Dimensionless transverse velocity w, in the presence and absence of a Coanda-inducing wall at a dimensionless downstream distance y = 1.5 units. Symbols: — baseline,◆◇ 0.25 standoff;▲△ 0.5 standoff; ● ○ 1.0 standoff. Filled symbols are for the full-length Coanda wall and open symbols are for the partial-length wall.

3.4.2 Streamwise velocity

Focus will now be directed to the response of the streamwise velocity *v* to the presence of the Coanda wall. This information is of lesser importance with respect to the Coanda effect but has relevance with regard to the longitudinal stretching of the fiber. Representative results for the dimensionless *v* velocity are presented in Figure 3.8 which corresponds to the intermediate downstream distance y = 1.0. The figure contains seven curves which are the counterparts of the curves displayed in Figures 3.5-3.7.

The dimensionless vertical velocity *v* is plotted on the ordinate, while the horizontal axis is the transverse coordinate *z*. It can be seen from the figure that the deviations of the Coanda-wall cases from the baseline case occur at larger values of *z*, where the *v* velocity increases. It is believed that this occurrence is due to the action of the Coanda wall to align the flow with its plane. The just-identified trend is also in evidence at the other *y* downstream distances.

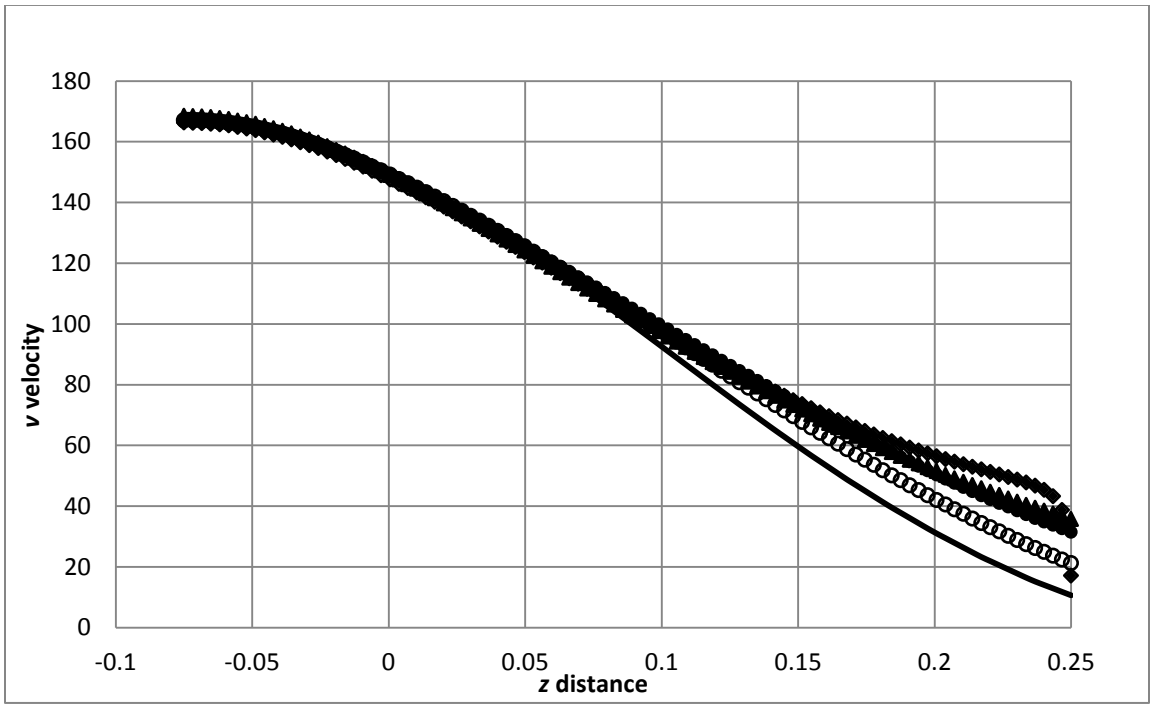

Fig. 3.8: Dimensionless streamwise velocity v, in the presence and absence of a Coanda-inducing wall at a dimensionless downstream distance y = 1.0 units. Symbols: — baseline; ◆ ◇ 0.25 standoff; ▲ △ 0.5 standoff; ● ○ 1.0 standoff. Filled symbols are for the full-length Coanda wall and open symbols are for the partial-length wall.

3.4.3 Vector diagrams

To provide insights into the flow patterns corresponding to various geometrical conditions, normalized vector diagrams are presented in Figures 3.9(a)-(d). The respective parts of the figure are: (a) baseline case, (b) standoff distance of 1.0, (c) standoff distance of 0.5, and (d) standoff distance of 0.25. Careful inspection of these vector diagrams provides convincing proof of the presence of the Coanda effect. For the baseline case where there is no Coanda wall, there is a strong inflow of fluid crossing the plane where the Coanda wall would have been situated. In all the other cases with the Coanda wall in place, there is a clearly evident fluid flow toward the wall even though it is a blockage. This reversal of flow direction can only be ascribed to the Coanda effect. Note that normalized vectors have been used to highlight the direction of the flow and not the magnitude. Hence, some vectors which appear to be crossing a wall indicate a flow direction towards the wall but the fluid does not cross the wall.

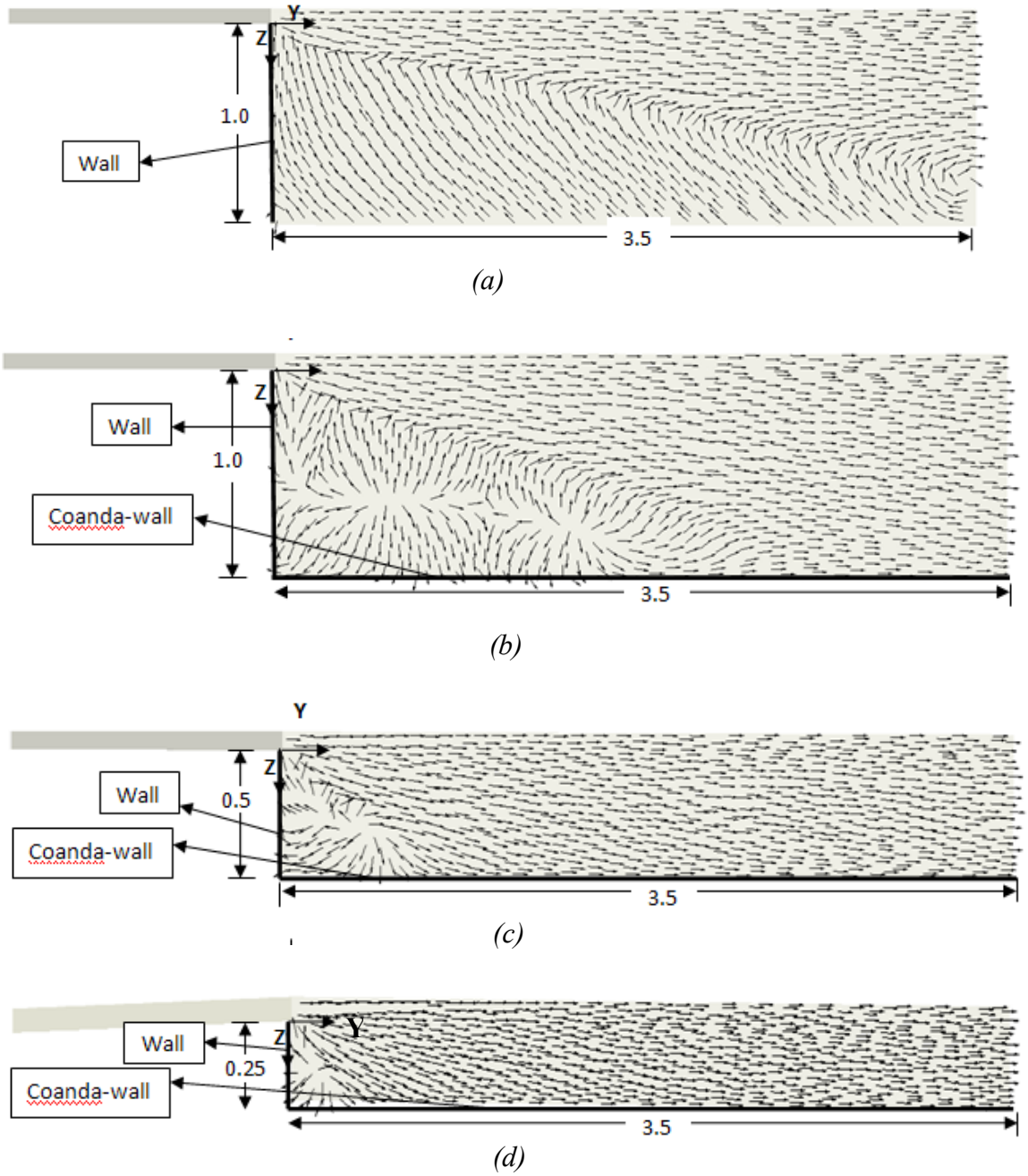

Fig. 3.9: Normalized vector diagrams on the symmetry plane x = 0 for plane wall configurations. (a) Baseline case; (b) 1.0 Standoff distance; (c) 0.5 Standoff distance; and (d) 0.25 Standoff distance

3.5 Simulations and results for a curved Coanda wall

In commonly encountered depictions of the Coanda Effect, a curved wall is exhibited. In fact, investigations of curved Coanda-wall effects are very much more common than are studies involving flat Coanda walls. It is relevant to qualitatively examine the behavior of the flow in the presence of a curved Coanda wall that occupies the same geometric position as the flat Coanda wall that was the focus of the foregoing presentation.

Figures 3.10 (a) and (b) illustrate the adopted curved wall configurations. The (a) part of the figure shows a lesser incised wall, the narrow waist of which is 0.5 units from the jet exit. On the other hand, the configuration shown in the part (b) diagram displays a narrower waist which is 0.25 units from the jet exit. The curvatures of both (a) and (b) are sections of an ellipse. In both cases, the downstream length of the Coanda wall is defined by the end of the curved section. Beyond the end of that section, the straight segment delineates the boundary of the solution domain which is regarded as an opening.

Figures 3.10 (a) and (b) also display normalized velocity vectors. The directions indicated by these vectors clearly indicate the presence of the Coanda wall, as did those in Figures 3.9 (b)-(d). Inspection of Figures 3.10 (a) and (b) suggests that the Coanda Effect is operative from the leading edge of the curved wall to the narrow waist of the wall. Another feature evident in Figure 3.10 (b) is the inability of the flow to follow the sharp

curvature at the downstream end of the Coanda wall. This inability might be undesirable in certain applications.

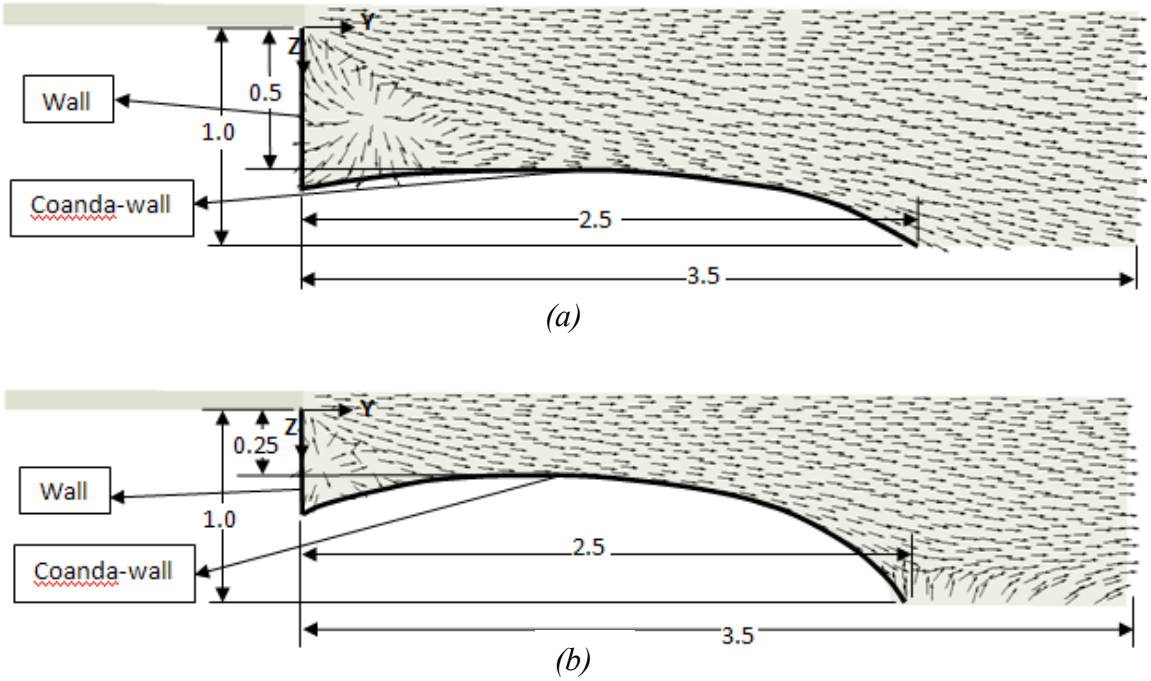

Fig. 3.10: Normalized vector diagrams of curved wall cases. (a) lesser incised wall; (b) deeply Incised wall.

3.5.1 Coanda effect as witnessed by the transverse velocity

Figures 3.11 and 3.12 have been prepared to compare the capabilities of curved and flat walls to induce the Coanda Effect. These figures have the same format as that used in Figures 3.5-3.7. Figure 3.11 displays the transverse velocity w as a function of the distance z which defines locations between the jet exit and the Coanda wall. This figure corresponds to a downstream distance $y = 0.5$ and to the symmetry plane $x = 0$. There are two curves in the figure for the contoured wall, respectively for the lesser (Figure 3.10(a))

and greater incisions (Figure 3.10(b)). The flat-wall case is represented by 0.25 and 0.5 standoffs, both partial walls.

Overall, there appears to be little difference between the flat- and curved-wall cases. This finding adds strong support to the notion that plane walls can effectively serve as Coanda-inducing surfaces.

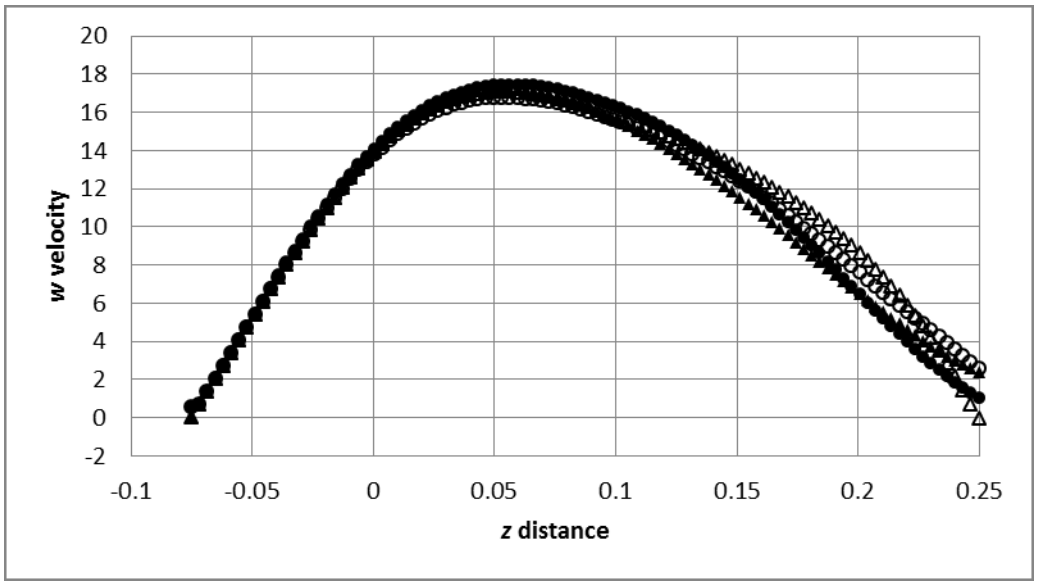

Fig. 3.11: Comparison of Coanda effects induced by curved and straight walls at a downstream distance y = 0.5. Symbols: ● Lesser incised curved wall; ○ Deeply incised curved wall; ▲ 0.5 Standoff flat wall (partial length); △ 0.25 Standoff flat wall (partial length)

Figure 3.12 presents a similar comparison at a downstream distance $y = 1.0$. It can be seen from the figure that best performance (largest w velocity magnitude) can be achieved equally well by either a flat or a curved wall. However, to achieve this equal

performance, the flat wall has to be positioned at a smaller standoff (0.25) than does the curved wall (0.5).

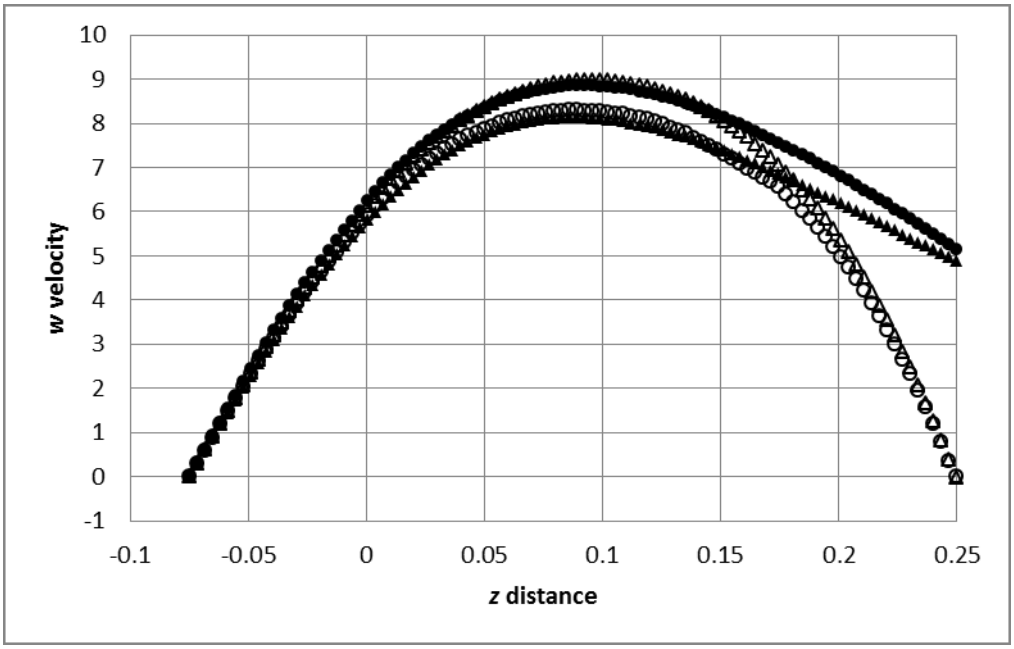

Fig. 3.12: Comparison of Coanda effects induced by curved and straight walls at a downstream distance y = 1.0. Symbols: ● *Lesser incised curved wall;* ○ *Deeply incised curved wall;* ▲ *0.5 Standoff flat wall (partial length);* △ *0.25 Standoff flat wall (partial length)*

Chapter 4

SUCTION CATHETERS FOR EXTRACTING SPENT CONTRAST MEDIA TO AVOID NEPHROPATHY

4.1 Introduction

The primary motivation of this chapter is to develop and implement numerical simulation models to analyze the flow characteristics of suction catheters for the extraction of iodinated contrast media from the human circulatory system. The goal is to develop a generalized model which can be used to evaluate suction catheter designs and also to obtain the relationship between pressure drop and flow rate.

Fluoroscopic contrast media is often introduced into the blood stream for visualization of the arteries and veins for diagnostic purposes and to aid the placement of medical devices. For a normal healthy individual, the introduction of iodinated-contrast media is a harmless event as the contrast medium is filtered out by the kidneys. However, for individuals with certain pre-existing conditions, the introduction of iodinated-contrast media causes irreparable damage to the kidneys, leading to a condition known as Contrast-Induced-Nephropathy (CIN). Despite its inherent risk to these individuals, the use of iodinated-contrast-media is often unavoidable and, in such cases, it is a necessary to prevent this medium from entering the kidneys to reduce the risk of CIN. One method

of preventing the contrast-medium-laden blood from reaching the kidneys is to use a suction catheter to drain the blood from the body as described in Chapter 1.

This method envisions the use of a suction catheter placed in the coronary sinus to drain the contrast-laden blood from the body. Depending on the volume of blood removed, it may either be discarded or filtered and then returned to the body through the femoral arteries. The coronary sinus has been chosen as the location for the suction catheter because it collects deoxygenated blood from all the major coronary arteries before draining it into the right atrium. The coronary sinus contributes about 90% of the volume of blood flowing into the right atrium. Figure 4.1 shows an image of the coronary sinus and its major tributaries.

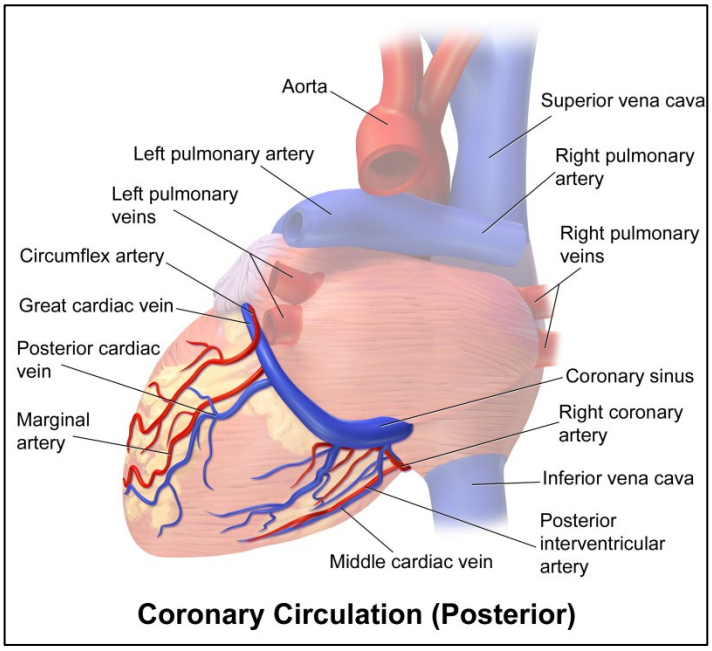

Fig. 4.1: Posterior image of the coronary sinus and its tributaries

The Great Cardiac Vein (GCV) enlarges into the coronary sinus and contributes about 60 -70% of the flow into the coronary sinus. The other notable tributaries are the middle cardiac vein (MCV) and posterior cardiac vein (PCV). The size and shape of these blood vessels varies greatly between individuals.

The first section of this chapter deals with establishing the flow characteristics occurring in the coronary sinus. In that section, a simplified general representation of the coronary sinus as a circular tube is used, and the generated results are utilized for simulating the operation of a suction catheter placed in the coronary sinus. The second section is focused on analyzing the flow occurring in a suction catheter placed in the coronary sinus. The main result of interest would be to obtain the flow rate in the catheter versus pressure drop across the length of the catheter. The final section explores modifications to the catheter inlet design by including side holes and slots in the catheter wall to enhance the flow rates occurring in the catheter. It also aims at quantifying the effects of some three-dimensional factors such as the contribution of tributaries to the coronary sinus flow and the effects of misalignment of the catheter flow rate.

4.2 Characterization of flow in the coronary sinus

The blood flow characteristics of the coronary sinus are of great interest to cardiologists as it is an indicator of the health of the heart and the circulatory system. Various experimental methods for measuring the volume of blood flow in the coronary sinus have been developed and reviewed widely in literature [118-121]. These methods describe

means of obtaining both time averaged [27,122] and instantaneous [123] volumetric flow rates or velocities. The measurements of flow rates at the coronary sinus are used to provide an estimate of the cardiac reserve of an individual.

The catherization of the coronary sinus is a commonly used medical interventional method for various applications such as delivering contrast media, inducing cardioplegia and balloon occlusion. All these applications generally involve the delivery of fluid or the occlusion of fluid flow, but the present application explores the removal of fluid from the coronary sinus. The removal of fluid is to be performed by means of a suction catheter which is to be connected to a pump, thereby creating a pressure-driven flow. To model the operation of the suction catheter, it is necessary to know the pressure in the coronary sinus which would be used as a boundary condition for the suction catheter simulation. This section of the chapter is focused on obtaining a general and reliable pressure boundary condition which can be used for modeling a suction catheter placed in the coronary sinus.

4.2.1 Steady flow volume and pressure in coronary sinus

4.2.1a Problem definition

Although the pressure in the coronary sinus is time-dependent due the pulsatile nature of the flow, considerable useful diagnostic information can be obtained relatively quickly by using time-averaged values. In the coronary sinus, averaged flow rates of 122 +/- 25 ml/min are widely reported in literature [27]. Depending on the measurement methods

used, some papers report flow rates as high as 160 ml/min[123]. To determine the pressure at the entrance of the coronary sinus, a simple numerical model was devised. It is based on the coronary sinus represented as a circular tube. The coronary sinus is a fairly large vessel with a diameter of 7 +/- 5 mm, and a length which varies widely between individuals in the range of 15 to 65 mm. The coronary sinus drains into the right atrium in which the pressure is close to the central venous pressure which ranges between 5 – 10 mmHg. Figure 4.2 shows the simplified model which was used to obtain the pressure in the coronary sinus.

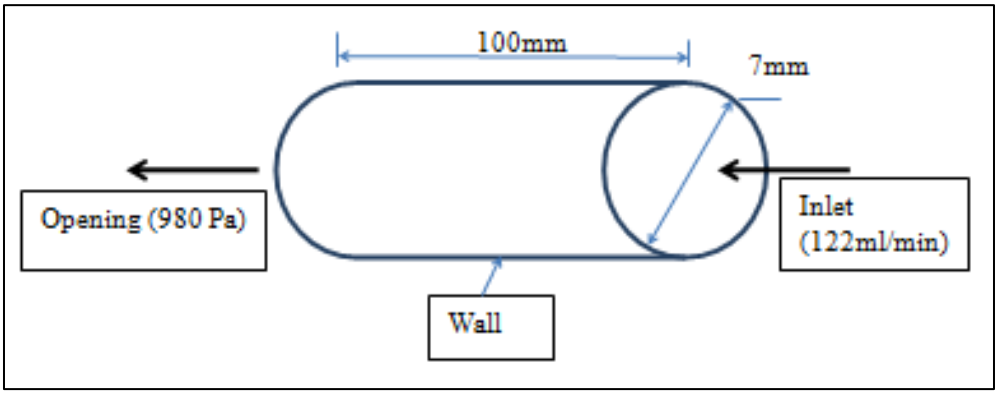

Fig.4.2: Numerical model used to obtain pressure in the coronary sinus

It can be seen from Figure 4.2 that the length of the coronary sinus has been extended to 100 mm to allow the flow to fully develop. A fixed flow rate of 122ml/min was applied at the inlet, and the other end was specified to be an opening at the right atrial pressure of 980 Pa. The diameter of the coronary sinus was taken to be 7 mm and the walls were assumed to be rigid. It has been reports that coronary arteries do not show significant dilation at low pressures [124].

4.2.1b Governing equations and constitutive models

The governing equations to be solved for the fluid flow are the steady-state, incompressible form of Navier-Stokes Equations (Eq. 4.1-4.3) which are the equations of Netwon's Second Law applied to a flowing fluid in conjunction with the continuity equation (Eq. 4.4) which is the mass conservation equation. Both Newtonian and non-Newtonian models for the viscosity of blood are to be considered.

Navier-Stokes Equations:

x-momentum:

$$\rho\left(\frac{\partial u^2}{\partial x}+\frac{\partial uv}{\partial y}+\frac{\partial uw}{\partial z}\right)=-\frac{\partial p}{\partial x}+\frac{\partial}{\partial x}\left[(\mu)\frac{\partial u}{\partial x}\right]+\frac{\partial}{\partial y}\left[(\mu)\frac{\partial u}{\partial y}\right]+\frac{\partial}{\partial z}\left[(\mu)\frac{\partial u}{\partial z}\right] \quad (4.1)$$

y-momentum:

$$\rho\left(\frac{\partial v^2}{\partial y}+\frac{\partial vw}{\partial z}+\frac{\partial vu}{\partial x}\right)=-\frac{\partial p}{\partial y}+\frac{\partial}{\partial y}\left[(\mu)\frac{\partial v}{\partial y}\right]+\frac{\partial}{\partial z}\left[(\mu)\frac{\partial v}{\partial z}\right]+\frac{\partial}{\partial x}\left[(\mu)\frac{\partial v}{\partial x}\right] \quad (4.2)$$

z-momemtum:

$$\rho\left(\frac{\partial w^2}{\partial z}+\frac{\partial wu}{\partial x}+\frac{\partial wv}{\partial y}\right)=-\frac{\partial p}{\partial z}+\frac{\partial}{\partial z}\left[(\mu)\frac{\partial w}{\partial z}\right]+\frac{\partial}{\partial x}\left[(\mu)\frac{\partial w}{\partial x}\right]+\frac{\partial}{\partial y}\left[(\mu)\frac{\partial w}{\partial y}\right] \quad (4.3)$$

Continuity Equation:

$$\frac{\partial u}{\partial x}+\frac{\partial v}{\partial y}+\frac{\partial w}{\partial z}=0 \quad (4.4)$$

The quantities u, v, and w are the respective velocity components in the x, y, and z directions; ρ is the density, p is the pressure, and μ is the viscosity. Note that the viscosity is contained within the differentiation operators to accommodate the spatial variations of the non-Newtonian model. For the Newtonian model, the viscosity is regarded as a constant so that it passes through these operators. A widely used blood viscosity of

0.0035 Pa.s was used for the Newtonian model. For the non-Newtonian case, both the Carreau and Power Law models introduced in Chapter 2 were used. The boundary conditions used to close the model have been indicated in Figure 4.2. The governing equations were discretized by the finite volume method and solved by means of ANSYS CFX software which is a commercially available CFD software package.

4.2.1c Results for steady flow simulations

The most relevant result of the simulation is the pressure drop occurring across the length of the modeled coronary sinus. This finding provides the inlet pressure to be applied as a boundary condition in subsequent simulations which would include the presence of a suction catheter.

Using a Newtonian model, the pressure drop across the length of the tube was found to be around 15 Pa. Based on the Reynolds number of around 100 in the artery, the flow is laminar. Figure 4.3(a) shows the pressure variation at the center line of the artery, and Figure 4.3(b) shows the wall shear stress as predicted by different blood constitutive models. The obtained pressure drop from the inlet (x = 0.1 m) to outlet (x = 0) is very close to the value predicted by the Poisueille's equation for fully developed laminar flow in a pipe.

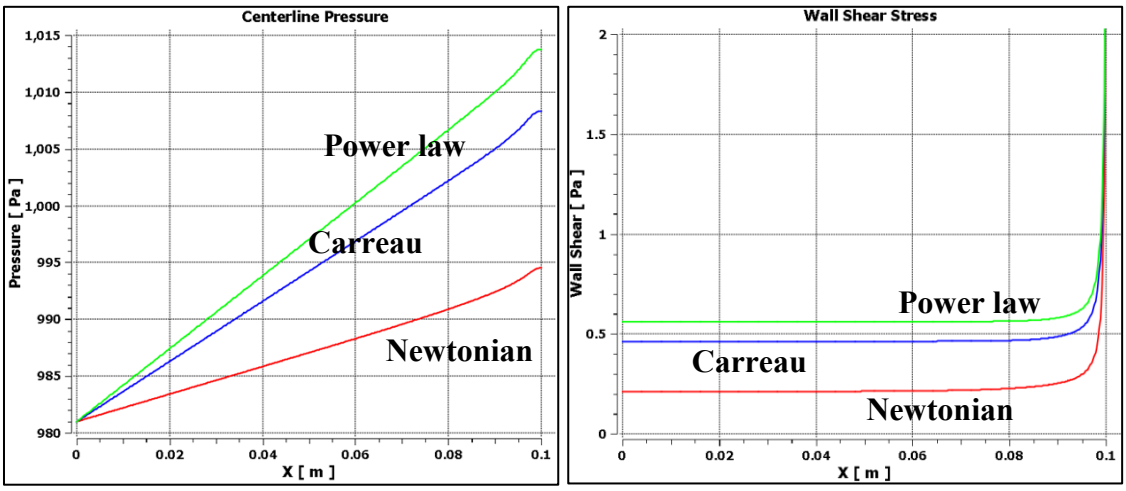

(a) *(b)*

Fig. 4.3: (a) Pressure at the center line of the coronary sinus; (b) Wall shear stress

It can be noted from Figure 4.3 that the Newtonian approximation underestimates both the pressure drop and wall shear stress. This is due to the fact that at the investigated conditions, the viscosity corresponding to the non-Newtonian models is higher than the Newtonian viscosity used. Since blood is a shear-thinning fluid, its apparent viscosity would reduce and approach the Newtonian viscosity at higher shear strain rates. Also, the difference in pressure drop predicted by different models is relatively small compared to the variability in the flow measurement inputs and overall pressure drop likely to be encountered during the use of a suction catheter. The shear stress levels are also low when compared to the levels required to cause hemolysis. For the sake of numerical efficiency, the Newtonian viscosity model was employed for further analysis.

4.2.2 Transient pulsatile flow in coronary sinus

4.2.2a Problem definition

The preceding section dealt with modeling the blood flow in the coronary sinus as steady. However, it is well known that the flow is transient and pulsatile in nature according to the cardiac rhythm. This section deals with modeling the pulsatile nature of the flow. The numerical model is similar to the one depicted in Figure 4.2, the only difference being that the steady flow inlet boundary condition is replaced by a time-dependent velocity. As an initial condition, the fluid was taken to be at rest throughout the solution domain. Rossum et al. have measured the instantaneous blood velocity in a human coronary sinus using MRI methods [123]. The velocity in the coronary sinus as a function of time is shown in Figure 4.4.

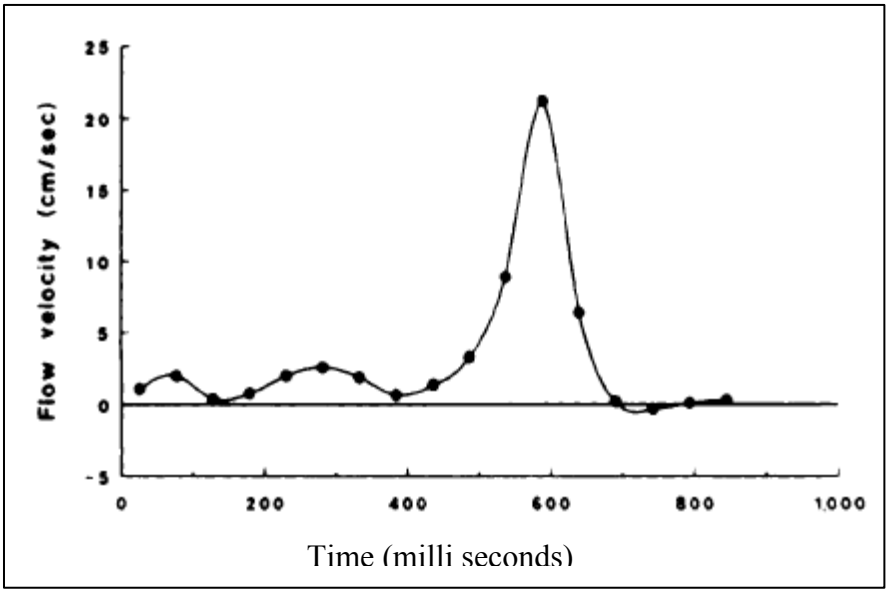

Fig. 4.4 [123]: The velocity in the human coronary sinus as a function of time

It can be seen from Figure 4.4 that the velocity is highly variable and includes one sharp peak corresponding to the early diastole and another small peak just before the sharp peak corresponding to the systole. It can also be seen that flow is reversed for a small portion of the cycle. Similar to the steady flow results, there is large variation in the flow measurement results between various individuals, measurement methods, and other physiological factors. The above velocity wave form has been used as input to solve for the corresponding inlet pressure variation as a function of time.

4.2.2b Governing equations

Once again, the governing equations to be solved are the Navier-Stokes and Continuity equations similar to those listed in section 4.1.2b. The only difference being that the unsteady terms can no longer be dropped. Also, the pulsatile nature of the flow can cause transition from laminar flow to turbulent flow and back. Therefore, the possibility of turbulence needs to be accounted for. Hence, a modified form of the Navier-Stokes Equations called the Reynolds-Averaged Navier Stokes Equations (RANS) are used to account for turbulence.

RANS Equations:

x-momentum:

$$\rho\left(\frac{\partial u}{\partial t}+\frac{\partial u^2}{\partial x}+\frac{\partial uv}{\partial y}+\frac{\partial uw}{\partial z}\right)=-\frac{\partial p}{\partial x}+\frac{\partial}{\partial x}\left[(\mu+\mu_t)\frac{\partial u}{\partial x}\right]+\frac{\partial}{\partial y}\left[(\mu+\mu_t)\frac{\partial u}{\partial y}\right]+\frac{\partial}{\partial z}\left[(\mu+\mu_t)\frac{\partial u}{\partial z}\right] \quad (4.5)$$

y-momentum:

$$\rho\left(\frac{\partial v}{\partial t}+\frac{\partial v^2}{\partial y}+\frac{\partial vw}{\partial z}+\frac{\partial vu}{\partial x}\right)=-\frac{\partial p}{\partial y}+\frac{\partial}{\partial y}\left[(\mu+\mu_t)\frac{\partial v}{\partial y}\right]+\frac{\partial}{\partial z}\left[(\mu+\mu_t)\frac{\partial v}{\partial z}\right]+$$

$$\frac{\partial}{\partial x}\left[(\mu+\mu_t)\frac{\partial v}{\partial x}\right] \tag{4.6}$$

z-momemtum:

$$\rho\left(\frac{\partial w}{\partial t}+\frac{\partial w^2}{\partial z}+\frac{\partial wu}{\partial x}+\frac{\partial wv}{\partial y}\right)=-\frac{\partial p}{\partial z}+\frac{\partial}{\partial z}\left[(\mu+\mu_t)\frac{\partial w}{\partial z}\right]+\frac{\partial}{\partial x}\left[(\mu+\mu_t)\frac{\partial w}{\partial x}\right]+$$

$$\frac{\partial}{\partial y}\left[(\mu+\mu_t)\frac{\partial w}{\partial y}\right] \tag{4.7}$$

Incompressible continuity equation:

$$\frac{\partial u}{\partial x}+\frac{\partial v}{\partial y}+\frac{\partial w}{\partial z}=0 \tag{4.8}$$

The quantity μ_t appearing in the RANS equations is called the turbulent viscosity. It is assumed to be isotropic, but can depend on the coordinates x, y, and z. The values of μ_t are obtained from turbulence models. The SST model [117-119] developed by Menter et al. has been specifically chosen to solve for turbulence because of its ability to be tuned to model transition between laminar and turbulent flows. Menter et al. have tuned the coefficients of turbulent kinetic energy production and dissipation in the SST model to be able to model transition between laminar and turbulent flow for external flows. Lovik et al. have tuned those constants to model transitional flows for pulsatile internal flows [46,47]. Here, the model used by Lovik et al. is employed to model the turbulent viscosity.

4.2.2c Results for transient flow simulations

The transient pressure profile corresponding to the inlet velocity wave form in Figure 4.4 is obtained from a 2-D axisymmetric numerical simulation and displayed in Figure 4.5. To let the periodic flow establish itself, the simulation was performed for three cardiac cycles. The figure also shows a comparison between the results obtained from the transitional-turbulence model and the laminar model. The comparison is made between the pressure at the inlet cross section, since it is the desired output of the simulation.

It can be seen from Figure 4.5 that both those models predict very similar results. This is most likely due to the fact that even at the peaks, the Reynolds numbers are so low that laminar flow prevails. This particular result demonstrates the ability of the transitional model to reduce into a laminar model at low Reynolds numbers.

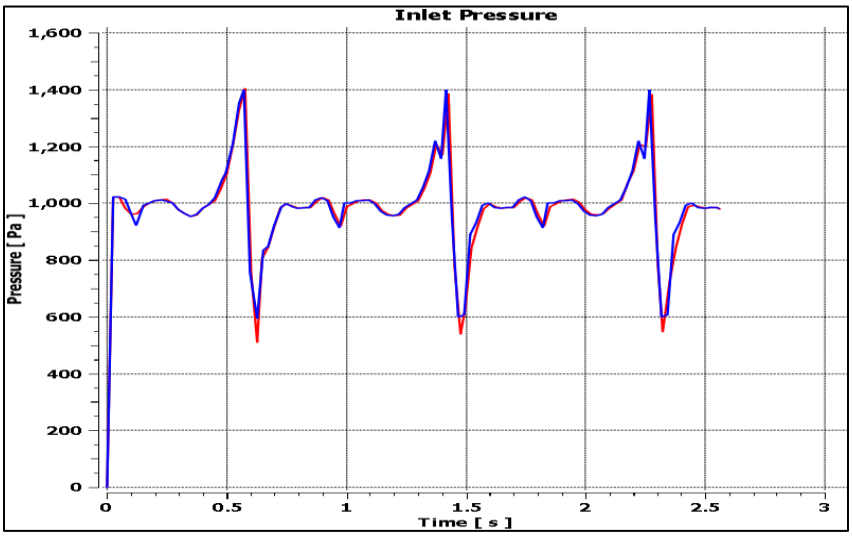

Fig. 4.5: Transient inlet pressure corresponding to inlet velocity in Figure 4.4

Furthermore, the average inlet pressure from Figure 4.5 over one second is found to be around 1002 Pa. For comparison, from a steady-state simulation based on an averaged flow rate from Figure 4.4, the inlet pressure was found to be around 1000Pa. This agreement between the two results lends credence to the ignoring of flow pulsations in certain applications where the duration of interest is much longer than one time period of pulsation. Limiting values of shear stress level and other variables can obtained from steady-state solutions of the peaks of the pulse.

4.3 Flow Analysis of a suction catheter placed in the coronary sinus

The preceding section was aimed at characterizing the flow in the coronary sinus in order to enable the simulation of the operation of a suction catheter. One of the main results of interest would be the relationship between the suction pressure and the rate of fluid extraction through the catheter. In order to obtain these results, an axisymmetric numerical model similar to the one shown in Figure 4.2 is constructed and shown in Figure 4.6.

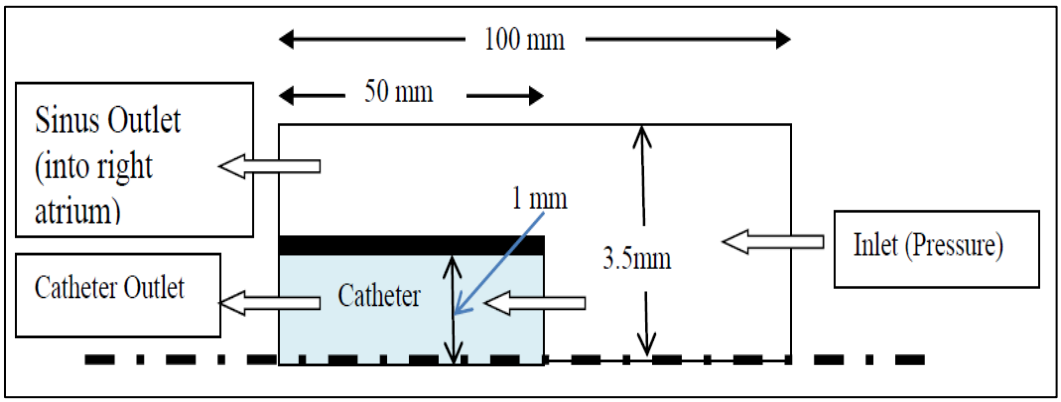

Fig. 4.6: Model of a suction catheter placed in the coronary sinus

The coronary sinus is modeled as a straight circular tube of 7-mm internal diameter. A catheter with a central lumen of 2mm is placed along the axis of the coronary sinus midway along the modeled length of the coronary sinus. The wall thickness of the catheter was varied between 0.25 and 0.50 mm. The pressure boundary conditions to be respectively applied at the inlet and outlet of the coronary sinus were determined in the preceding section. For two separate cases, a fixed steady pressure and a timewise periodic pressure shown in Figure 4.5 were applied at inlet of the coronary sinus. For the latter transient case, all the velocity components of the fluid in the solution domain were set to zero as initial condition. The catheter outlet pressure was varied parametrically and the corresponding flow rate was obtained. The governing equations were the same as those employed in preceding section, and a Newtonian constitutive model for the viscosity of blood was used.

4.3.1 Steady flow results for a suction catheter operating in the coronary sinus

Figure 4.7 shows the relationship between the catheter suction pressures at the modeled outlet of the catheter and the volumetric flow extraction rate through the catheter with wall thicknesses of 025 and 0.5 mm. For both the cases, the catheter lumen diameter was 2mm.

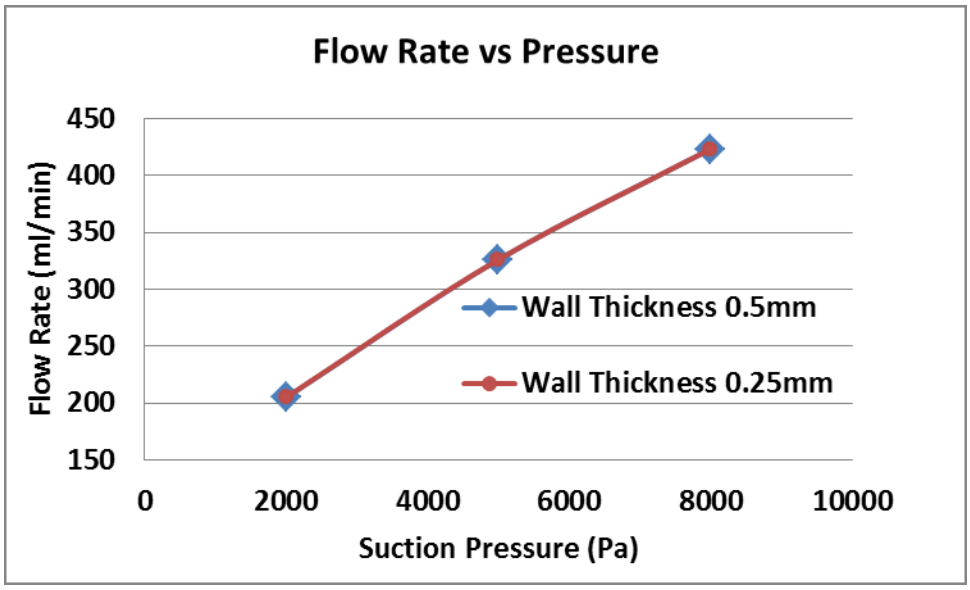

Fig. 4.7: Extraction flow Rate versus catheter outlet pressure

Typical desired flow extraction rates are in the range of 200 to 400 ml/min. Figure 4.7 shows the suction pressures required at the outlet of the modeled catheter section with a given sinus inlet pressure (~1000Pa) to obtain these flow rates. Note that the suction pressures shown in Figure 4.7 are the suction pressures that need to be applied to the catheter near the end of the coronary sinus. Note that the total pressure drop which needs to be overcome by the pump would be much higher than the pressure drop obtained by

subtracting the modeled catheter outlet pressure and the coronary sinus inlet pressure. This is due to the fact that only a small length of the catheter has been included in the modeled. It can also been seen from Figure 4.7 that the catheter wall thickness does not have an impact on the flow rate through the catheter in the investigated ranges.

Figure 4.8 shows the ratio of the flow rate in the catheter to the flow rate entering the coronary sinus. For the effective removal of the contrast media, it is desired that most of the flow entering the coronary sinus should exit through the suction catheter and must not escape into the right atrium through the space between the catheter wall and the sinus wall. When the flow ratio shown in Figure 4.8 is less than unity, it indicates that there is some flow escaping through the space between the catheter and the sinus wall. At higher suction pressures, the ratio becomes greater than unity indicating that flow is being sucked back into the catheter from the right atrium. This is a significant finding as it shows that the need for a complex flow- occluding balloon can be eliminated when the proper suction pressure is applied. In reality, the extent of this backflow is limited by the presence of the Thebesian valve. Applying excessive suction pressures would lead to greater strain on the valve.

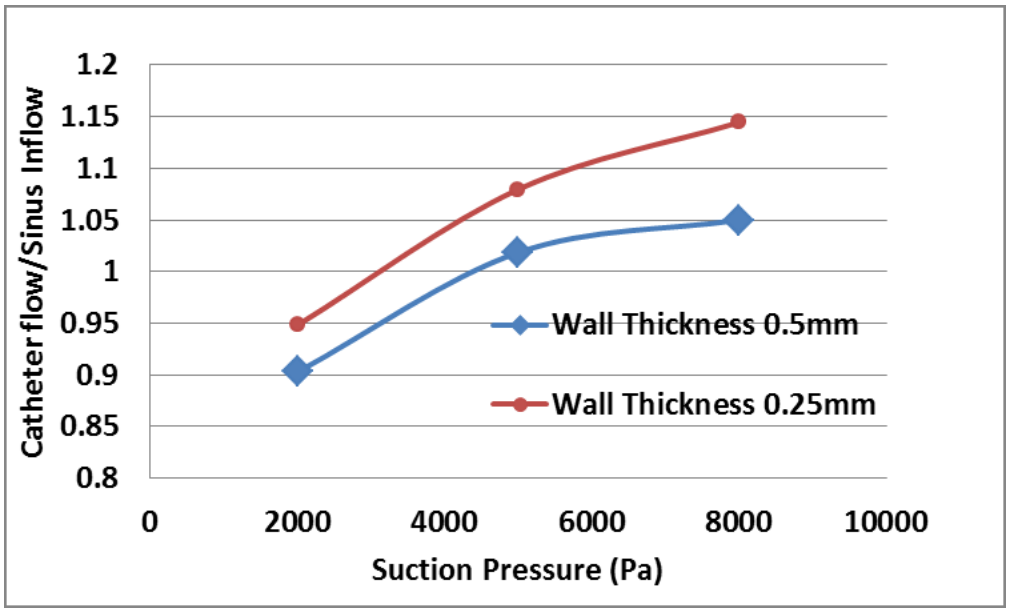

Fig. 4.8: Ratio of catheter flow rate to coronary sinus inflow

Though the catheter wall thickness does not have an impact on the overall flow rate through the catheter, it can be clearly seen from Figure 4.8 that it influences the amount of amount of flow through the annular space between the catheter wall and the artery wall. Surprisingly, it shows that the catheter with the thicker wall corresponds to more flow through the annular space, despite having reduced annular area. This result can be explained with the aid of velocity vector diagrams of the flow entering the suction catheters depicted in Figure 4.9.

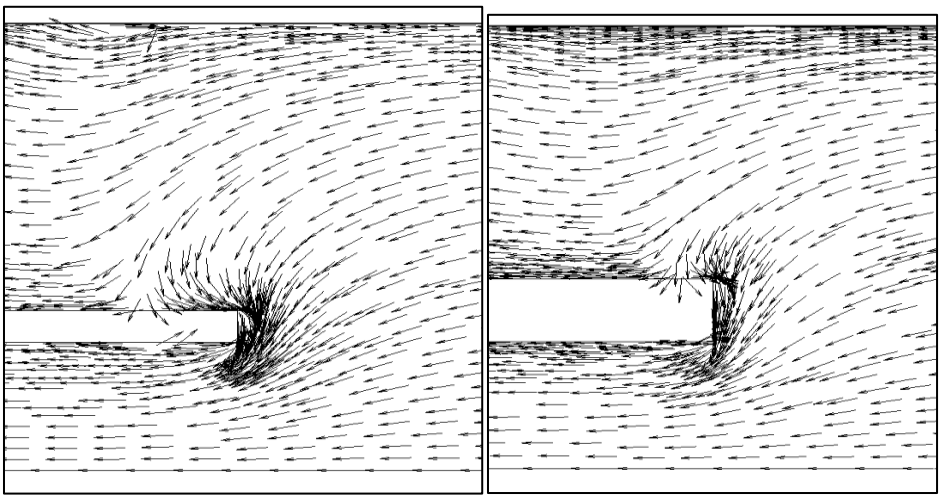

(a) *(b)*

Fig. 4.9: Normalized velocity vectors showing flow entering the suction catheter at 2000 Pa outlet pressure (a) catheter with thin wall (0.25mm) (b) Cathteter with thick wall (0.5mm)

It can be seen from the vector diagrams that the flow entering the suction catheter from near the artery wall would face greater resistance from the thicker wall due to increased wall length in the vertical direction which would lead to relatively lesser amount of flow getting into the catheter.

Figure 4.10 shows the shear stress contours of the fluid in the domain, and Figure 4.11 shows the relationship between shear stress level and suction pressure. It can be seen that there is a very localized zone of high shear stress near the entrance of the catheter. The magnitude of shear stress is still relatively low in terms of potential to induce hemolysis. Blood would need to be exposed to this order of magnitude of shear stress for at least a

few hundred seconds to induce hemolysis. It can be seen that the maximum shear stress increases with suction pressure and that the wall thickness has an impact on the value of the localized maximum shear stress.

The shear stress in this localized region can be significantly reduced by rounding the catheter wall tip.

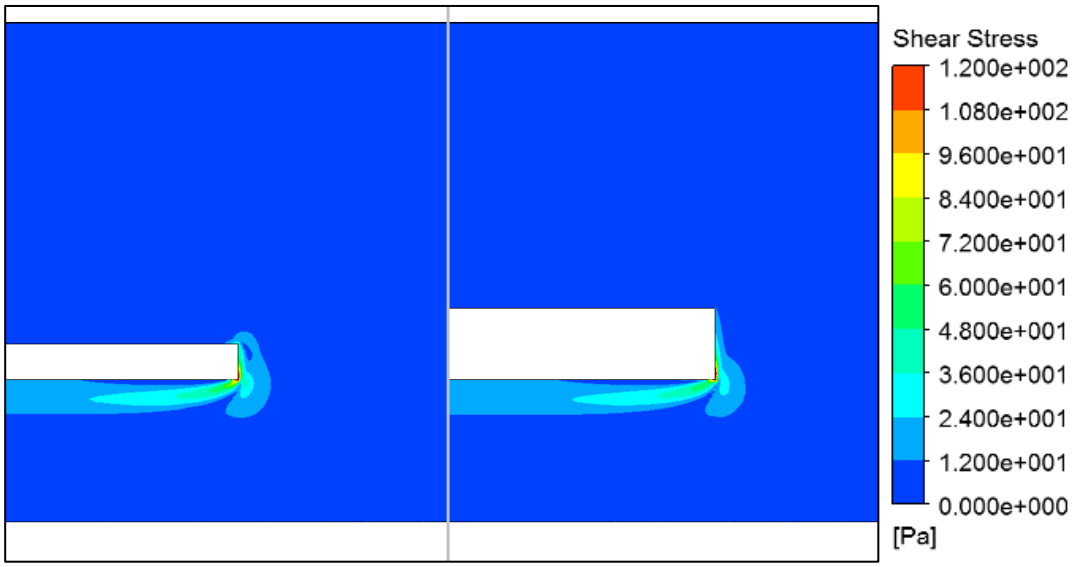

(a) *(b)*

Fig. 4.10 Shear stress contours of flow entering the suction catheter at 2000 Pa catheter outlet pressure (a) catheter with thin wall (0.25mm) (b) Cathteter with thick wall (0.5mm)

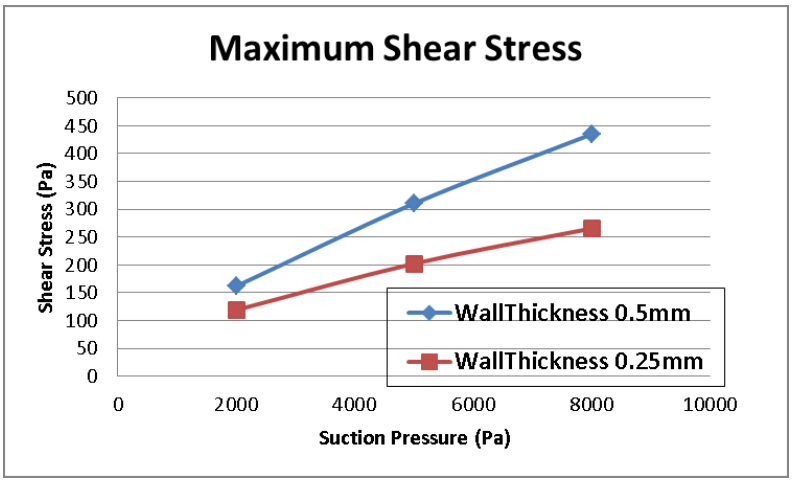

Fig. 4.11: Maximum shear stress in flowing blood at location shown in Fig. 4.10 as a function of suction pressure

4.3.2 Transient Flow in a suction catheter placed in the Coronary Sinus

To account for the pulsating nature of the flow, the computed transient pressure profile in Figure 4.5 was applied as a boundary condition at the entrance of the coronary sinus and a fixed suction pressure of 2000 Pa was imposed at the exit of the catheter. Figure 4.12 shows the transient flow variations at the inlet of the coronary sinus and in the suction catheter. It can be clearly seen that the effect of the pulsation has damped out in the catheter and a constant flow rate of about 200ml/min prevails. This value agrees extremely well with the flow rate obtained from the steady state solution in the preceding section which also predicted a flow rate of about 200ml/min in the catheter at a suction pressure of 2000 Pa. This result shows that the effect of flow pulsations can be neglected while simulating the flow in a suction catheter. Peak limiting values of parameters such as the wall shear stress can be obtained by getting a steady state solution at corresponding to the peaks in the boundary conditions.

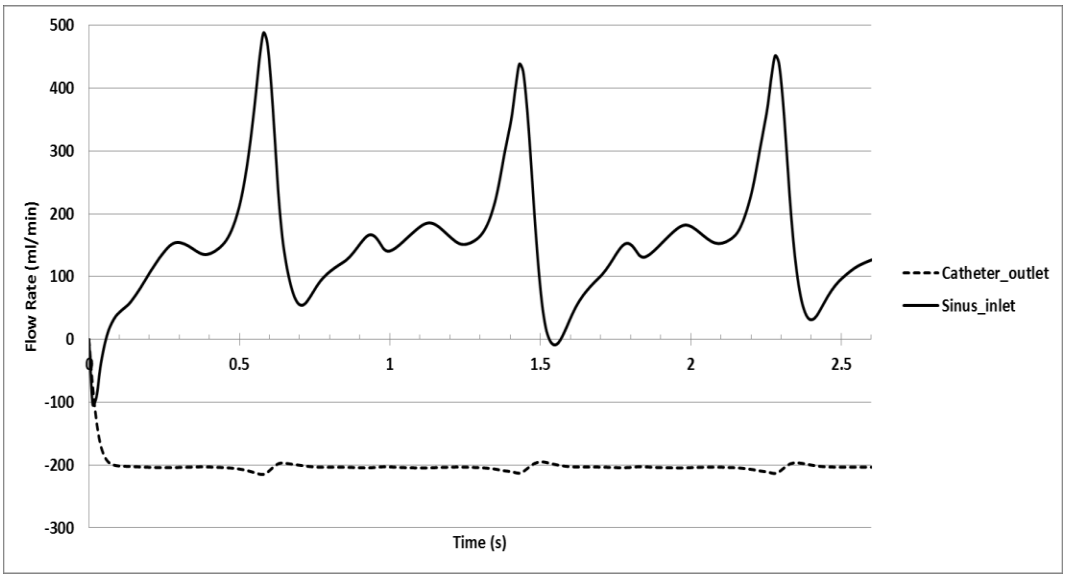

Fig. 4.12: Transient flow rates at the inlet of the sinus and in the outlet of the catheter

4.4 Three-Dimensional Effects on the Flow in Suction Catheters

All the models employed so far included a two-dimensional axisymmetric representation of the artery and the catheter. This section aims to quantify the relative impact of ignoring some three-dimensional factors which might influence the flow through the catheter. Effort was made to quantify the impact of including the major tributaries of the coronary sinus in the solution domain. Other factors which were studied included the possibility of misalignment of the catheter with center [axis?] of the artery [artery or coronary sinus?] and also the presence of slits in the catheter tip to supplement the flow entering the catheter.

4.4.1 Effect of three-dimensional coronary sinus geometry

Figure 4.13 shows a representative three-dimensional model which was created to investigate the fidelity of the results heretofore obtained by the axisymmetric model. An actual three-dimensional view of the coronary arteries was shown earlier in Figure 4.1. The geometry and tributaries of the coronary sinus vary greatly between individuals. For this study, a simpler three-dimensional model was built which mimics the greater cardiac vein (GCV) enlarging into the coronary sinus through a 90 degree bend and also includes a representation of two of its tributaries.

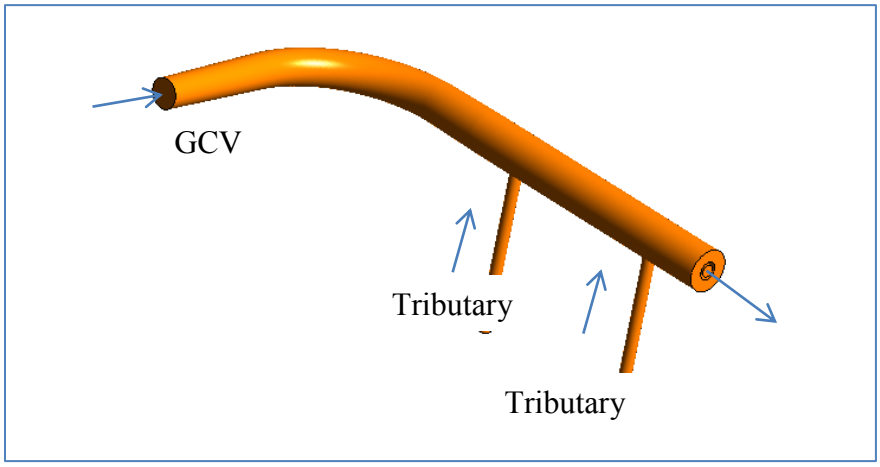

Fig. 4.13: Three-dimensional representation of the coronary sinus

To obtain the flow rate--pressure drop relationship, the flow in the coronary sinus was first solved without the presence of the suction catheter. Similar to Section 4.2.1, this simulation applied a flow rate of 122ml/min as an inlet boundary condition for the coronary sinus. Literature [125] indicates that about 70% of the flow in the coronary sinus comes from the GCV. So, 70% of 122 ml/min was applied at the inlet of the GCV.

The remaining 30% was split equally between the two modeled tributaries. The right atrial pressure of 980 Pa was applied to exit of the coronary sinus. It has been shown in the previous section that the effect of pulsation can be ignored. A steady state simulation was deployed to obtain the pressures at the inlets of the solution domain. These pressures would then be used as boundary conditions for the model which includes the presence of the suction catheter.

When the catheter was included in the model, the pressures at the GCV and tributary entrances, which were obtained earlier with a fixed flow rate simulation, were applied as opening boundary conditions. Once again, the outlet pressure of the catheter was varied parametrically. Figure 4.14 compares the results for the suction catheter flow rate versus outlet pressure obtained for the three-dimensional geometry with that for the axisymmetric approximation. The results are in very close agreement with each other. The axisymmetric model can be executed more rapidly with better spatial resolution and with a fewer number of nodes and elements.

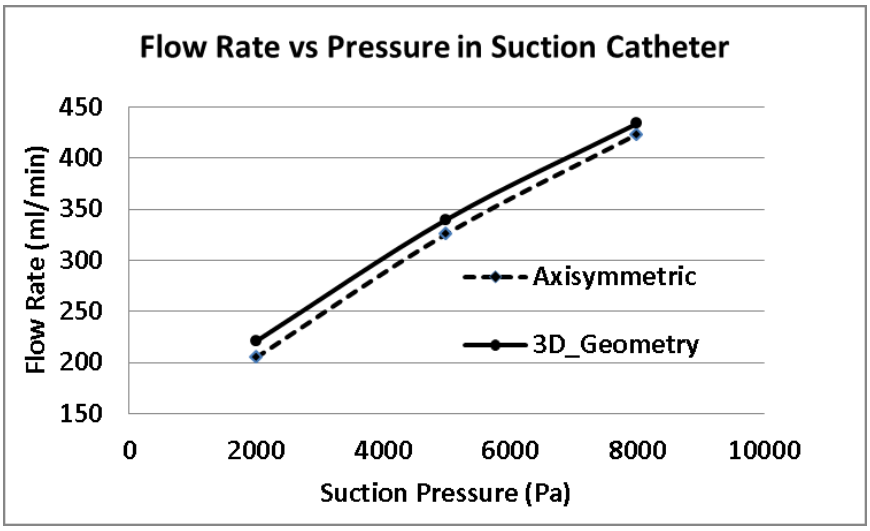

Fig. 4.14: Flow rate versus catheter outlet pressure for axisymmetric and three-dimensional geometries

Figure 4.15 has been prepared to compare the relative contributions to the flow in the suction catheter. It can be seen that up to 80% of the flow comes from the GCV. The presence of a significant amount of backflow also indicates that the use of a flow occluding balloon would not be necessary. The tributaries contribute only up to 1% of the flow in the suction catheter. It should also be noted that as the suction pressure is increased, the backflow contribution to the flow is also increased. This finding is also consistent with the axisymmetric model results.

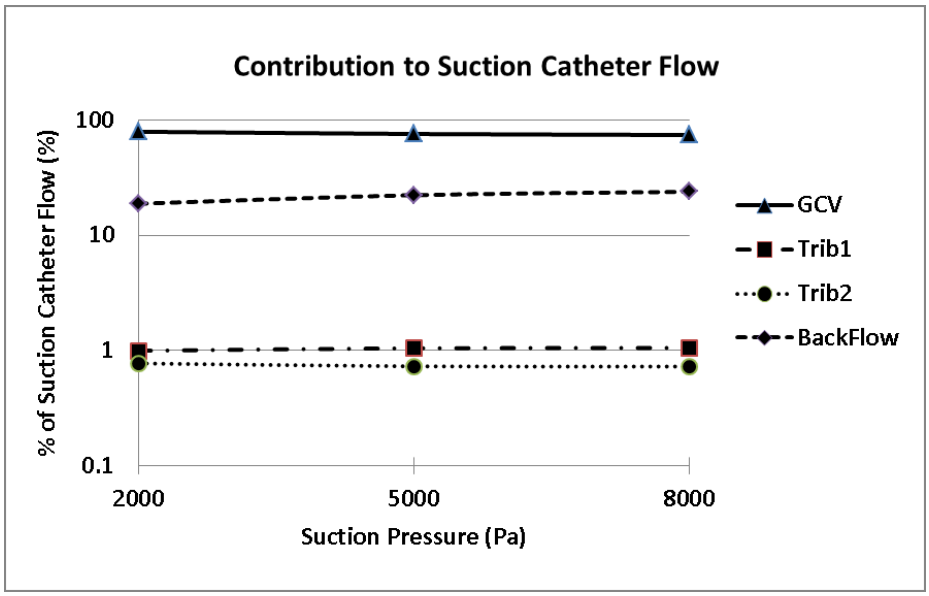

Fig. 4.15: Sources of flow to the suction catheter

4.3.2 Effect of catheter misalignment and presence of catheter slits

During the operation of the device, the central lumen of catheter may not always be aligned with the axis of the artery if a proper retaining system is not in place. This section investigates the impact of catheter misalignment on the flow through the catheter. Some catheters have slits on their sides to compensate for any loss of flow due to misalignment. The impact of such slits on the flow through the catheter is also studied here. Figure 4.16 shows a schematic diagram of a slit just downstream of the catheter tip which was investigated. The investigated catheter had four such circumferential slits.

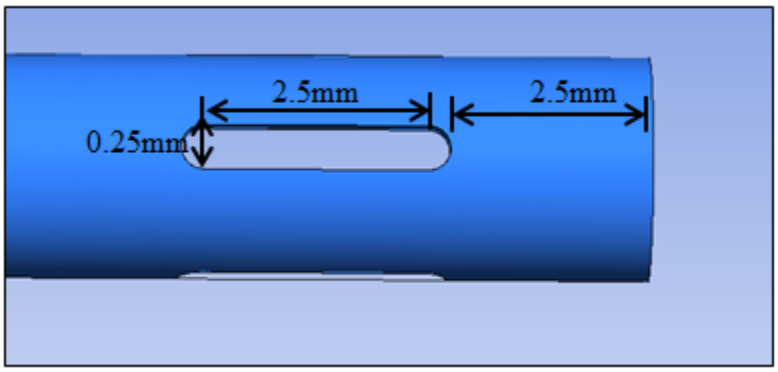

Fig. 4.16: Diagram of a catheter with slits adjacent to the tip

For the sake of efficiency, the cylindrical representation of the coronary sinus was used as it has showed good agreement with the three-dimensional results. However, axisymmetry could not be used to investigate the slits and misalignment. For the misalignment case, the axis of the catheter lumen was offset from the axis of the surrounding artery by 1mm. Table 4.1 has been prepared to show the effects of the presence of slits and misalignment on the flow rate through the catheter.

Table 4.1: Effect of slits and misalignment on the flow rate though the suction catheter

Suction Pressure (Pa)	Aligned	Presence of Slits	Catheter flow rate (ml/min)	Sinus Inlet Flow rate (ml/min)	Ratio Cath/Inlet
2000	Yes	No	205	227	0.90
2000	No	No	202	227	0.89
2000	Yes	Yes	188	201	0.94
2000	No	Yes	188	227	0.83

It can be seen from Table 1 that the effect of misalignment of the catheter has a fairly negligible effect on the flow through it. This could be due to the fact that the flow in the surrounding space is much lower than the flow in the catheter due to relatively higher suction pressure in the catheter. Also, the presence of the slits did not enhance the flow. If anything, it led to reduced flow through the catheter. This is due to the fact that the majority of the flow tends to come in through the slits. This fluid needs to turn in order to flow along the catheter which adds additional pressure drop. The fluid coming in through the slits also restricts the amount of flow which can enter through the actual inlet of the catheter. A study of the effect of the presence of circumferential circular holes in the catheter tip on the flow rate also yielded similar results, and those details are displayed in Appendix C.

Chapter 5

CONCLUDING REMARKS

Numerical modeling and simulation was employed as a means of analyzing physical phenomena pertaining to the design and development of biomedical devices and media. Simulation can be a very powerful and efficient tool for analyzing the various participating physical processes. It can be used to either substitute for or enhance experimental work. Developing numerical models often involves performing a balance between accuracy, time, robustness, and memory requirements. In this work, appropriate numerical models of various fluid flow processes were developed to aid the design, operation, and manufacture of biomedical devices. Care was taken with the mesh and time steps to obtain a numerically accurate solution. Whenever simplifying model assumptions were made for the sake of efficiency, the results were validated with literature results or more complex models. The major applications of the work are with respect to the design of infusion ports, manufacture of fine-fibers, and operation of suction catheters to extract spent contrast media. The adopted principles and methodology can also be applied to wide variety of related fluid flow processes.

To the best knowledge of the author, the work presented in the second chapter is the first attempt to quantify the fluid flow and mass transfer characteristics of human-body infusion ports. The work was motivated by the need to characterize competing versions of such therapy-facilitating systems.

Two of the systems (A and B in the designation of the report) are already available in the marketplace. The other, system C, is still in the developmental stage. The method of investigation used here was based on numerical simulation. Three-dimensional, unsteady solutions of the Navier-Stokes, continuity, and species conservation equations were performed.

The general configuration of the three systems is the same. A reservoir containing the medium to be infused is attached to a tube-like catheter which delivers the medium to its point of use. Fluid motion is activated by the introduction of a fixed volume of the medium into the reservoir. The liquid may be either the same or different from that in the reservoir.

The differences among the systems are geometrical, including reservoirs of different sizes and shapes and in the mode of attachment of an extraction catheter to the reservoir. In particular, system C had an optimal attachment which guaranteed the absence of flow separation. The attachment mode of System A gave rise to flow separation, and that of B gave rise to incipient separation. The flow velocities, for normal operation were so small that hemolysis did not occur in any of the ports, regardless of the attachment mode.

The successful use of the reservoir as a mixing chamber for different fluids has also been validated. The feasibility of operating the ports at higher flow rates and also in both flow extraction and delivery modes was established.

In the third chapter, the use of the Coanda effect as a means for controlling the trajectories of still-molten polymer fibers during the melt-blowing process has been investigated by means of numerical simulation. The fiber trajectories has a significant impact on the physical properties of the fabrics produced the melt-blown process. Such fabrics are used to make a wide variety of biomedical materials such as surgical masks, caps, gowns, drapes and medical packaging equipment. They are also used to manufacture filtration materials for dialysis applications and air filtration. The Coanda effect can also be used to explain other biomedical and physiological phenomena such as flow in fluidic ventilators, air distribution in lungs, fetal blood circulation, and human phonation [65-67].

Although the published literature has fully focused on the Coanda effect as created by curved bounding walls, the present study has investigated both plane and curved walls. A significant outcome of the work is the demonstration that plane walls are able to give rise to important Coanda effects that are comparable to those created by curved walls
To provide a broad spectrum of physical situations that might be candidates for practical implementation of the Coanda effect in fine-fiber production, parametric variations were made of the lateral standoff distance between the Coanda-creating wall and the location at which the fiber exits from the forming die. Also varied was the streamwise length of the Coanda wall. The results of the simulations were presented for parametric locations downstream of the fiber exit. Particular attention was given to the transverse velocity in

the direction of the Coanda wall, and the magnitude of this quantity was taken as the metric for quantifying both the presence of the Coanda effect and its magnitude. For the plane Coanda wall, it was found that at a dimensionless downstream distance of 0.5 from the fiber exit, the Coanda effect is of little practical significance. In contrast, enhancements of the transverse velocity are significant from the standpoint of practical applications at dimensionless downstream distances of 1.0 and 1.5.

Two curved Coanda-wall cases were also considered, the distinction between them being the degree of curvature. One of the unique findings of the investigation is that the magnitudes of the Coanda effects induced by a curved wall and a plane wall are comparable. Specifically, with respect to the curved wall, it was found that the greatest augmentation of the transverse velocity occurs at a downstream distance corresponding to the location of the narrow waist of the curvature.

In the fourth chapter, the operation of a suction catheter situated in the coronary sinus to extract spent contrast media in order to prevent contrast-induced nephropathy (CIN) was analyzed. Currently, there are no efficacious methods of preventing or treating CIN for patients with certain pre-existing conditions. The required suction pressure in the catheter to extract the desired amount of spent media was evaluated. The potential risk of hemolysis by the suction catheter was assessed. One significant finding was the lack of necessity to employ a flow-occluding balloon to prevent the contrast media from escaping into the right atrium of the heart when the device is in operation. This avoidance

would significantly reduce the cost and complexity of the device. The effect of the timewise pulsatile nature of the blood flow on the operation of the device was also quantified. Commonly used modifications to the catheter tip such as including side holes and slits were also explored. In general, they did not offer any significant enhancement to the flow through the catheter.

Though the numerical analysis here was limited to a suction catheter in the coronary sinus for extracting spent contrast media, the same principles would apply to suction catheters operating anywhere in the body for applications such as dialysis and removal of blood clots.

BIBLIOGRAPHY

1. Chung TJ, Computational fluid dynamics. New York: Cambridge University Press, 2010
2. Bose TK (Tarit Kumar), Computational fluid dynamics. New York: Wiley, 1988
3. Magoulès F, Computational fluid dynamics. Boca Raton: CRC Press, 2011
4. Zienkiewicz OC, Taylor RL, and Zhu JZ, Finite element method: its basis and fundamentals. Amsterdam; Boston: Butterworth-Heinemann, 2013
5. Reddy JN and Gartling DK, The finite element method in heat transfer and fluid dynamics. Boca Raton, FL: CRC Press, 2001
6. Zienkiewicz OC, Taylor RL, and Nithiarasu P, The finite element method for fluid dynamics. Amsterdam; Boston: Elsevier Butterworth-Heinemann, 2005
7. Versteeg HK (Henk Kaarle) and Malalasekara W, An introduction to computational fluid dynamics: the finite volume method. Harlow, England; New York: Pearson Education Ltd., 2007
8. Pletcher RH, Tannehill JC, and Anderson DA, Computational fluid mechanics and heat transfer. Boca Raton, FL: CRC Press, Third Edition
9. David LB, with contributions by Boris JP ... [et al.]. Finite-difference techniques for vectorized fluid dynamics calculations. New York: Springer-Verlag, 1981
10. Schneck DJ, "*An outline of cardiovascular structure and function",* In: The Biomedical Engineering Handbook, 2000; 1(2); CRC Press, Boca Raton
11. Radaeilli AG and Peiro J, "*On the segmentation of vascular geometries from medical images",* International Journal for Numerical Methods in Engineering, 2010; 26(1): 3-34
12. Steinman D, "*Image-Based Computational Fluid Dynamics Modeling in Realistic Arterial Geometries*", Annals of Biomedical Engineering, 2002; 30: 483-497
13. Cebral JR, et al. "*From medical images to anatomically accurate finite element grids*", International Journal for Numerical Methods in Engineering, 2001; 51(8): 985-1008

14. Pal R, "*Rheology of concentrated suspensions of deformable elastic particles such as human erythrocytes*", Journal of Biomechanics, 2003; 36: 981-989
15. De Gruttola SK, et al. "*Computational simulation of a non-Newtonian model of the blood separation process*", Artif. Organs, 2005; 29: 949-959
16. Yilmaz F, and Gundogdu YM, "*A critical review on blood flow in large arteries; relevance to blood rheology, viscosity models, and physiological conditions",* Korea-Australia Rheology Journal, 2008; 20(4): 197-211
17. Crowley TA, and Pizziconi V, "*Isolation of plasma from whole blood using planar microfilters for lab-on-a-chip applications*", Lab Chip, 2005; 5: 922-929
18. Toda K, and Furuse H, "*Extension of Einstein's viscosity equation to that for concentrated dispersions of solutes and particles*", Journal of Bioscience and Bioengieering, 2006; 102: 524-528
19. Cho YI and Kensey KR, "*Effects of the non-Newtonian viscosity of blood on hemodynamics of diseased arterial flows: part 1, steady flows*", Biorheology, 1991; 28: 241-262
20. Johnston BM, Johnston PR, Corney S, and Kilpatrick D, "*Non-Newtonian blood flow in human right coronary arteries: steady state simulations*", Journal of Biomechanics, 2004; 37: 709-720
21. Gijsen FJ, et al., "*The influence of the non-Newtonian properties of blood on the flow in large arteries: unsteady flow in a 90-degree curved tube*", Journal of Biomechanics, 1999; 32: 705-713
22. Rojas HAG, "*Numerical implementation of viscoelastic blood flow in a simplified arterial geometry*", Medical Engineering and Physics, 2007: 29: 491-496
23. Rajagopal KR, and Srinivasa AR, "*A thermodynamic frame work for rate type fluid models*", Journal of Non-Newtonian Fluid Mechanics, 2000; 88: 207-227
24. Yeleswarapu KK, et al., "*The flow of blood in tubes: theory and experiment*", Mechanics Research Communications, 1998; 25: 257-262
25. Steffe JF, Rheological methods in food process engineering. Freeman press, 1996
26. Bertrand ME, et al., "*Coronary sinus blood flow at rest and during isometric exercise in patients with aortic valve disease: Mechanism of angina pectoris in*

presence of normal coronary arteries", American Journal of Cardiology, 1981; 47(2): 199-205

27. Ganz W, et al., "*Measurement of Coronary Sinus Blood Flow by Continuous Thermodilution in Man",* American Heart Association, 1971; 44: 181
28. Gundogdu MY, and Çarpinlioglu MO, "*Present state of art on pulsatile flow theory, part 1. laminar and transitional flow regimes*", Japan Society of Mechanical Engineering Int. J, 1999a; 42: 384-397
29. Gundogdu MY and Çarpinlioglu MO, "*Present state of art on pulsatile flow theory, part 2. turbulent flow regime*", Japan Society of Mechanical Engineering Int. J, 1999b; 42: 398-410
30. Steven D, John MT, Keefe BM, Gerson R, and Arnold AF, "*Experimental fluid mechanics of pulsatile artificial blood pumps*", Annual Review of Fluid Mechanics Vol. 38: 65-86
31. Moin P, and Krishnan M, " *Direct Numerical Simulation: A Tool in Turbulence Research",* Annual review of Fluid Mechanics, 1998; 30: 539-578
32. Mittal R, et al., "*Application of large-eddy simulation to the study of pulsatile flow in modeled arterial stenosis",* Journal of Biomechanical Engineering, 2001; 123(4): 325-332
33. Molla MM, et al., "*LES of additive and non-additive pulsatile flows in a model arterial stenosis",* Computational Methods for Biomechanical and Biomedical Engineering, 2010: 13: 105-120
34. Paul M, et al., " *Large-Eddy simulation of pulsatile blood flow*", Medical Engineering and Physics, 2009; 31: 153-159
35. Dodge DW and Metzner AB, "*Turbulent flow of non-newtonian systems*", AIChE Journal, 1959; 5: 189-204
36. Wilson KC and Thomas AD, "*A new analysis of the turbulent flow of non-newtonian fluids*", The Canadian Journal of Chemical Engineering, 1985; 63(4): 539-546

37. Draad AA, Kuiken GDC, and Nieuwstadt FTM, "*Laminar-turbulent transition in pipe flow for Newtonian and non-Newtonian fluids*", Journal of Fluid Mechanics, 1998; 377: 267-312
38. ANSYS CFX-Solver Theory Guide
39. Wilcox DC, Turbulence Modeling for CFD. La Canada, California: DCW Industries, 2nd edition, 1981
40. Piquet J, Turbulent flows: models and physics. Berlin; New York: Springer-Verlag, 1999
41. Cebeci T, Analysis of turbulent flows with computer programs. Oxford: Butterworth-Heinemann, 2013.
42. Menter F, et al., "*Transition Modelling Based on Local Variables*", 5th International Symposium on Engineering Turbulence Modeling and Measurements, Mallorca, Spain, 2002
43. Menter F, et al., "*A Correlation –Based Transition Model Using Local Variables, Part I – Model Formulation*", Proceedings of ASME Turbo Expo Power for Land, Sea, and Air, Vienna, Austria, 2004
44. Menter F, et al., "*A Correlation –Based Transition Model Using Local Variables, Part II – Test Cases and Industrial Applications*", Proceedings of ASME Turbo Expo Power for Land, Sea, and Air, Vienna, Austria, 2004
45. Abraham JP, et al., "*Internal flows which transit from turbulent through intermittent through to laminar",* International Journal of Thermal Science, 2010; 49(2): 256-263
46. Abraham JP, et al., "*Pulsating fluid flows undergoing transition between laminar, transitional, and turbulent flow regimes*", Proceedings of ASME Summer Bioengineerin Conference, 2009; A: 493-494
47. Lovik RD, et al., "*Laminarization and turbulentization in a pulsatile pipe flow",* Numerical Heat Transfer, 2009; 56: 861-879
48. ANSYS Workbench 12.0 User Manual and Theory
49. Kalita P, et al., "*Mechanical Models of Artery Walls*", Archives of Computational Methods in Engineering, 2008; 15: 1-36

50. Holzapfel GA, "*Structural and numerical models for the elastic response of arterial walls with residual stresses"* In: Biomechanics of Soft Tissue in Cardiovascular System, 2003, Springer, New York: 109-184
51. Dobrin PB, " *Distribution of lamellar deformations: implications of properties of the arterial media",* Hypertension, 1999; 33(3): 806-810
52. Hayashi K, "*Experimental approaches on measuring the mechanical properties andconstitutive laws of arterial walls",* Journal of Biomechanical Engineering, 1993; 115(4b): 481-488
53. Baldwin AL, "*Use of optical coherence tomography to measure mechanical and transport properties pulsating artery walls",* ASME Advances in Bioengineering, 2001; 50: 677-678
54. Walters KR, "*Ultrasonic estimation of mechanical properties of pulmonary arterial wall under normoxic and hypoxic conditions*", AIP Conference Proceedings, 2005; 760: 1541-1548
55. Quinn NM, "*An experimental and numerical investigation into the deformation profiles of mock arteries",* ASME Summer Bioengineering Conference, 2007; 465-466
56. Li MX, et al., "*Numerical analysis of pulsatile blood flow and vessel wall mechanics in different degrees of stenoses",* Journal of Biomechanics, 2007; 40: 3715-3724
57. Bazilevs Y, et al., "*Isogeometric fluid-structure interaction analysis with applications to arterial blood flow*", Computational Mechanics, 2006; 38: 310-322
58. Di Martino ES, et al., "*Fluid Structure interaction within realistic three-dimensional models of the aneurysmatic aorta to assess the risk of the rupture of the aneurysm",* Medical Engineering and Physics, 2001; 23: 647-655
59. Khanafer K, and Berguer R, "*Fluid-Structure interaction analysis of turbulent pulsatile flow within a layered aortic wall as related to aortic dissection",* Journal of Biomechanics, 2009; 42: 2642-2648

60. Krutka HM, Shambaugh RL, and Papavassiliou DV, "*Effects of die geometry on the flow field of the melt-blowing process*", Industrial & engineering chemistry research, 2003; *42*(22): 5541-5553
61. Chen T and Huang X, "*Modeling polymer air drawing in the melt blowing nonwoven process*", Textile research journal, 2003; 73(7): 651-654
62. Lee Y and Wadsworth LC, "*Effects of melt-blowing process conditions on morphological and mechanical properties of polypropylene webs*", Polymer, 1992; *33*(6): 1200-1209
63. Kayser JC and Shambaugh RL, "*The manufacture of continuous polymeric filaments by the melt-blowing process*", Polymer Engineering & Science, 1990; *30*(19): 1237-1251
64. Chen T, Wang X, and Huang X, "*Modeling the air-jet flow field of a dual slot die in the melt blowing nonwoven process*", Textile research journal, 2004; *74*(11): 1018-1024
65. Erath BD and Plesniak MW, "*The occurrence of the Coanda effect in pulsatile flow through static models of the human vocal folds*", The Journal of the Acoustical Society of America, 2006; *120*: 1000
66. French JW and Guntheroth WG, "*An Explanation of Asymmetric Upper Extremity Blood Pressures in Supravalvular Aortic Stenosis The Coanda Effect*", Circulation, 1970; *42*(1): 31-36
67. Klain M, and Smith RB, "*Fluidic technology*", Anaesthesia, 1976; *31*(6): 750-757
68. Bartorelli AL and Marenzi G, "*Contrast-Induced Nephropathy*", Journal of Interventional Cardiology, 2008; 21: 74-85
69. McCollough AP and Soman SS, "*Contrast-Induced Nephropathy",* Critical Care Clinics, 2005; 21: 261-280
70. Gleeson TG and Bulugahapitiya S, "*Review, Contrast-Induced Nephropathy*", American Journal of Roentgenology, 2004; 183: 1673-1689
71. Wong GTC and Irwin MG, "*Contrast-Induced Nephropathy"*, British Journal of Anesthesiology, 2007; 99(4): 474-483

72. Walsh SR, Tang T, Gaunt ME, and Boyle JR, "*Contrast-Induced Nephropathy",* Journal of Endovascular Therapy, 2007; 14(1): 92-100
73. Baret BJ and Parfrey S, "*Clinical Practice. Preventing nephropathy induced by contrast* medium", New England Journal of Medicine, 2006; 354(4): 379-386
74. Hou SH, et al., "*Hospital-acquired renal insufficiency: a prospective study"*, American Journal of Medicine, 1983; 74: 243-248
75. Levy EM, et al., "*The effect of acute renal failure on mortality. A cohort analysis",* Journal of the American Medical Association, 1996; 275: 1489-1494
76. Lindsay J, et al., "*Percutaneous coronary intervention-associated foreshadows increased risk of late adverse events in patients with normal baseline serum creatinine",* catheter Cardiovascular Intervention, 2003; 59: 338-343
77. Harjai KJ, et al., "*A comparison of contemporary definition of contrast nephropathy in patients undergoing percutaneous coronary intervention and a proposal for a novel nephropathy grading system",* American Journal of Cardiology, 2008; 101(6): 812-819
78. Reich D, "*Method and Device for preventing contrast associated nephropathy",* US Patent No. 6554819
79. Al-Rashdan IR, "*Method and Device for preventing contrast associated nephropathy",* US Patent No. 7824357
80. Blackshear P and Blackshear G, "*Mechanical Hemolysis",* Handbook of Bioengineering edited by Skalak R and Chien S, Mc-Graw-Hill, New York, NY, 1987
81. Lu P, Lai H, and Liu J, "*A Re-evaluation and Discussion on the Threshold Limit for Hemolysis in a Turbulent Shear Flow*", Journal of Biomechanics, 2001; 34: 1361-1364
82. Fry DL, "*Acute vascular endothelial changes associated with increased blood velocity gradients",* Circulation Research, 1968; 22: 165-197
83. Ramstack JM, Zuckerman L, and Mockros LF, "*Shear Induced Activation of Platelets"* , Journal of Biomechanics, 1979; 12: 113-125

84. Pennati G, Balossino R, Dubini G, and Migliavacca F, "*Numerical simulation of thrombus aspiration in two realistic models of catheter tips*", Artificial Organs, 2010; *34*(4): 301-310
85. Soleimani S, Pennati G, and Dubini G, "*Numerical Simulation of Thrombus Aspiration Catheter: Preliminary Results*", International Conference on Advancements of Medicine and Health Care through Technology, 2011 January: 256-259
86. Gijsen FJH, Van de Vosse FN, and Janssen JD, "*The influence of the non-Newtonian properties of blood on the flow in large arteries: steady flow in a carotid bifurcation model*", J. Biomech, 1999; 32: 601–608
87. Benard N, Perrault R, and Coisne D, "*Computational approach to estimating the effects of blood properties on changes in intra-stent flow*", Ann. Biomed. Eng., 2006; 34: 1259–1271
88. Akl-Besharah JM, Mumford CJ, Akashah SA, and Salman O, "*Prediction of the viscosity of lubricating oil blends*", Fuel, 1989; 68: 809–811
89. Grigioni M, Daniele C, D'Avenio G, and Barbaro V, "*A discussion on the threshold limit for hemolysis related to Reynolds shear stress*", J. Biomech, 1999; 32: 1107–1112
90. Williams A, Hughes D, and Nyborg W, "*Hemolysis near a transversely oscillating wire*", Science, 1970; 169: 871–873
91. Bacher R and Williams M, "*Hemolysis in capillary flow*", J. Lab. Clin. Med, 1970; 76: 485–496
92. Rooney J, "*Hemolysis near an ultrasonically pulsating gas bubble*", Science, 1970; 169: 869–871
93. Paul R, Apel J, Klaus S, Schugner F, Schwindke P, and Reul H, "*Shear stress related blood damage in laminar Couette flow*", Artif. Organs., 2003; 27: 517–529
94. Sallam A, and Hwang N, "*Human red blood cell hemolysis in a turbulent shear flow. Contribution of Reynolds shear stress*", Biorheology, 1984; 21: 783–797

95. Wurzinger L, Optiz R, Blasberg P, and Schmid-Schonbein H, "*Platelet and coagulation parameters following millisecond exposure to laminar shear stress*", Thromb. Haemostasis, 1985; 54: 381–386

96. Sutera S and Mehrjardi M, "*Deformation and fragmentation of human RBC in turbulent shear flow*", Biophys. J., 1975; 15: 1–10

97. Leverett L, Hellums J, Alfrey C, and Lynch B, "*Red blood cell damage by shear stress*", Biophys. J., 1972; 12: 257–273

98. Shapiro S and Williams M, "*Hemolysis in simple shear flows*", Am. Inst. Chem. Eng., 1970; 16: 575–580

99. Steinbach J, PhD Thesis, University of Minnesota, Minneapolis, 1970

100. Omel'chenko AI, et al. "*Transport of aqueous solutions in laser-irradiated biological tissues*", Temp Symposium Entry. International Society for Optics and Photonics, 2004; Jan: 257-260

101. Menter FR, "*Two-equation eddy-viscosity turbulence models for engineering applications*", AIAA journal, 1994; 32(8): 1598-1605

102. Wilcox DA, "*Simulation of transition with a two-equation turbulence model*". AIAA journal, 1994; *32*(2): 247-255

103. Patel VC, Rodi W, and Scheuerer G, "*Turbulence models for near-wall and low Reynolds number flows-a review*", AIAA journal, 1985; *23*(9): 1308-1319

104. Montalvo RA, "*Implantable infusion port with reduced internal volume*", US Patent 5,476,460; 1995

105. Miozzi M, Lalli F, and Romano GP, "*Experimental investigation of a free-surface turbulent jet with Coanda effect*", Experiments in Fluids, 2010; *49*(1): 341-353

106. Shambaugh BR, Papavassiliou DV, and Shambaugh RL, "*Next-Generation Modeling of Melt Blowing*", Ind. Eng. Chem. Res., 2011; 50: 12233–12245

107. Xie S and Zeng Y, "*Turbulent Air Flow Field and Fiber Whipping Motion in the Melt Blowing Process: Experimental Study*". Ind. Eng. Chem. Res., 2012; 51: 5346−5352

108. Zhou C, Tan DH, Janakiraman AP, and Kumar S, "*Modeling the Melt Blowing of Viscoelastic Materials*", Chem. Eng. Sci., 2011; 66: 4172-4183

109. Chen T, Zhang C, Chen X, and Li L, "*Numerical Computation of the Fiber Diameter of Melt Blown Nonwovens Produced by the Inset Die*", J. App. Polym. Sci., 2009; 111: 1775-1779

110. Milligan MW, Lu F, and Buntin RR, "*The Use of Crossflow to Improve Nonwoven Melt-Blown Fibers*", J. App. Polym. Sci., 1992; 44: 279-288

111. Klinzing WP and Sparrow EM, "*Three-Dimensional Fluid Flow in the Processing of Fine Fiber",* Ind. Eng. Chem. Res., 2008; 47: 8754-8761

112. Launder BE and Rodi W, "*The Turbulent Wall Jet - Measurements and Modeling*", Ann. Rev. Fluid Mech., 1983; 15: 429-459

113. Triboix A and Marchal D, "*Satbility Analysis of the Mechanism of Jet Attachment to Walls*", IJHMT, 2002; 45: 2769-2775

114. Kanna PR and Das MK, "*Numerical Simulation of Two-dimensional Laminar Incompressible Offset Jet Flows",* Int. J. Numer. Meth. Fluid, 2005; 49: 439-464

115. Klinzing WP and Sparrow EM, "*Evaluation of Turbulence Models for External Flows*", Numer. Heat Transfer, Part A, 2009; 55: 205-228

116. Launder BE and Spalding DB, "*The Numerical Computation of Turbulent Flows*", Comp. Meth. Appl. Mech. Eng., 1974; 3: 269-289

117. Menter FR, Kuntz M, and Langtry R, "*Ten Years of Industrial Experience with SST Turbulence Model*", Proc. Fourth Int. Symp. on Turbulence, Heat and Mass Transfer, 2003; 625-632

118. Marcus ML, Wilson RF, and White CW, "*Methods of measurement of myocardial blood flow in patients: a critical review*", Circulation, 1987; *76*(2): 245-253

119. Goodale WT, Lubin M, Eckenhoff JE, Hafkenschiel JH, and Banfield WG, " *Coronary sinus catheterization for studying coronary blood flow and myocardial metabolism*", American Journal of Physiology--Legacy Content, 1948; *152*(2): 340-355

120. Bing RJ, et al., "*The measurement of coronary blood flow, oxygen consumption, and efficiency of the left ventricle in man*", American heart journal, 1949; 38(1): 1-24

121. Sakuma H, Kawada N, Takeda K, and Higgins CB, "*MR measurement of coronary blood flow*", Journal of Magnetic Resonance Imaging, 1999; *10*(5): 728-733

122. Afonso SKODA, "*A thermodilution flowmeter*", Journal of applied physiology, 1966; *21*(6): 1883-1886

123. Van Rossum AC, Visser FC, Hofman MB, Galjee MA, Westerhof N, and Valk J, " *Global left ventricular perfusion: noninvasive measurement with cine MR imaging and phase velocity mapping of coronary venous outflow*", Radiology, 1992; *182*(3): 685-691

124. Pham T and Sun W, "*Characterization of the mechanical properties of the coronary sinus for percutaneous transvenous mitral annuloplasty*", Acta Biomaterialia, 2010; 6(11): 4336-4344

125. Hood Jr. WB, "*Regional venous drainage of the human heart*", British Heart Journal, 1968; *30*(1): 105

Appendix A

STREAMLINES AND VECTOR DIAGRAMS FOR VASCULAR ACCESS PORTS IN FORWARD FLOW AT 450ML/MIN

A.1 Three-dimensional streamlines

Figures A.1(a) – A.1(c) represent the three-dimensional streamlines for Port C, Port A, and, Port B respectively. Five streamlines were started at the inlet of the reservoirs of all the ports. For steady flow, the streamlines represent the path traveled by the fluid particles which are injected at a certain location. The results presented here are for a flow of 450 ml/min at 1 second after the injection of fluid begins.

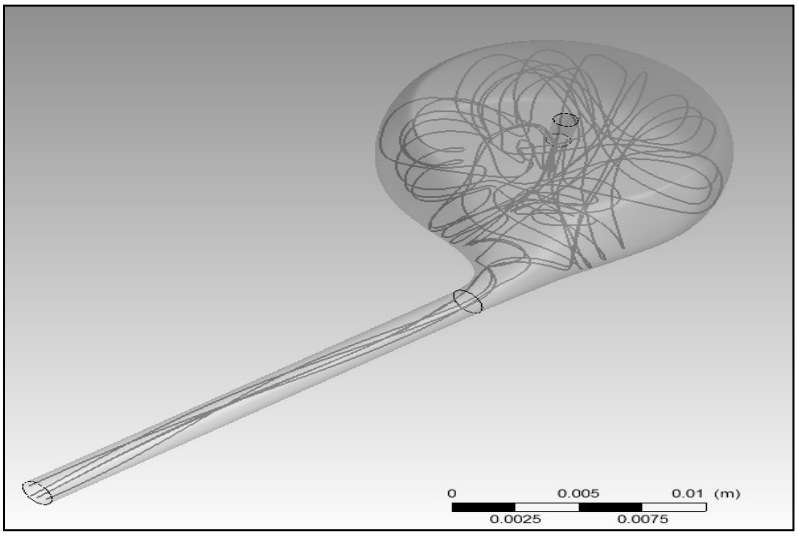

(a)

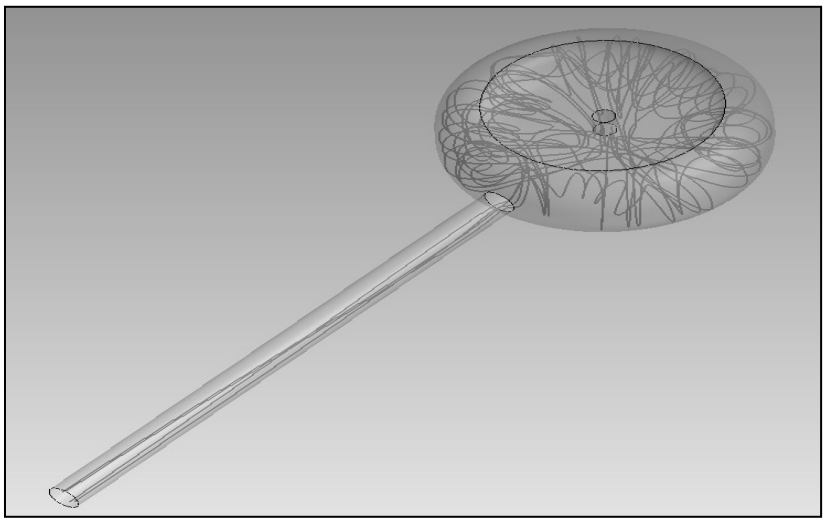

(b)

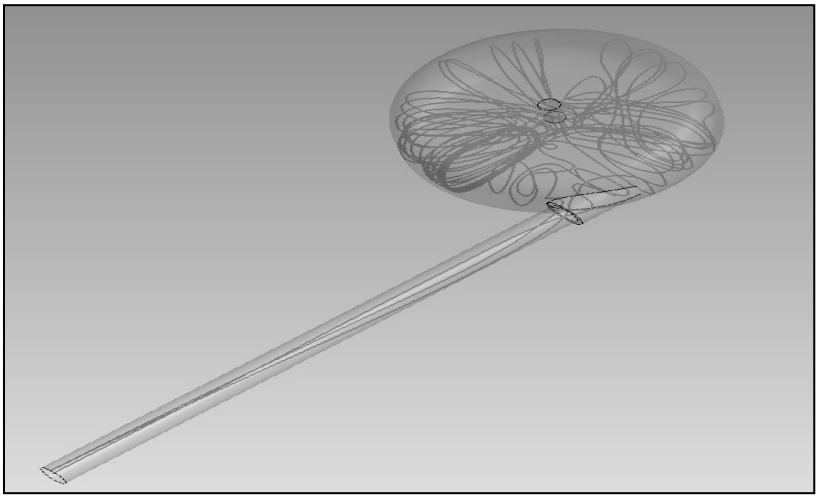

(c)

Fig. A.1: Three dimensional streamlines originating at inlet (a) Port C; (b) Port B; (c) Port A

A.2 Velocity vectors

Velocity vectors represent the magnitude and direction of fluid flow at various locations. Figures A.2(a) –A.2(c) show the velocity vectors entering the catheter for Ports A, B, and, C respectively.

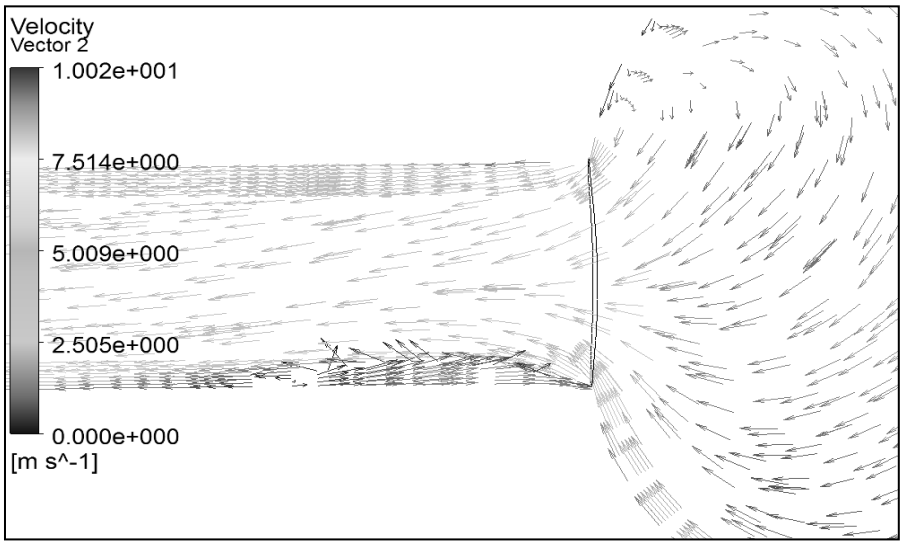

(a)

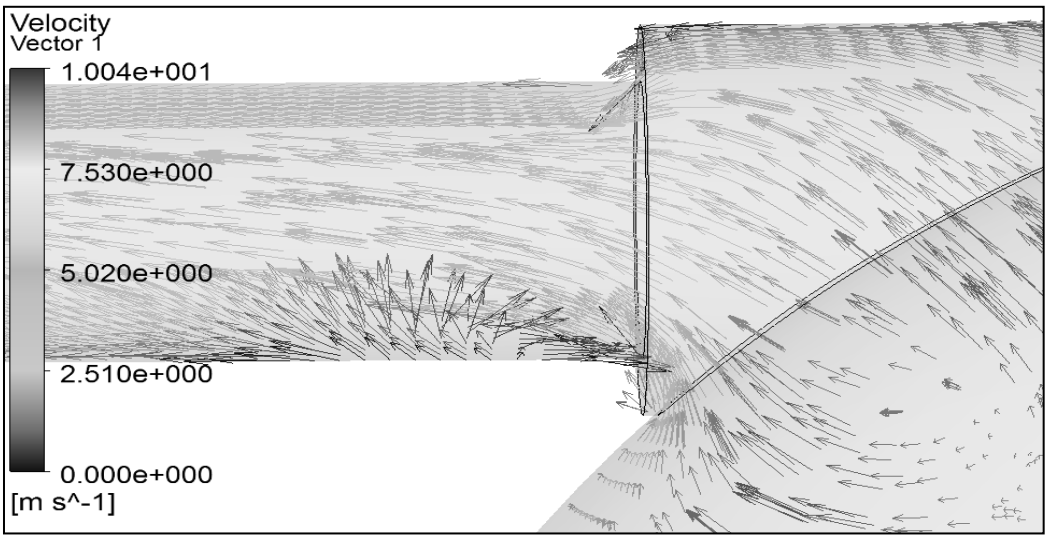

(b)

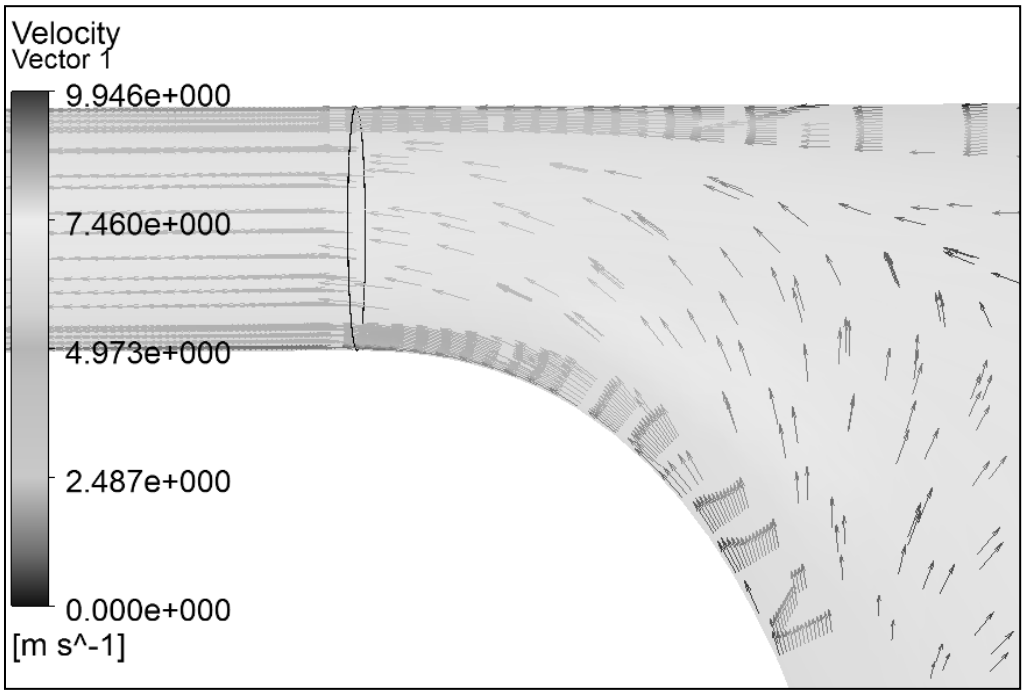

(c)

Fig. A.2: Velocity Vectors (a) Port A; (b) Port B; (c) Port C

Appendix B

DIAGRAMS DEPICTING EFFECT OF VOLUME-REDUCING MEMBERS ON FLOW PATTERNS

B.1Results for Port C

B.1.1 Forward Flow for Port C

B.1.1A Three-dimensional streamlines

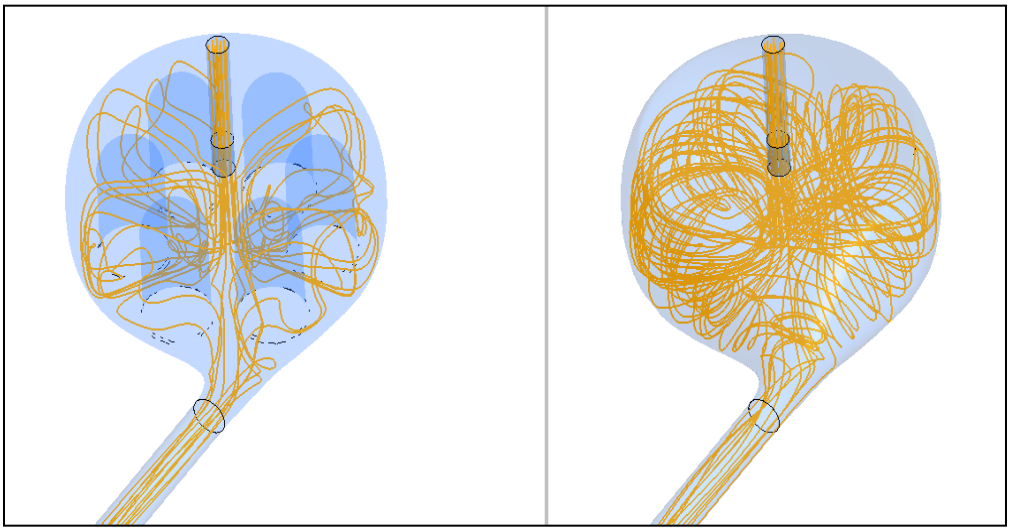

Fig. B.1: Three-dimensional streamlines for the Port C in forward flow, left with volume reducing members and right without volume reducing members

B.1.1B Surface streamlines, vector diagrams and velocity contours

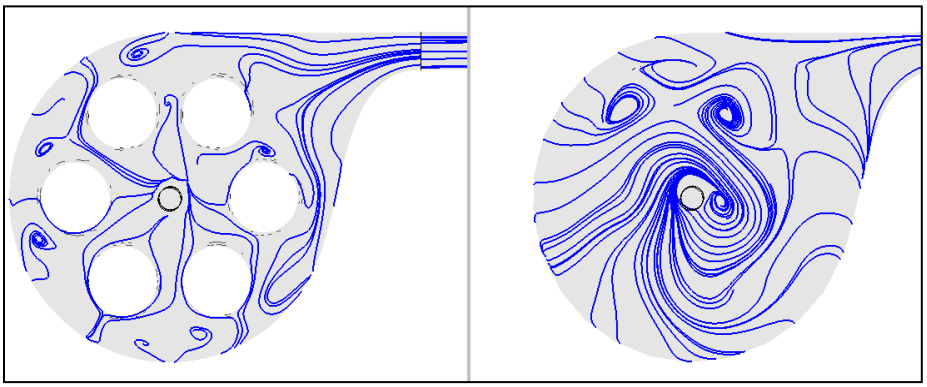

Fig. B.2(a): Surface streamlines on a central plane for the Port C in forward flow

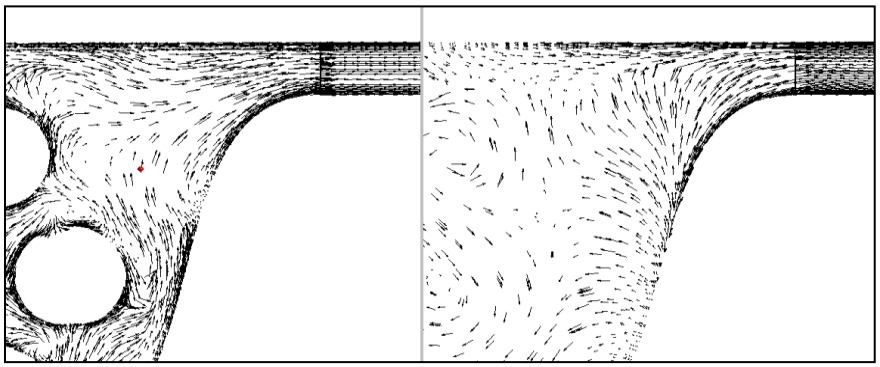

Fig. B.2(b): Velocity vectors in the plane corresponding to Fig. B.2(a)

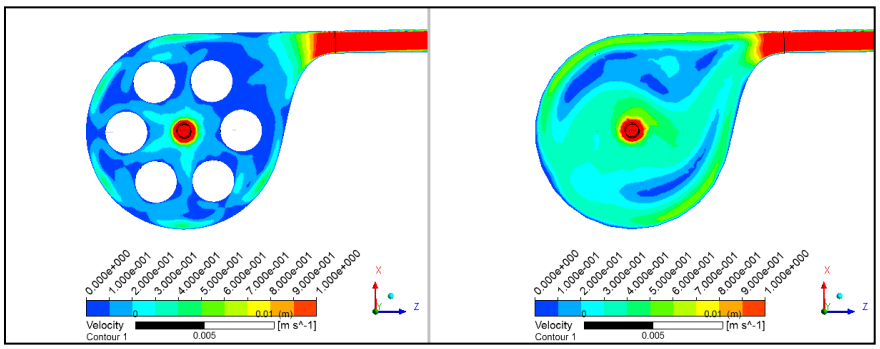

Fig. B.2(c): Velocity contours in plane corresponding to Fig. B.2(a) (scaled: 0 - 1 m/s)

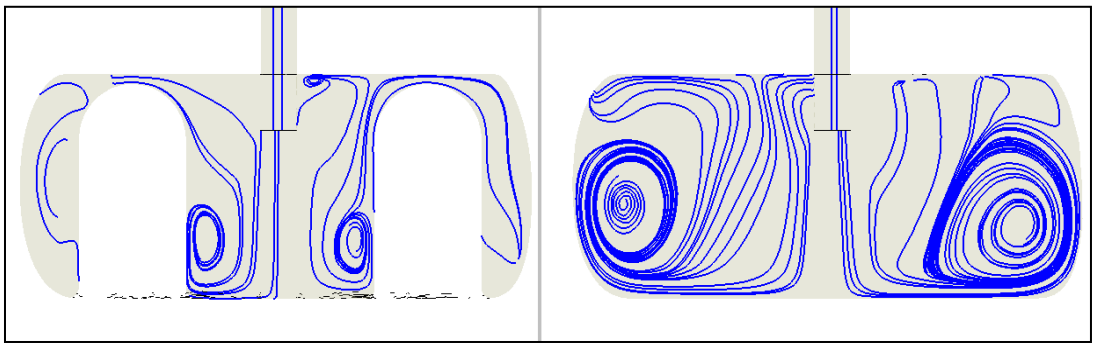

Fig. B.3(a): Surface Streamlines in a plane perpendicular to Fig. B.2(a)

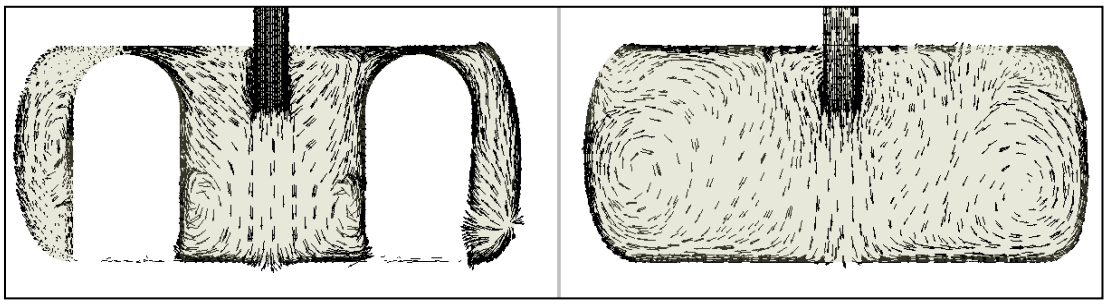

Fig. B.3(b): Velocity vectors in a plane corresponding to Fig. B.3(a)

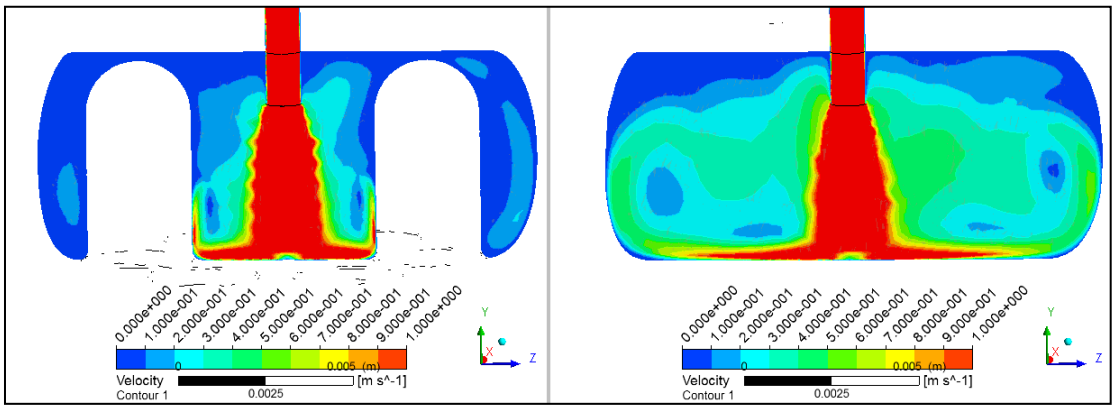

Fig. B.3(c): Velocity contours in a plane corresponding to Fig. B.3(a) (scaled between 0 and 1 m/s)

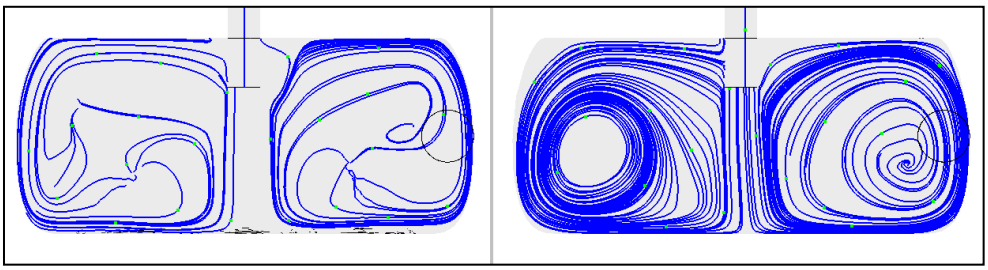

Fig. B.4(a): Surface Streamlines in a plane perpendicular to Figs. B.2(a) and B.3(a)

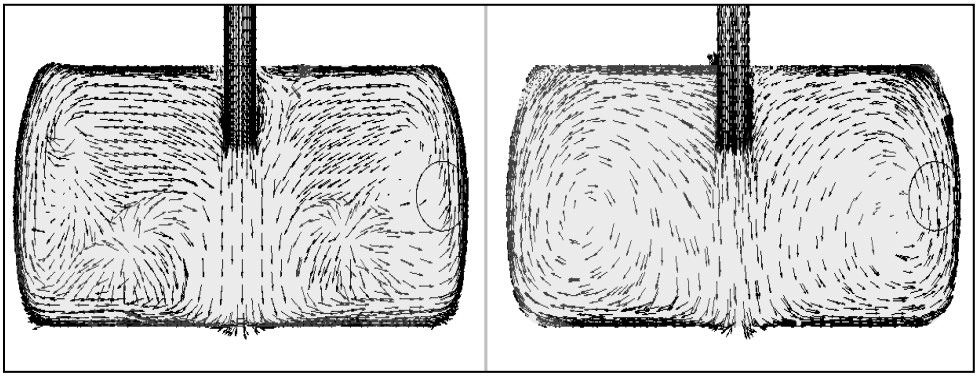

Fig. B.4(b): Velocity vectors in a plane corresponding to Fig. B.4(a)

B.1.2 Reverse flow for Port C

B.1.2A Three-dimensional streamlines

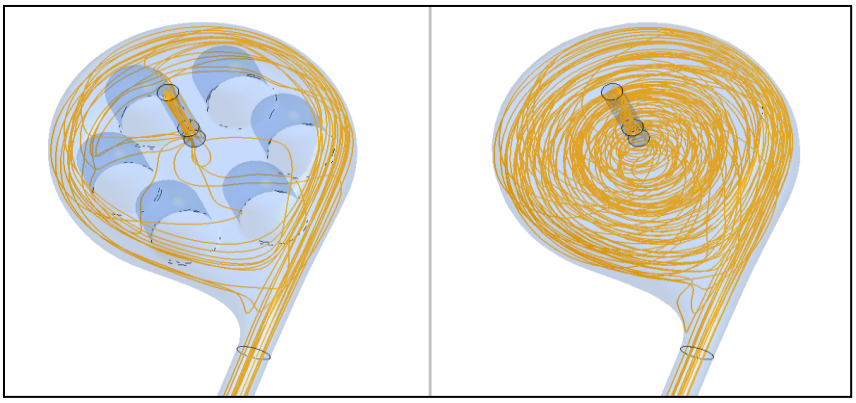

Fig. B.5: Three-dimensional streamlines for the Port C in reverse flow

B.1.2B Surface streamlines, vector diagrams and velocity contours

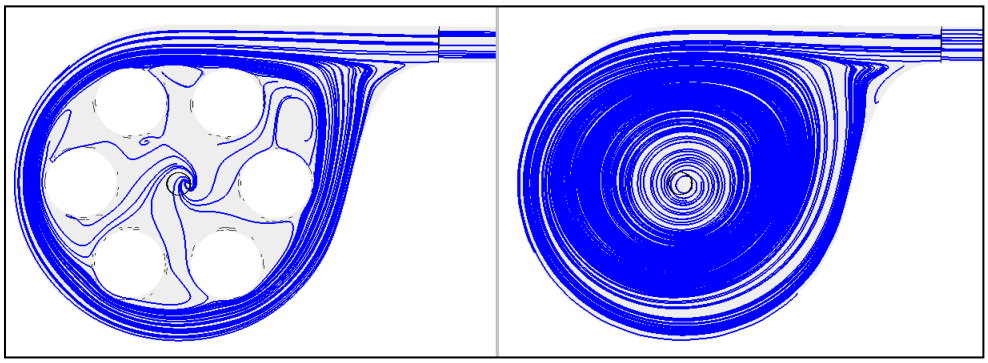

Fig. B.6(a): Surface streamlines on a central plane for the Port C in reverse flow

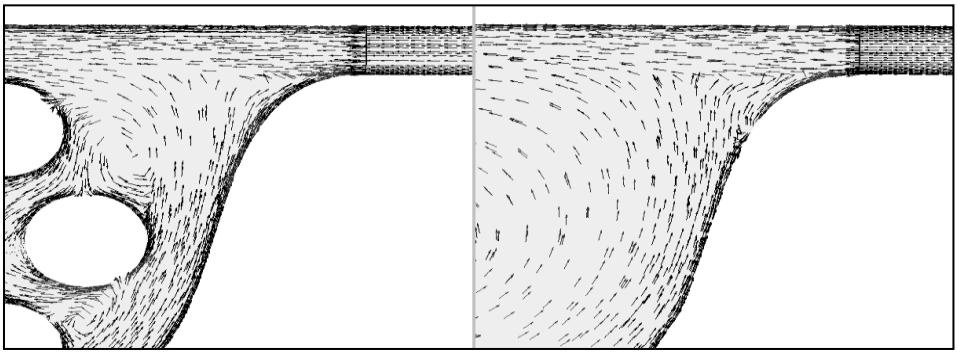

Fig. B.6(b): Velocity vectors in the plane corresponding to Fig. B.6(a)

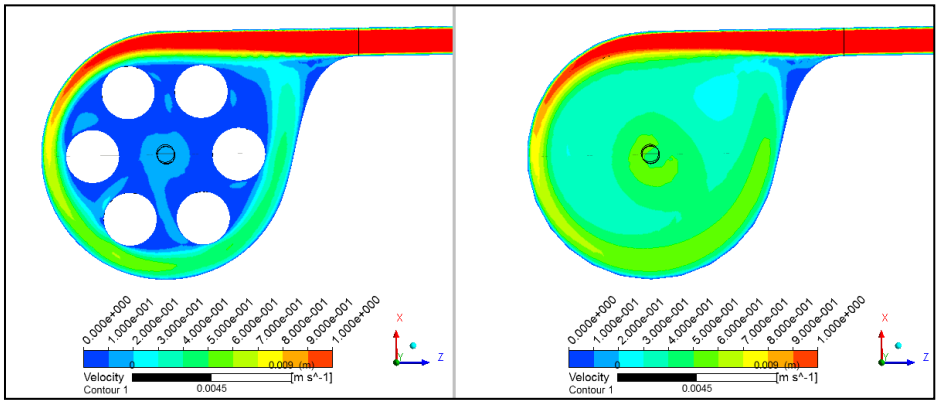

Fig. B.6(c): Velocity vectors in the plane corresponding to Fig. B.6(a)

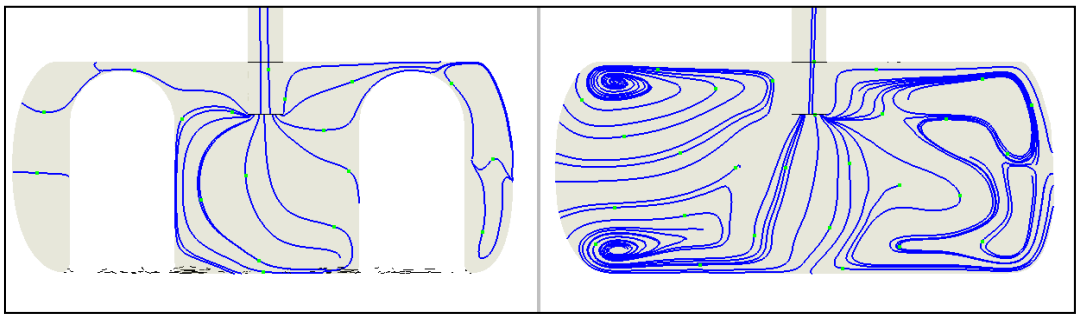

Fig. B.7(a): Surface streamlines on a plane perpendicular to Fig. B.6(a)

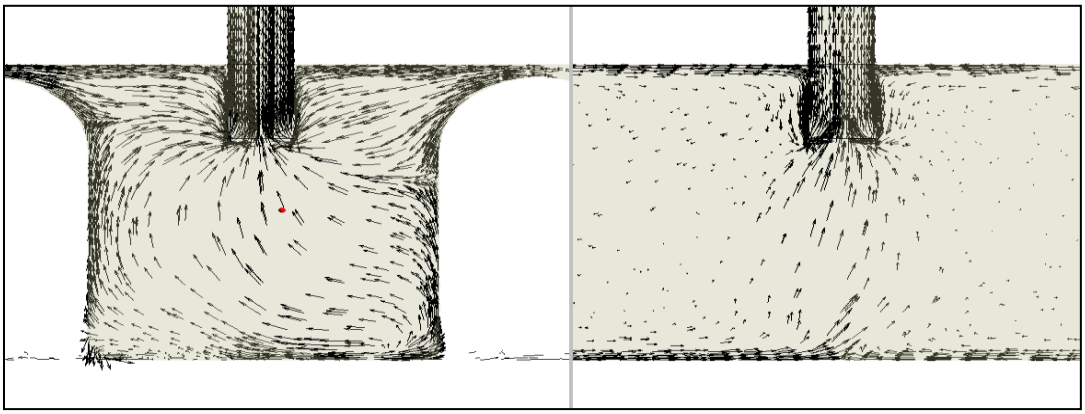

Fig. B.7(b): Velocity vectors corresponding to Fig. B.7(a)

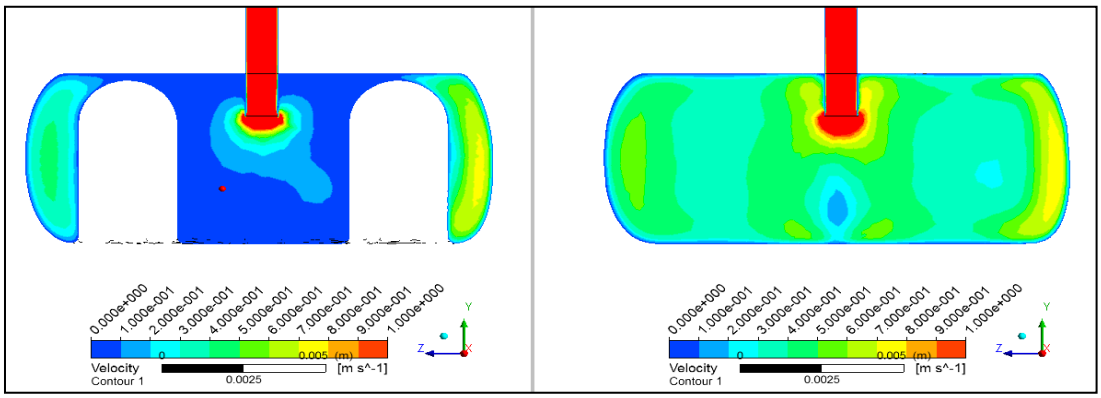

Fig. B.7(c): Velocity contours corresponding to Fig. B.7(a): (scaled between 0 and 1 m/s)

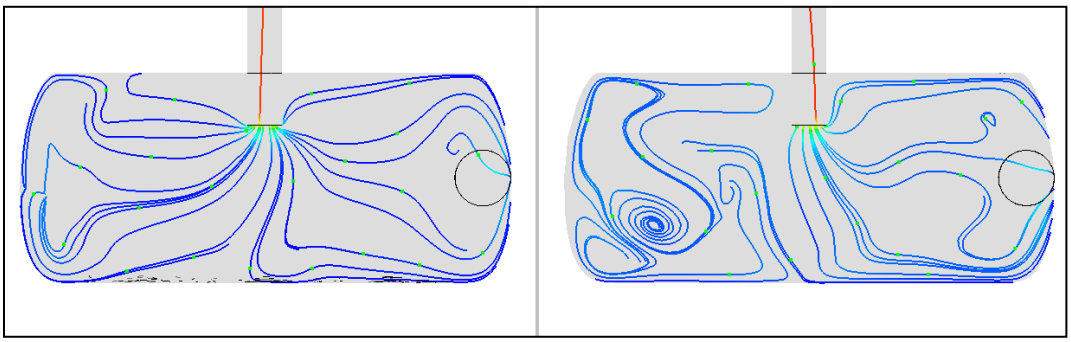

Fig. B.8(a): Surface streamlines on a plane perpendicular to Fig. B.7(a) and Fig. B.6(a) for the Port C in reverse flow

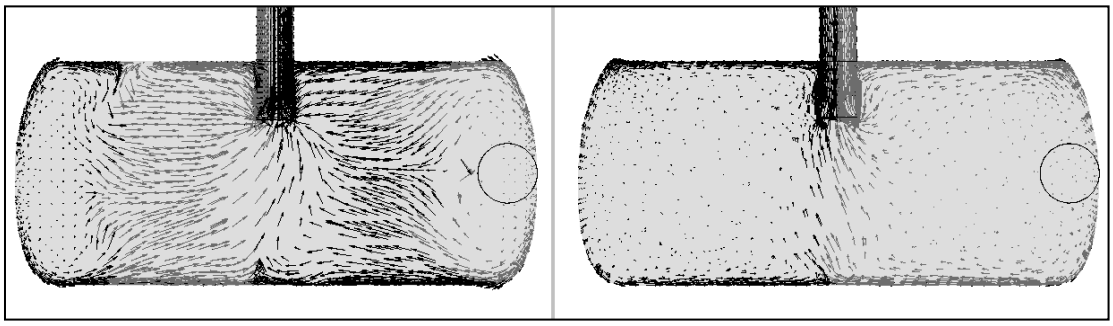

Fig. B.8(b): Velocity vectors corresponding to Fig. B.8(a)

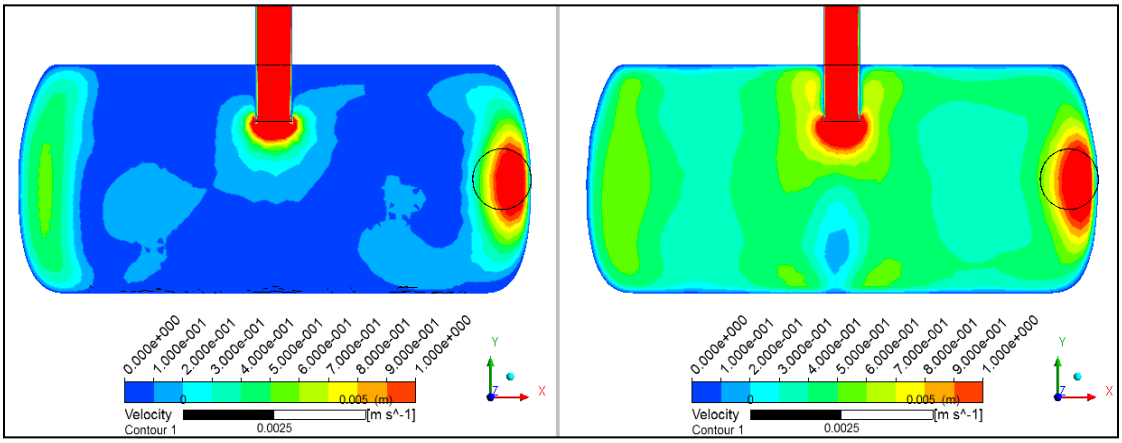

Fig. B.8(c): Velocity contours corresponding to Fig. B.8(a) (scaled: 0 - 1 m/s)

B.2 Results for Port A

B.2.1 Forward flow for Port A

B.2.1A Three-dimensional streamlines

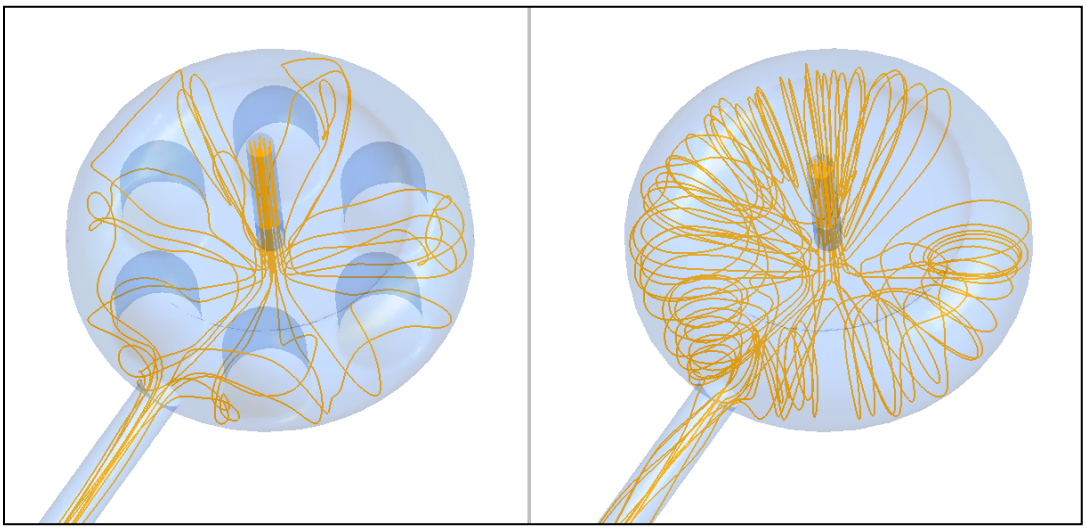

Fig. B.9: Three-dimensional streamlines for Port A, left: with volume-reducing members and right: without volume-reducing members

B.2.1B Surface streamlines, vector diagrams and velocity contours

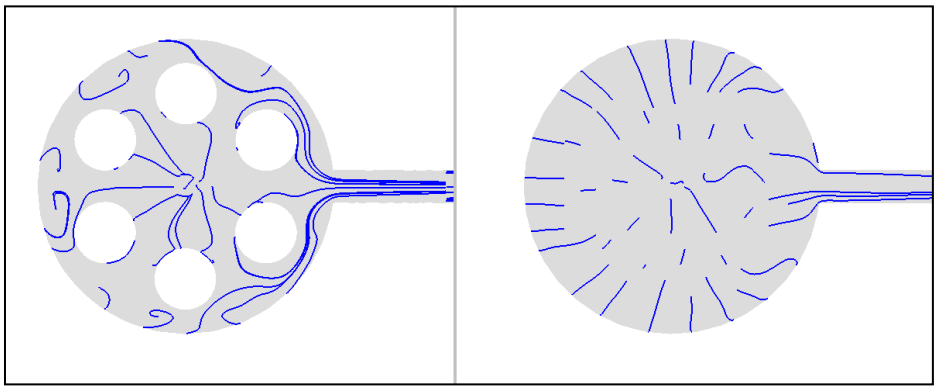

Fig. B.10(a): Surface streamlines on the central plane plane for Port A in forward flow

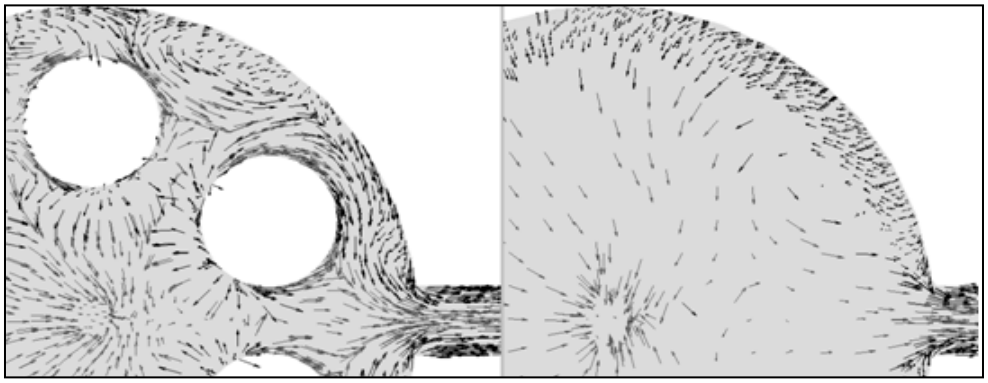

Fig. B.10(b): Velocity vectors corresponding to Fig. B.10(a)

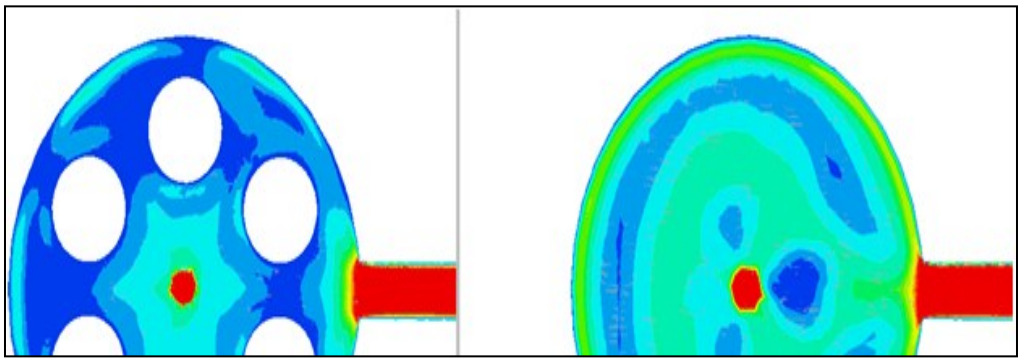

Fig. B.10(c): Velocity contours corresponding to Fig. B.10(a) (scaled: 0 - 1 m/s)

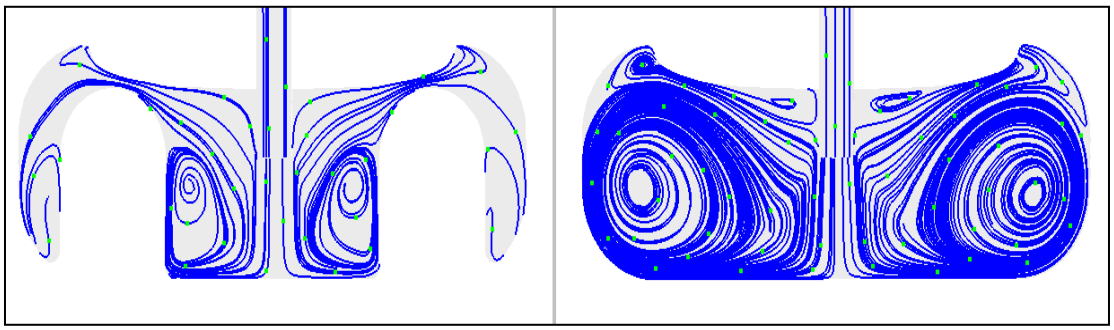

Fig. B.11(a): Surface streamlines in a plane perpendicular to Fig. B.10(a)

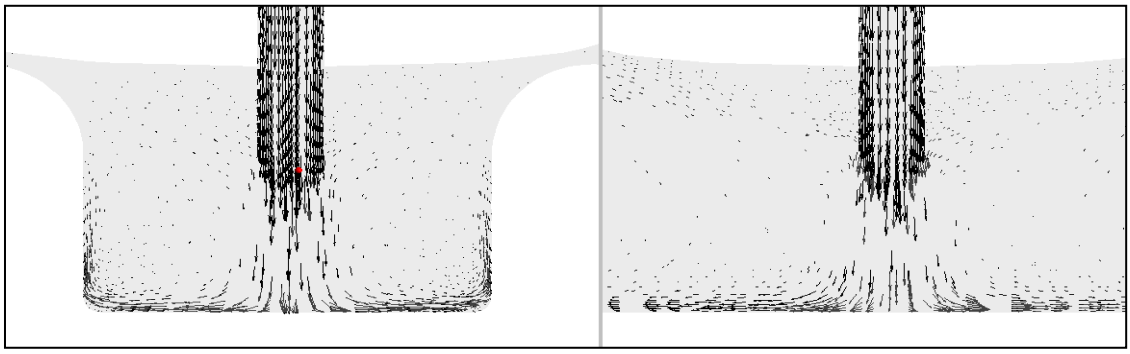

Fig. B.11(b): Velocity vectors corresponding to Fig. B.11(a)

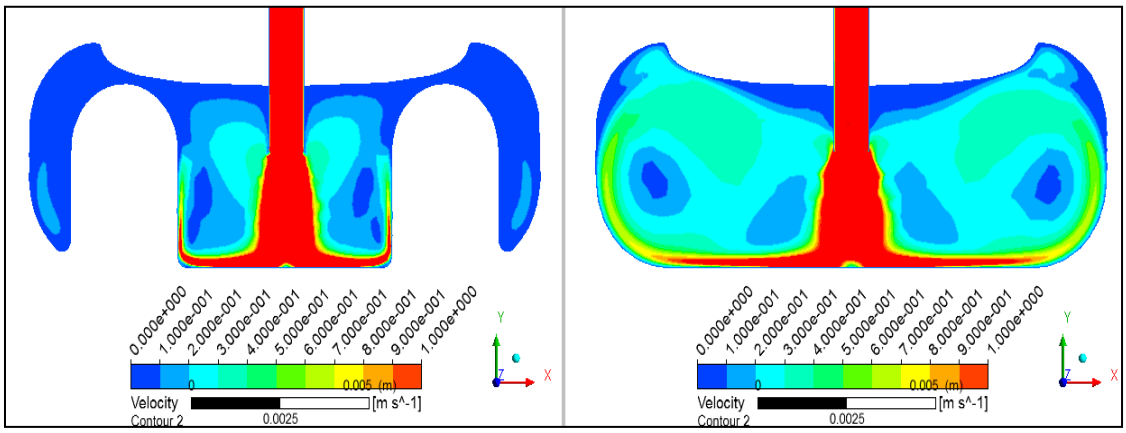

Fig. B.11(c): Velocity contours corresponding to Fig. B.11(a) (scaled between 0 and 1 m/s)

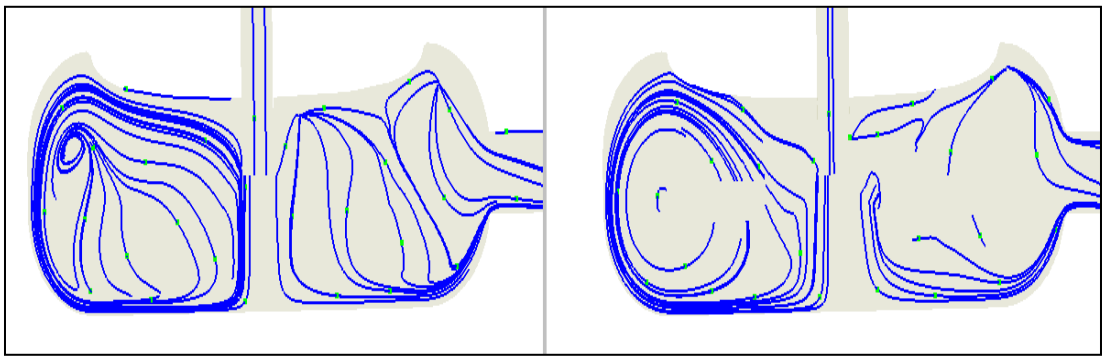

Fig. B.12(a): Surface streamlines in a plane perpendicular to *Fig. B.10(a) and Fig. B.11(a)*

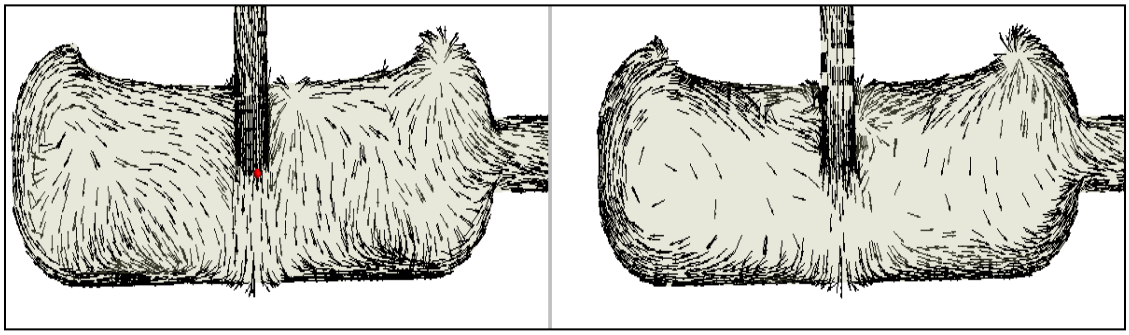

Fig. B.12(b): Velocity vectors corresponding to Fig. B.12(a)

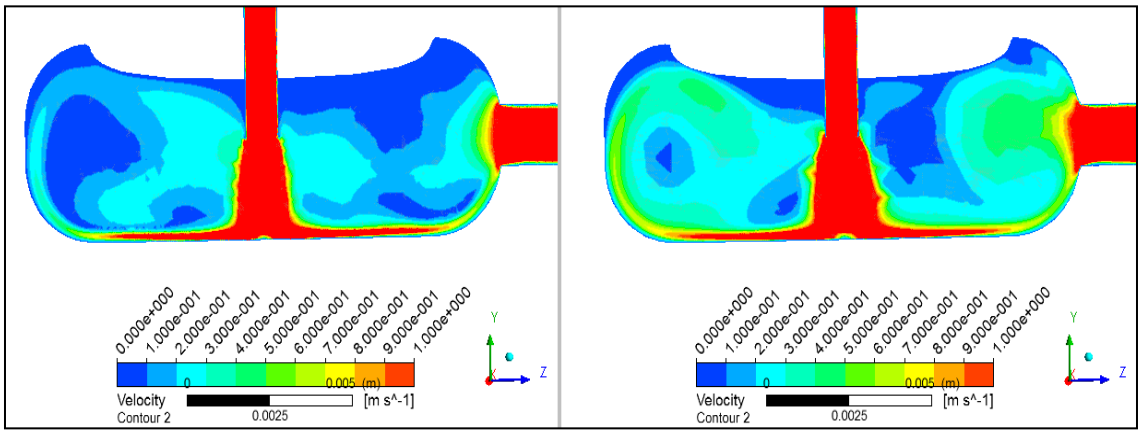

Fig. B.12(c): Velocity contours corresponding to Fig. B.12(a) (scaled: 0 - 1 m/s)

B.2.2 Reverse flow for Port A

B.2.2A Three-dimensional streamlines for Port A in reverse flow

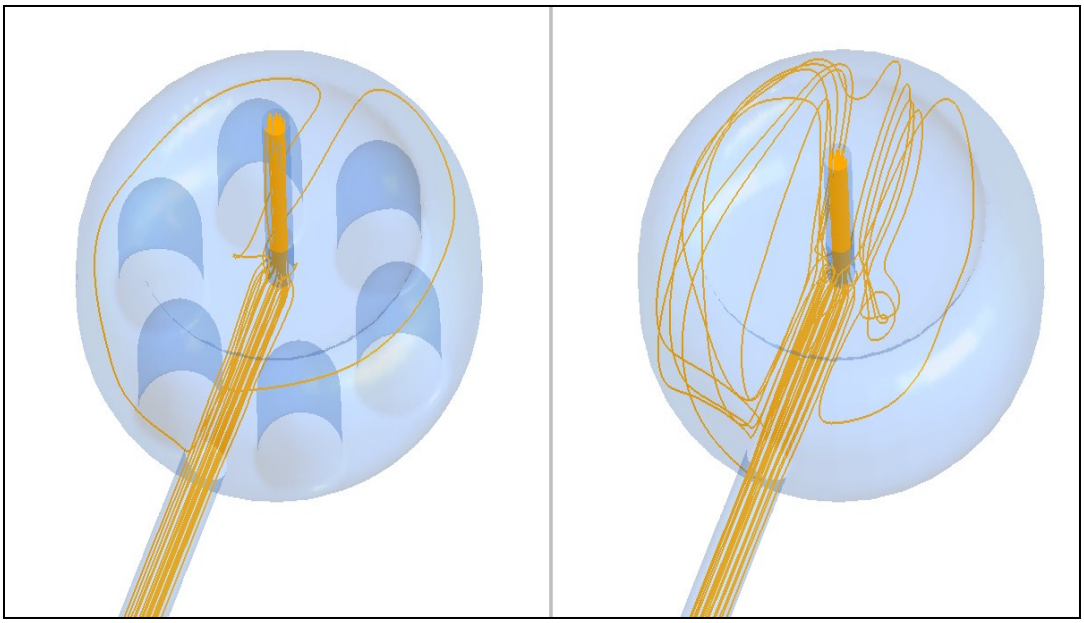

Fig. B.13: Three dimensional streamlines for Port A in reverse flow

B.2.2B Surface streamlines, vector diagrams and velocity contours

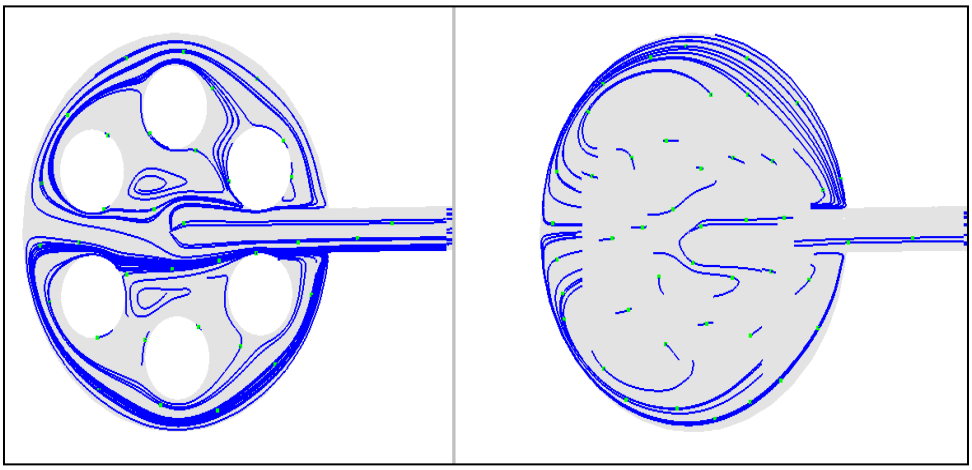

Fig. B.14(a): Surface streamlines on the central plane plane for Port A in reverse flow

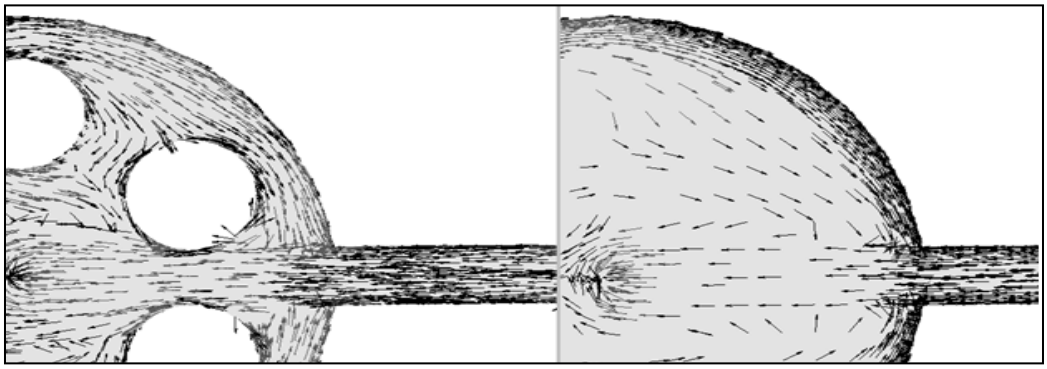

Fig. B.14(b): Velocity vectors corresponding to Fig. B.14(a)

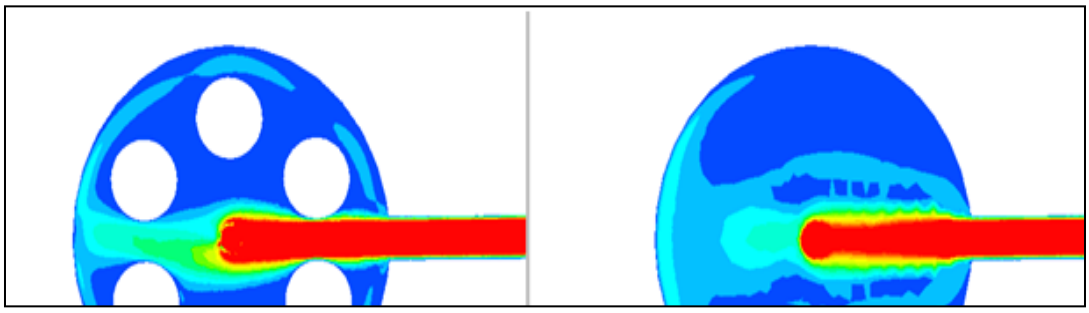

Fig. B.14(c): Velocity contours corresponding to Fig. B.14(a) (scaled: 0 - 1 m/s)

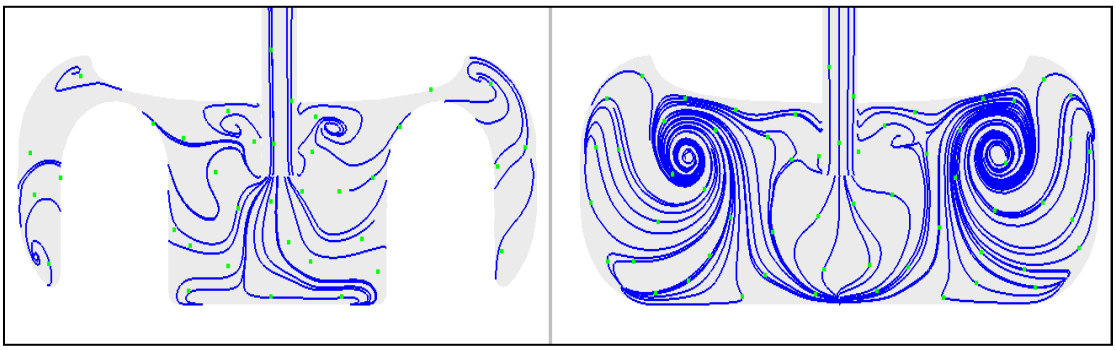

Fig. B.15(a): Surface streamlines in a plane perpendicular to Fig. B.14(a)

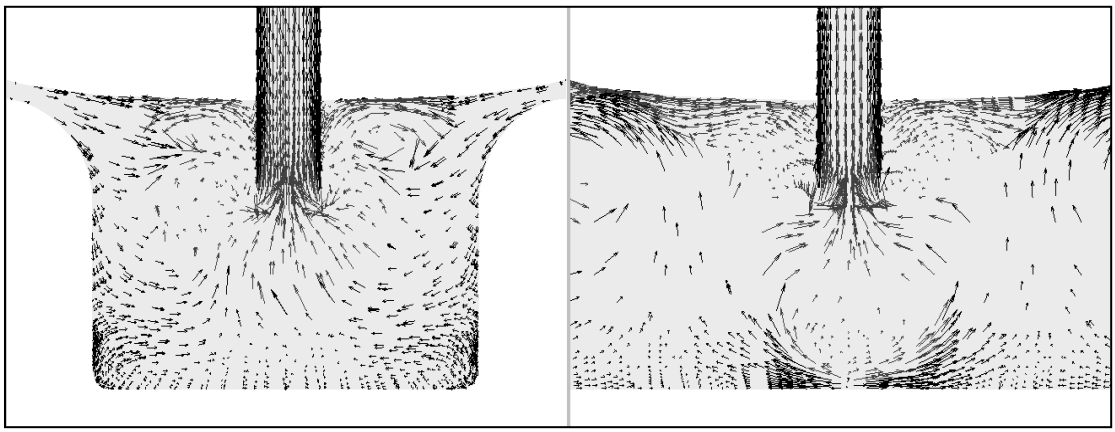

Fig. B.15(b): Velocity vectors corresponding to Fig. B.15(a)

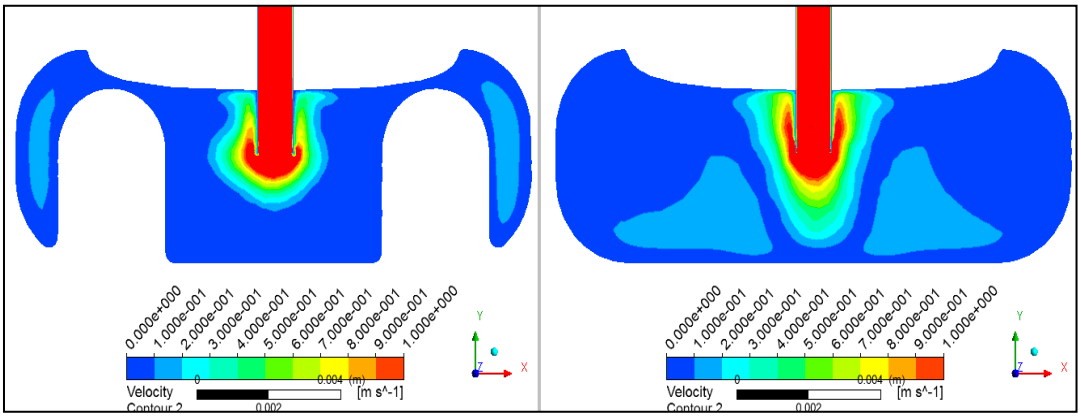

Fig. B.15(c): Velocity contours corresponding to Fig. B.15(a) (scaled: 0 - 1 m/s)

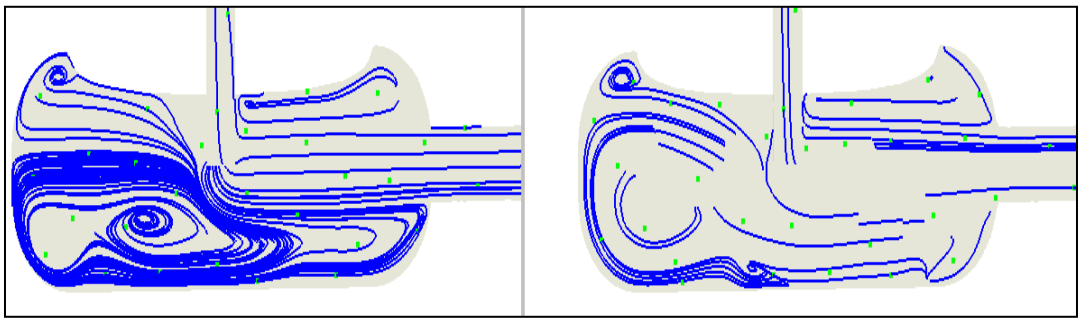

Fig. B.16(a): Surface streamlines in a plane perpendicular to Fig. B.14(a) and Fig. B.15(a)

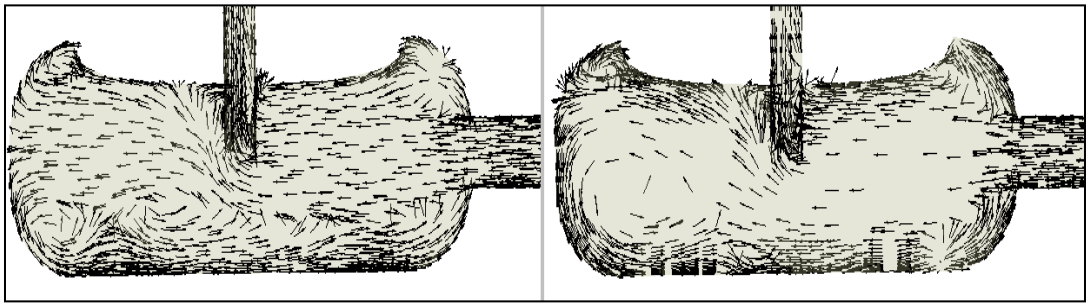

Fig. B.16(b): Velocity vectors corresponding to Fig. B.16(a)

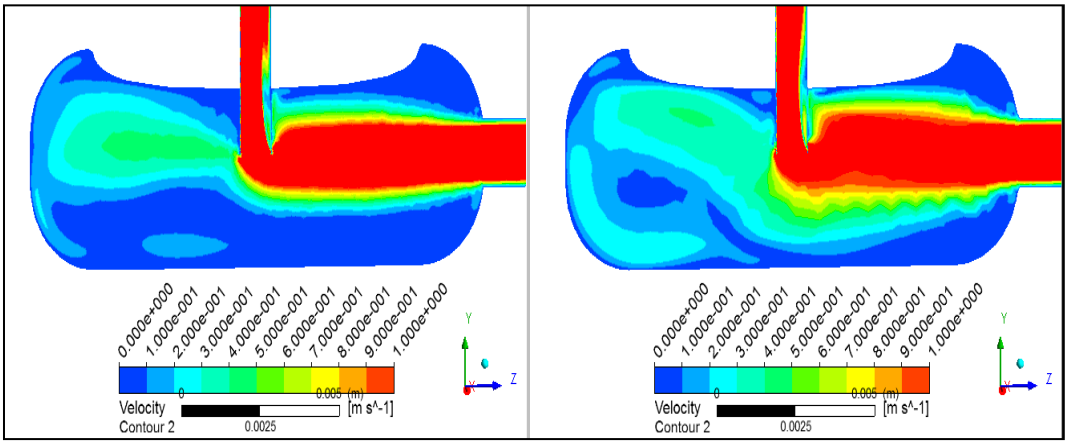

Fig. B.16(c): Velocity contours corresponding to Fig. B.16(a) (Scaled between 0 and 1 m/s)

Appendix C

EFFECT OF SIDE HOLES IN THE CATHETER TIP

C.1 Model setup

A simplistic initial model consists of the device alone and does not account for the flow through the annular region between the catheter and the vessel wall. In particular, it assumes that the device is surrounded by a static fluid at a constant pressure. It has been seen that pressure drop in the surrounding annular reason is very small (~10Pa). The fluid domains for the device without holes and with holes are shown in Figures C.1(a) and C.1(b) respectively.

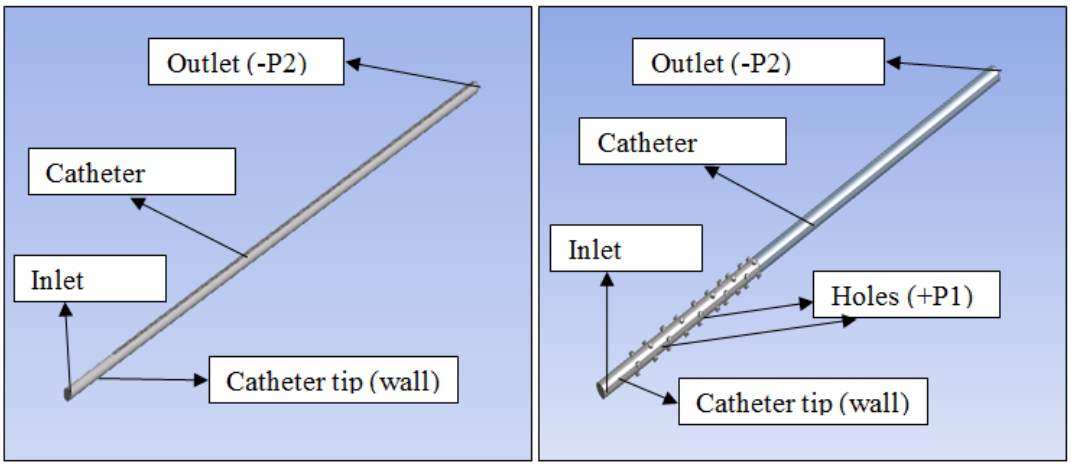

(a) *(b)*

Figs. C.1(a) and C.1(b): Figures showing the setup of the preliminary fluid flow model for the device without and with side holes respectively

The model is solved with the following assumptions and boundary conditions:

- Steady flow
- Incompressible flow
- Single fluid with a Newtonian viscosity
- Known pressure at the catheter exit
- Constant known inlet pressure
- Laminar flow
- No slip rigid device walls
- Straight catheter of a fixed length

The three dimensional Navier-Stokes equations along with the continuity equation were solved with the above assumptions and boundary conditions using ANSYS CFX. Planar symmetry was used wherever possible to reduce the number of nodes.

C.2 Results

One of the key results obtained from the simulation is the relationship between the pressure drop and flow rate for both the catheters. Figure C.2 shows the dependence of flow rate on pressure drop for both the proposed designs where, V_2 is the device without holes and V_5 is the device with side holes.

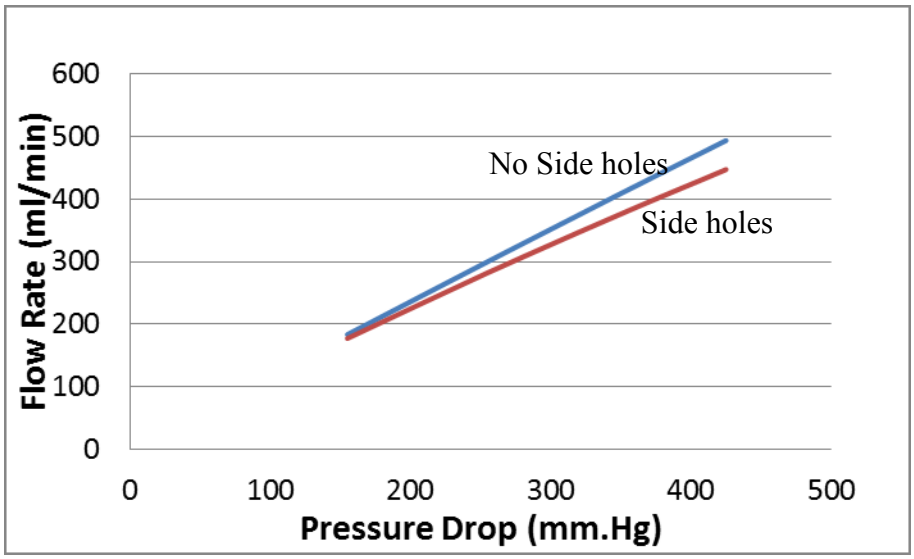

Fig. C.2: Dependence of flow rate on pressure drop across the catheter

As expected, the flow rate increases with pressure drop. The more or less linear relationship between the two variables indicates the attainment of fully developed flow for most part of the long catheter. The flow results were validated with the analytical results for fully developed laminar flow. It is, however, surprising to note that the device without the holes gives a higher flow rate than the one with the holes even though both of them are dimensionally similar. One would expect the addition of holes to increase the flow rate due to an increase in inlet area. Closer examination of the results reveals a series of recirculation zones adjacent to the holes (Figure C.3(a)) for the catheter with side holes while no such zones exist for the catheter without side holes (Figure C.3(b)). The presence of eddies creates an additional source of pressure loss. The effect of the increase in inlet area is offset by the presence of eddies. Hence, the addition of side holes leads to a reduced flow rate in the catheter for the same pressure drop.

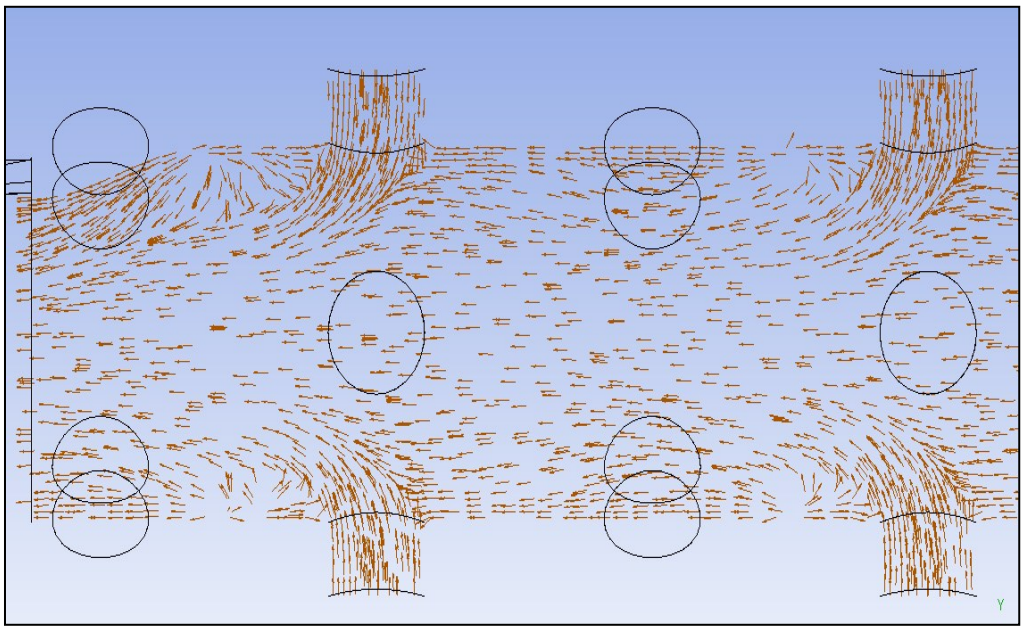

(a)

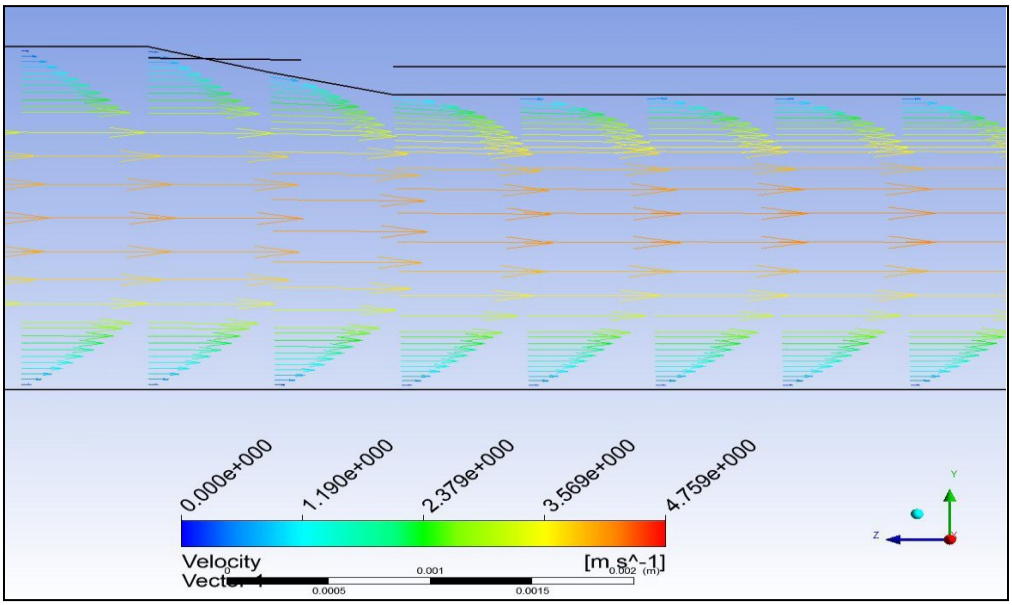

(b)

Figs. C.3(a) and C.3(b): Velocity vectors showing the presence and absence of re-circulating zones in the catheters with and without side holes respectively

Streamlines are also very effective tool for flow visualization. In this case, the streamlines also represent the path lines and streak lines. The streamlines originating from the inlet and the holes for both the devices are shown in Figures C.4(a) and C.4(b).

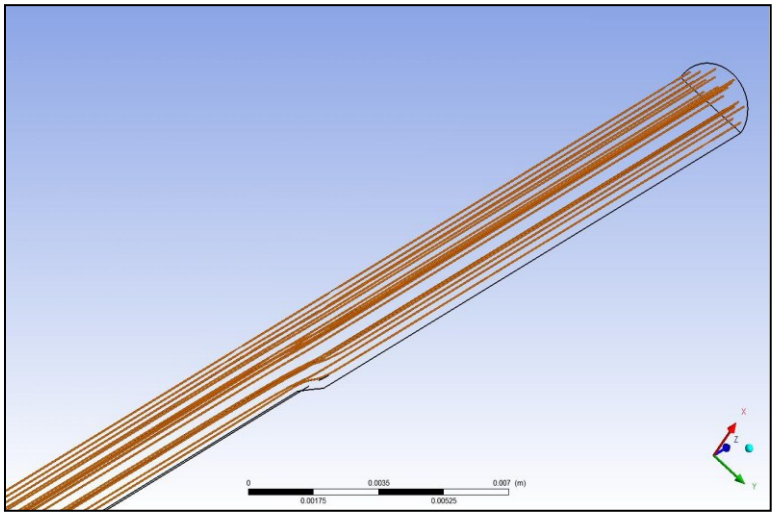

(a)

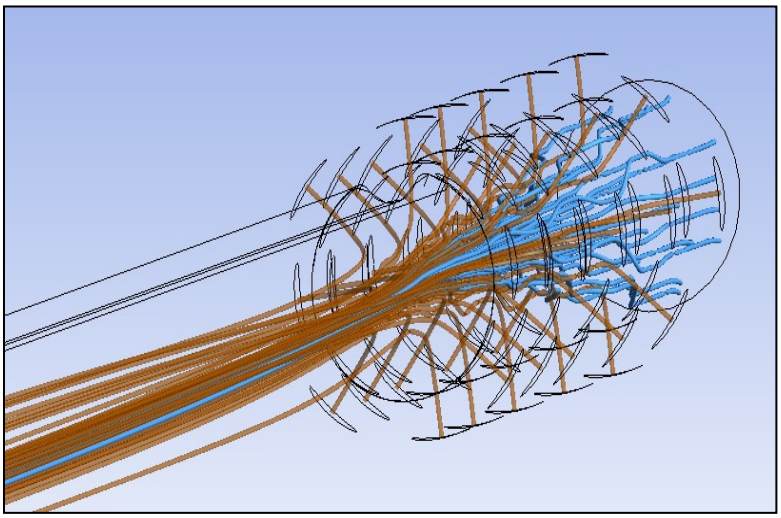

(b)

Figs. C.4(a) and C.4(b): 3-D Streamlines showing smooth and straight lines for device without holes and twisted and tortuous lines for the device with holes respectively

Another interesting observation for the device with side holes is that most of the flow comes from the side holes downstream of the inlet and barely any flow (0.7 %) comes through the inlet. This information can be seen using a 2D velocity contour plot as shown in Figure C.5.

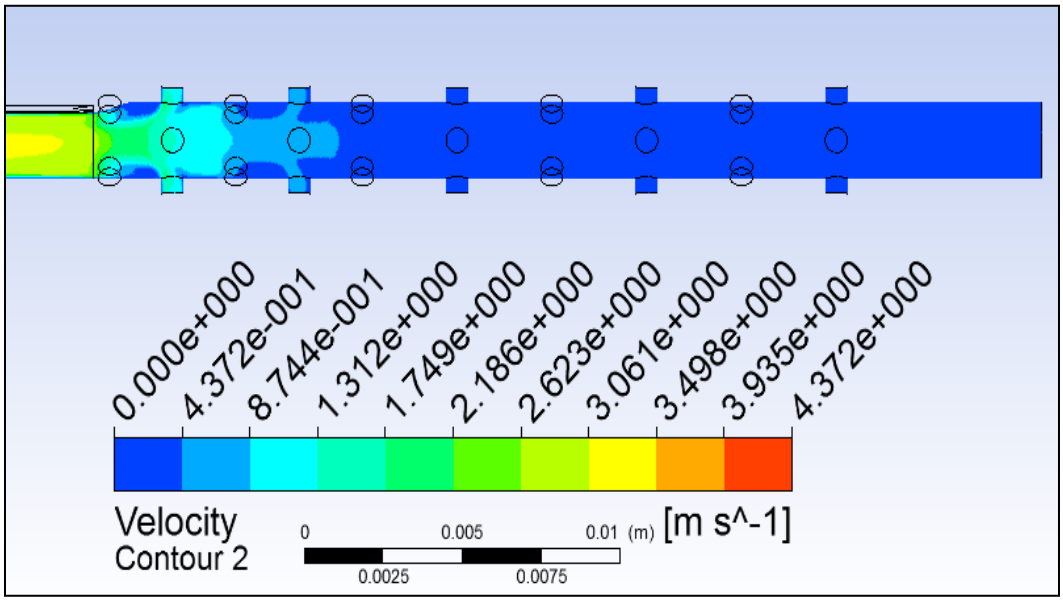

Fig. C.5: Velocity contour plot showing that most of the flow is coming through a few side holes and virtually no flow comes through the inlet for the device with side holes

Additional simulations with a different pattern of side holes yielded different flow patterns. The flow pattern depends on the size, spacing and shape of the holes.